Delivery of CO by Bio-Inspired Metallocentres

A thesis submitted to the University of East Anglia
For the degree of Doctor of Philosophy
Submitted December 2016

Mark A. Wright

Energy Materials Laboratory
School of Chemistry, UEA
Norwich

Abstract

Although once thought to have no beneficial medicinal value due to its historic reputation as being a 'silent killer', recent investigations into the therapeutic applications of carbon monoxide (CO) on mammalian physiology have sparked a growing interest in designing metal-based carbonyl complexes to act as pro-drugs. Thoughtful design of transition metal carbonyl complexes result in controllable and tunable CO release triggered by photochemical labilization from the metal centre. The work contained in this thesis focuses on the design, synthesis and CO release capabilities of a series of photoactive iron-based carbon monoxide releasing molecules (photoCORMs). This work is complimented with studies of analogous ruthenium complexes.

PhotoCORMs are able to impart spatial and temporal control over CO delivery following site specific irradiation with an appropriate wavelength. High energy ultra-violet light has poor tissue penetration and causes damage to the skin. Here, a series of iron carbonyl complexes were synthesised. Extension of the ligand conjugation system and addition of a nitrogen donor group proved to shift the absorption spectrum in a bathochromic fashion. Examination of photoCORM capabilities reveal the iron carbonyl complexes release CO following visible light irradiation.

The number of developed CORMs which satisfy the required pharmaceutical characteristics is relatively small. Essential characteristics include water solubility and biocompatibility. We expand on the design of our complexes by incorporating thiolated saccharide ligands into the coordination sphere. The resulting dimeric carbonyl complexes display significantly enhanced water solubility as well as a major change in CO release behaviour.

The anti-inflammatory properties of the photoCORM systems were investigated *in vitro*. Production of LPS-induced pro-inflammatory cytokine, TNF-α was markedly decreased following CORM administration. Surprisingly, CORM potency was greatest when cells were kept in the dark.

Designing two photon up-converter systems is a leading strategy to enhanced the light harvesting ability of metal complexes. Here, the design of such attachable systems is discussed.

Acknowledgements

First and foremost, I would like to offer my sincerest gratitude to my supervisor, Dr Joseph Wright, for his friendly support, thoughtful guidance and warm encouragement throughout this Ph.D. Through his supervision, and the wealth of knowledge he has offered, he cemented a pathway for me to grow as a synthetic chemist, whilst also teaching me on the intricacies of LaTeX and the art of scientific writing. I would like to thank Prof Christopher Pickett for the insightful discussions and the valuable advice he offered during this period of study. I would also like to express my appreciation to Dr Maria O'Connell and Tyler Wooldridge, who welcomed me into their laboratory and provided me with the equipment and know-how to perform the biological assays which proved to be fundamental to the success of this project. Further thanks goes to Sarah Morris, who performed the cell viability assays reported in this thesis.

I am especially grateful to the friends and colleagues, past and present, who have made working in the Energy Materials Laboratory a thoroughly enjoyable experience. Special thanks to Aušra, Amanda and Woody for their unique ability to fill the lab with laughter, and to Farhana and Trevor for their constant support and friendship. This thanks also extends to project student, Matt Surman (*a.k.a* 'swaglord') for his dedication to the project and his uplifting humour.

I am indebted to my family for their unconditional help and faithful encouragement of my studies. I especially appreciate the times spent playing Risk, with our good-humoured rivalry and jokey banter; I will not easily forget those happy evenings. A heartfelt thanks also goes to Linda and Tony Harnwell, who have opened their home to me and showed me great kindness throughout the years.

Lastly, my gratitude beyond measure, to the person who has stood as a pillar of support and comfort since our first meeting back at sixth form. You have been by my side throughout this Ph.D., living every single moment of it with me. If it weren't for your selfless encouragement, I would not have had the courage to embark on this journey in the first place. Emily, for your unparalleled love and unwavering support, I have not words enough here. Thank you.

In the end, it's not the years in your life that count.

It's the life in your years.

– Abraham Lincoln

Contents

Chapter 1

Introduction

1.1 Carbon Monoxide: An Overview

The use of carbon monoxide (CO) as a therapeutic agent may come as a surprise if one considers its historic reputation as being a 'silent killer'. Indeed, the toxicity of this colourless, odourless and tasteless gas has been well known since Greek and Roman times.[1]

Despite its notoriety, the beneficial role of CO began to emerge during the 20th century when Swedish physician Torgny Sjöstrand demonstrated that human beings constantly exhale CO, even when all external sources of the gas were removed.[2] The endogenously produced CO was found to be a by-product of the oxidative decarboxylation of haem, which is catalysed by a family of enzymes called haem oxygenases.[3] Sjöstrand noted that diseased patients produced significantly greater quantities of CO compared to healthy patients.[2] This surprising and unexpected observation led to a surge of studies on the biological relevance of gaseous molecules.

Carbon monoxide, along side other biologically relevant gases, namely nitric oxide (NO) and hydrogen sulfide (H_2S), has been shown to play a pivotal role as a signalling molecule in mammals.[4] CO has been established as being anti-inflammatory,[5,6] vasodilatory,[7,8] anti-apoptotic[9] and plays a crucial role in a number of immune-related disorders.[10]

The use of carbon monoxide as a therapeutic agent has sparked a number of questions.

There are major concerns over administrative methods of gaseous CO. These include the possibility of CO poisoning and what constitutes an effective dose, as well as fundamental questions regarding its target sites and mechanism(s) of activity.

Pharmacological chemists are interested in the development of so-called carbon monoxide releasing molecules (CORMs). These molecules act as inert molecular vehicles capable of carrying bound CO through the blood stream and only releasing their load when subjected to do so by a specific trigger at defined tissues. The advantage of using CORMs include the possibility of carefully designing drugs so that properties such as tissue specificity and CO release capability can be meticulously controlled.

1.2 Bioactivity of CO

1.2.1 Action of Haem Oxygenase

The majority of CO generated in mammalian organisms derives from the catabolism of haemoglobin from red blood cells by the haem oxygenase (HO) enzymes. HO was originally characterised by Tenhunen *et al.* in 1969,[11] who uncovered the enzymatic mechanism responsible for the oxidative degradation of haem to yield bilirubin, CO and ferrous iron (Scheme 1). The conversion requires the presence of molecular oxygen, nicotinamide adenine dinucleotide phosphate (NADPH), and the concerted action of cytochrome P_{450} reductase.[12]

HO catalyses the oxidative degradation of haem by oxidising the α-methene bridge of the protoporphyrin ring to form the green bile pigment and antioxidant, biliverdin. Subsequently, involvement of NADPH and biliverdin reductase reduces the biliverdin to form the yellow bile pigment and antioxidant, bilirubin.[11] In this pathway HO is rate-limiting.

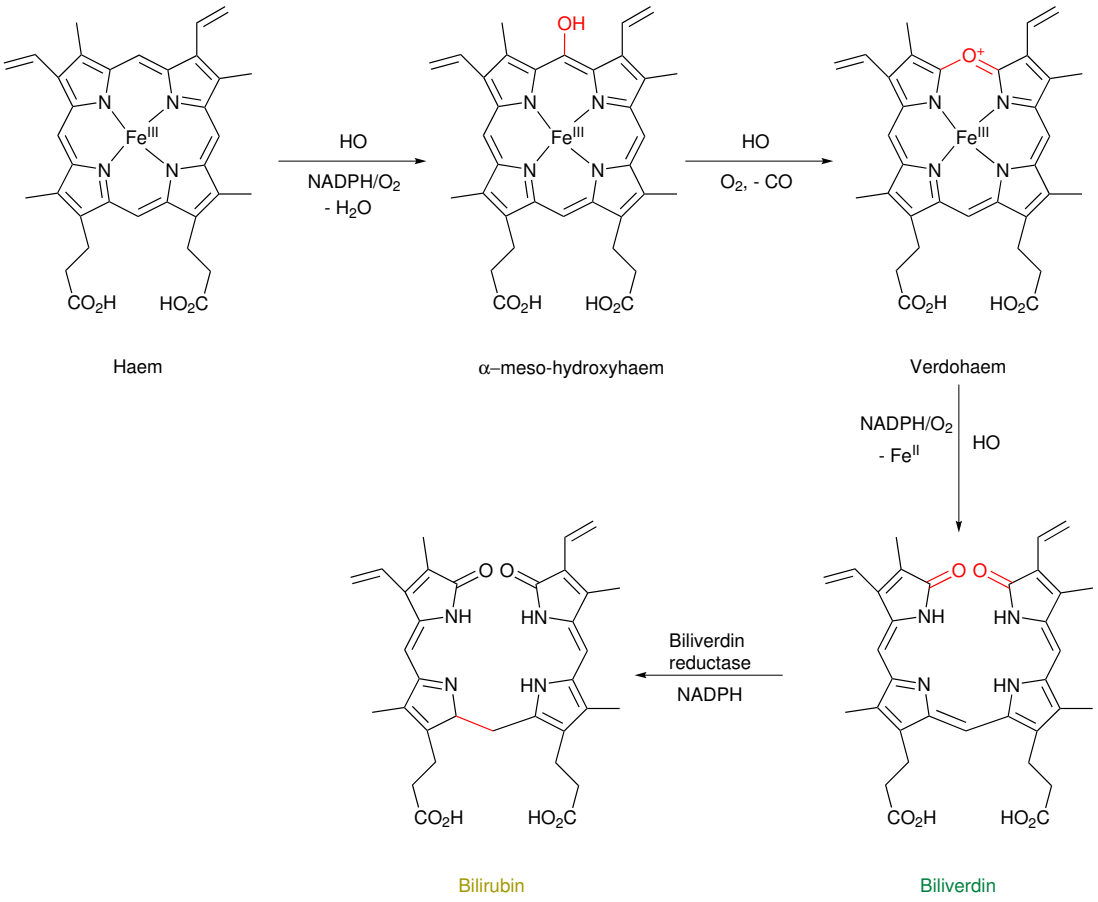

Scheme 1: Catabolism of haem by haem oxygenase

The roles of HO act to protect the organism. Free haem molecules are toxic to the cellular environment, leading to lipid peroxidation and generation of reactive oxygen species (ROS).[13] The biliverdin and bilirubin produced are antioxidants and are capable of performing an array of important cellular functions.[14] The free ferrous iron generated is reutilized, being taken up by ferritin and either excreted by the cell or recycled for haem synthesis. The generated CO has been associated with a variety of beneficial effects which include reducing cellular stress by inhibiting the production of pro-inflammatory cytokines, thus suppressing the expression of pro-inflammatory enzymes.[15]

There are three isoforms of the HO enzyme: HO-1, -2 and -3, although only HO-1 and HO-2 appear to be active enzymes.[1] The HO-2 and -3 isoforms are constantly expressed and act to regulate the basal level of free haem. HO-2 is a non-inducible isoform which serves to maintain regulatory functions in the nervous system and is commonly found in the brain, testis, liver and endothelium. HO-3 is structurally similar to HO-2 but with

a lower enzymatic activity.[16] HO-1 is an inducible isoform that can be up-regulated by a vast array of stimuli[17] including substrate (haem), oxidants, heavy metals, cytokines and radiation.[12] This suggests that HO-1 is not only in the business of haem degradation and iron homoeostasis, but represents a fundamental defence against stressful insults to the organism.[18,19] HO-1 has been explicitly shown to impart cellular protection against a variety of injuries.[5,15,20] Examples include protection against vascular diseases such as atherosclerosis and hypertension[12] as well as the suppression of endothelial cell apoptosis.[21]

HO-1 is critical for survival, with HO-1 deficiencies in mice and humans linked with short lifespans. In contrast, HO-2 deficient mice can survive through their expected lifespan. Mice treated with high doses of HO inhibitors or with a HO-1 deficiency showed greater susceptibility to lipopolysaccharide (LPS) induced endotoxic shock.[22] Genetic deficiency or inhibition of HO-1 activity has also been associated with oxidative tissue damage[18] and chronic inflammation in human and mice models. Up-regulation or over-expression of HO-1 has been shown to improve vascular dysfunction and inhibit chronic rejection.[23] Interestingly, administration of gaseous CO to HO-1 deficient mice acted to reduce the LPS-induced inflammation. Indeed, targeting HO-1 is an attractive pathway for the therapeutic relief of a number of ailments such as inflammation and reperfusion injury.

Although the functional importance of the HO system in providing an essential defence for the organism has been well established, the precise mechanism(s) by which HO-1 elicits this protective response remains unclear. The ability of CO to provide cytoprotection mimics that of HO-1 in rodent models. Extensive research into the *in vivo* application of CO has established a number of important beneficial functions in response to various physiological and pathophysiological conditions.

1.2.2 Gaseous Mediations

The vital protective action of the HO system and its by-products led to the postulation that CO acted as a biological gaseotransmitter. Indeed, it was discovered that CO displayed similar protective properties observed for nitric oxide (NO). Studies on the vessel relaxation properties of NO and CO commenced at the same time.

From such studies the biomedical potential of NO rapidly emerged as a versatile molecule capable of important physiological and pathophysiological effects. Ironically CO was dismissed, its relaxation functions were viewed as being merely circumstantial and were disregarded.[17] To justify this action one must consider that at the time much more information about NO had been collected as it was already recognised as being a signalling molecule. NO is a reactive molecule capable of initiating a range of versatile chemistry on biological targets. This is in contrast to CO, where only reactivity towards haem moieties was known. Although the endogenous generation of CO was known well before NO was recognised as a biological mediation, it was initially believed that the physiological effects of NO and CO operated independently of each other. This was later found not to be the case when NO donor molecules were shown to activate HO-1 and increase CO production.[17]

Nitric oxide is generated endogenously in mammalian organisms through the oxidative conversion of L-arginine to L-citrulline. This reaction is catalysed by NO synthase (NOS), of which there are three active isozymes: neuronal, endotherlial and inducible NOS. The NO molecule is redox active, forming $[NO]^+$ or $[NO]^-$ following a one electron oxidation or reduction, respectively. The redox state of the diatomic molecule is responsible for the physiological benefit it generates. NO acts as a superoxide scavenger, leading to the formation of peroxynitrile ($[O{=}NOO]^-$). This is rapidly excreted from the body by decomposing to NO_2 and $[NO_3]^-$ and exhaled.[24]

1.3 CO Target Sites

1.3.1 Soluble Guanylyl Cyclase

Soluble guanylyl cyclase (sGC) is a heterodimeric (α/β) haem protein found in a variety of mammalian cells which sense cellular signalling molecules including NO and CO. The catalytic reaction involves the conversion of GTP to cGMP, a cyclic nucleotide which plays a role in a number of physiological processes including vasodilatation.[25] Guanylyl cyclase contains two catalytic domains, an α and β domain. The β domain

contains a 5-coordinate haem moiety. NO coordinates to the iron metal centre and in doing so fully displaces a bound histidine. This results in a large conformational change which activates the enzyme. On the other hand, CO coordinates with a lower binding constant compared to NO. As a result, the histidine remains bound and iron becomes 6-coordinate.[26] It is thought that an intracellular molecule interacts with the α domain which leads to the dissociation of the bound histidine to activate the enzyme.[24] Consequently, the extent at which CO activates sGC is much lower compared to the activity achieved by NO. However in the presence of YC-1 (**1**, Figure 1), a small synthetic molecule which activates sGC, an increase in the production of cGMP is reported.

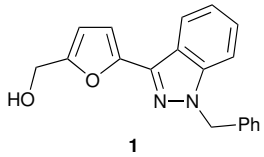

1

Figure 1: sGC activator, YC-1

Recent studies have shown CO promotes the relaxation of vascular smooth muscles, a response which has been attributed to the action of activated sGC.[8] Motterlini and co-workers investigated the effect CO has on aortic rings precontracted with phenylphrine, and found CO activity is at least partially cGMP dependent. A study by Fan *et al.* demonstrated that CO also had the ability to increase cellular ATP (adenosine triphosphate) in an sGC associated mechanism. The levels of ATP generated *in vitro* was reduced in the presence of ODQ (1*H*-[1,2,4]oxadiazole[4,3-*a*]quinoxalin-1-one), which acts as a sGC inhibitor.[27]

1.3.2 Mitogen-Activated Protein Kinases

Mitogen-activated protein kinases (MAPKs) are a family of proteins which regulate a number of cellular functions, including regulating the expression for pro-inflammatory cytokines[28] such as TNF-α (tumor necrosis factor) and IL-1 (interleukin-1). They are activated by a variety of extracellular stimuli including UV light, heat, osmotic shock,

inflammatory cytokines and growth factors.[29] MAPKs consist of a serine-threonine domain and achieve cellular signalling following phosphorylation. There are three types of MAPK, namely, extracellular signaling-regulated kinase (ERK1/2), c-Jun (N)-terminal kinase (JNK1/2/3) and p38 isoforms.

Activation of MAPK by endotoxin lipopolysaccharide (LPS) leads to a rapid increase in the production of pro-inflammatory mediators and the down-regulation of anti-inflammatory cytokines. Upon CO targeting of MAPKs, inhibition of the expression of the pro-inflammatory cytokines and up-regulation of the production of the anti-inflammatory cytokine IL-10 occurs. *In vivo* studies using mice models administrated with LPS in the presence of CO displayed significantly reduced quantities of the pro-inflammatory cytokine TNF-α. Choi and co-workers further demonstrated that CO mediated this anti-inflammatory action *via* activation of p38, ERK1/2 and JNK pathways in a concentration-dependent manner.[5] Pathway p38 activation was achievable at lower concentrations of CO (250 ppm) whilst ERK1/2 and JNK remain unaffected at this dosage. Furthermore, dominant negative mutant mice models ($Mkk^{-/-}$) showed considerable increase in TNF-α production following LPS administration compared to the $Mkk^{+/+}$ mice. In the presence of CO, there was a significant up-regulation of the production of the anti-inflammatory cytokine IL-10 in the $Mkk^{+/+}$ specimens. $Mkk^{-/-}$ mice in a CO-enriched atmosphere produced slightly greater amounts of IL-10 compared to specimens in a CO-absent atmosphere, which indicates CO achieves its anti-inflammatory effects by targeting the MAPK pathway.[5,28,30]

It is unclear exactly how CO modulates MAPK-related pathways as the kinases do not contain a haem residue. One potential candidate is the Mn(II) containing protein phosphatase C2 (PP2C), which acts as a serine/threonine phosphatase involved in responding to cellular stress.[31] This offers a potential direct pathway in which CO could modulate MAPK, where coordination onto the transition metal active site brings about a fundamental change in the phosphorylation-dephosphorylation process. Conversely, CO could modulate MAPK *via* an indirect pathway. In a study on lung ischemia-reperfusion in rat models, Mishra *et al.* showed that CO suppressed ERK activation, which in turn reduced early growth response 1 (Egr-1, a transcriptional activator of inflammatory cascades) expression.[32] Their findings highlight a cGMP dependent pathway, as the

suppression of ERK was reversed in the presence of a sGC inhibitor.

1.3.3 BK_{Ca} channels

So-called 'big conductance' K_{Ca} channels are present in many types of vascular smooth muscle cells and are considered to have two main physiological functions: determining membrane potential and regulating electrical activity within the cell. The structure of BK_{Ca} channels consists of two subunits comprised of tetramers: a pore-forming α-subunit and an accessory β-subunit. The channels allow the influx of Ca(II) ions through the membrane and an eflux of K^+ ions, resulting in cell membrane hyperpolarization and reducing cellular excitability. There are three types of BK_{Ca} channels: small, intermittent and large conductance. The physiological role of BK_{Ca} channels include neuronal excitability and smooth muscle contractility, which in turn affects vascular activity.[33]

Mitochondrial produced reactive oxygen species (ROS) have been shown to activate BK_{Ca} by increasing Ca(II) spark frequency along with increasing the effective coupling of Ca(II) to K^+ channels.[34] As CO has been shown to promote ROS production in mitochondria, this suggests an indirect mechanism by which CO could effect vascular activity.[35] In addition, evidence has emerged which suggests BK_{Ca} channels enhance cGMP-induced relaxation of smooth muscles.[36] The two systems are thought to be linked, as particular substances which increase cGMP concentration also cause membrane hyperpolarization in smooth muscle cells. It is hypothesised that this leads to vasorelaxation.[37]

Direct interaction of CO with K^+ channels was originally met with scepticism as the channels lack a transition metal (TM) centre for CO to react. Further investigation showed that the haem containing complex, iron protoporphyrin IX, is involved in the covalent bonding of calcium in Ca(II)-sensitive K^+ channels. Wu *et al.* demonstrated the vasodilatory action of artery smooth muscle cells in rats tails was achieved by CO in an concentration-dependent manner.[38,39] The suggested mechanism involved an interaction between CO and a histidine residue located on the α-subunit of BK_{Ca} channels.

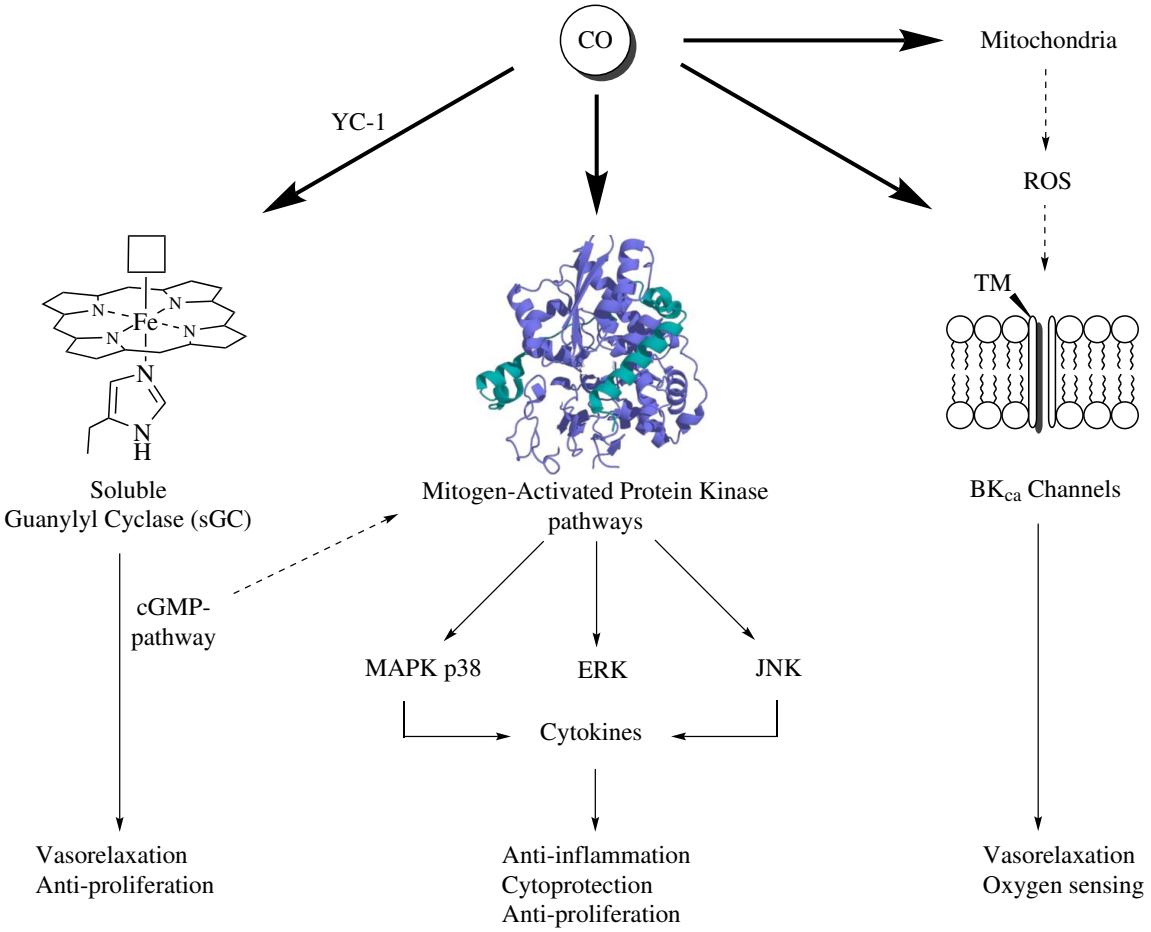

Figure 2: Suspected pathways involved in CO signalling (ROS = reactive oxygen species, TM = transition metal)[5,8,24,26,31,38–40]

1.4 CO as a Therapeutic Agent

In prokaryotic cells such as anaerobic bacteria, exogenous CO is extracted and used as a source of carbon and energy. In eukaryote organisms, CO acts as a versatile signalling molecule and has been shown to play pivotal roles in a wide range of physiological and pathophysiological processes.[8] The beneficial effects attributed to CO includes, but are not limited to anti-inflammatory processes,[5,6] vasodilatation,[7,8] risk reduction in organ transplant,[20] platelet aggregation inhibition,[41] oxygen sensing,[40] bacterial growth inhibition,[42] cell proliferation,[4] anti-apoptotic effects and cytoprotective effects.[9]

Employing CO as a therapeutic agent is based on studies on induction and gene transfer of HO-1, inhalation of gaseous CO and administration of CORMs. The inducible isoform of heam oxygenase (HO-1) is activated by a number of oxidative stress triggers and represents an opportunity for therapeutic targeting. Up-regulation and over-expression of HO-1 has demonstrated cytoprotective effects *in vitro*[18,21] and *in vivo*.[43–45] Gene therapy also offers an opportunity for optimizing and targeting vectors involved in activation of HO-1. This line of treatment would involve screening patients for the HMOX1 gene promoter polymorphrisms to highlight individuals who present a higher risk of developing treatable diseases.[46]

Gaseous CO has been implemented in a variety of clinical trials that show a range of beneficial effects can be achieved at concentrations between 20–500 ppm. However administration of CO through the lungs has a number of drawbacks which must be addressed. Gaseous CO means rough concentration estimates and issues remain such as no tissue specificity and administration requirement of specialist equipment and facilities.[1] A valid alternative to gaseous CO is the use of drugs which carry and deliver CO to biological systems. These CORMs usually consist of transition metal carbonyls that release CO when stimulated by a specific stimuli.

1.4.1 Sepsis and Inflammation

Inflammation is a biological consequence of tissue responding to a harmful stimulus such as a bacterial infection. It is true that inflammation is a common condition associated with a multitude of chronic pathologies including cardiovascular disorders, diabetes, cancer and obesity.[47] It has been successfully demonstrated in cell cultures that the production of pro-inflammatory cytokines (TNF-α and IL-1β) induced by LPS is significantly inhibited when exposed to CO. Not only this, but the production of anti-inflammation cytokines (IL-10) is promoted.

The ability of CO to alleviate inflammation has been extensively demonstrated in several animals models and there is a good amount of evidence to suggest its potential therapeutic use for treatment of inflammatory related diseases. Mice treated with a lethal dose of endotoxins to bring about the liver disease fulminant hepatitis showed a

20–90 % recovery after inhalation of a CO-enriched atmosphere.[27,46] Another animal model study to note is treatment of CO from the ruthenium-based CORM ALF-492 (**2**, Figure 3) to mice suffering with cerebral malaria (an inflammation to the brain). The study found complete protection from malaria is CO dependent, with the CORM up-regulating the expression of HO-1.[48] In addition, Perrella and co-workers demonstrated that addition of the CORM rescued HO-1 deficient mice from sepsis.[45]

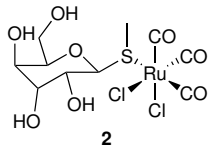

2

Figure 3: *In vivo* studies demonstrates CORM ALF-492 protects mice against cerebral malaria[48]

Therapeutic treatment of CO for inflammatory conditions such as human inflammatory bowel disease, Crohn's disease and ulcerative colitis have all received mounting interest. Plevy and co-workers studied the therapeutic modality of chronic colitis in mice models. Administration of gaseous CO was shown to improve chronic intestinal inflammation in IL-10 deficient mice.[44] Ford and co-workers established protective effects of 1 h/day gaseous CO (250 ppm) for inflammatory disease necrotizing enterocolitis in rat models.[49]

1.4.2 Cardiovascular Disease

Utilizing CO as a therapeutic agent for vascular disease seems the most plausible condition to treat due to ease of administration of gaseous CO. In the event of a serious vascular injury, such as myocardial infarction, revascularization therapy should be applied immediately to minimize and prevent further myocardial damage. HO-1 activity has been established to protect against hypoxia[50,51] and ischemia-reperfusion injury.[52,53] Exogenous CO diminishes vasoconstriction, leading to decreased blood pressure and improved circulation.

A number of studies demonstrate that chronic inhalation of low levels of CO attenuate

a variety of cardiovascular ailments. Otterbein *et al.* studied the suppression of intimal hyperplasia and graft infiltration in mice and rat models. Continuous exposure of CO (250 ppm) 1 hour before injury was shown to lessen the intimal hyperplasia associated with carotid artery angioplasty injury.[54] Nagai and co-workers reported ischemia-reperfusion injury of rat models was mediated following pre-inhalation of CO (1000 ppm, 24 h).[55] Vandier and co-workers reported chronic inhalation of CO attenuates hypoxic pulmonary artery hypertension (PAH).[56] In addition, Zuckerbraun *et al.* demonstrated gaseous administration of low concentrations of CO (250 ppm, 1 h/day) not only reversed PAH, but also reduced right heart hypertrophy and improved the general health of the animal models.

1.4.3 Organ Transplantation

Although organ transplantation has developed rapidly over the last few decades, the longer term outcome of this surgical technique remains poor. Despite advances in approach, specifically employment of new immunosuppression drugs and better post-operative care, many scientists now view organ transplantation as requiring therapeutic treatment to avoid organ rejection. CO offers a potential therapy for organ transplantation due to its ability to prevent ischemia/repurfusion injury and elicit cytoprotective effects.[16]

An organ is stored in a preservation solution prior to transplantation. Enrichment of the solution with CO not only increases the survival chances of the recipient and organ itself, but also diminishes oxidative injury and improves renal function and reduces histological injury well after the transplantation surgery.[46] Gaseous CO and CORMs have been successfully employed to deliver beneficial responses in various organ transplantations including heart,[16] lung,[16] kindey,[16] liver[57] and pancreas.[16] Direct administration of CO has also been shown to reduce the risk of reperfusion injury as a result of rejection of transplanted organ.[58]

1.5 Principles of Carbonyl Complexes

1.5.1 Bonding of CO

The atomic orbitals of the carbon and oxygen atom each consist of one spherical 2s orbital and three barbell-shaped 2p orbitals. The 2p orbitals point along the Cartesian axes ($2p_x$, $2p_y$ and $2p_z$) and are orthogonal to each other. The lobes of the 2p atomic orbitals are represented as different shades to indicate the different phases of the wave function. Atomic orbitals are able to combine constructively due to overlapping of two in-phase orbitals or destructively in an out-of-phase interaction.

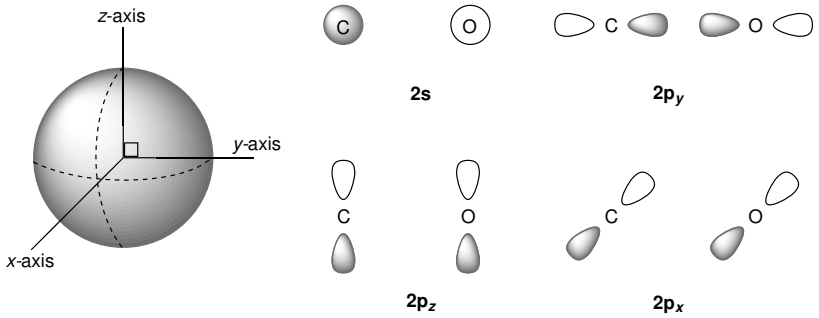

Figure 4: Representation of the atomic orbitals of CO

A constructive interaction results in the build-up of electron density between two nuclei and leads to the formation of a molecular orbital, which is of lower energy compared to the atomic orbitals. Destructive interactions do not result in a new bond, but formation of an anti-bonding molecular orbital, which lies at a higher energy than the atomic orbitals.

The two types of bonds formed in CO include one σ bond and two π bonds. The σ bond, which has cylindrical symmetry between the carbon and oxygen nuclei, is formed from the hybridization of the 2s and $2p_z$ orbitals in order to achieve the optimum shape for bonding. The σ* orbital is formed when the two atomic orbitals combine in a destructive, out-of-phase manner. This anti-bonding molecular orbital is situated predominantly on the carbon atom, and lies at a higher energy compared to the bonding molecular orbitals. Saturation of the σ* orbital results in a lengthening of the carbon

oxygen bond. In the resulting hybridizated orbitals, a non-bonding orbital arises from the pair of orbitals which point away from the C−O bond.

The number of atomic orbitals (2s and $2p_z$ on each nuclei) overlap to give an equal number of molecular orbitals (σ bonding, two σ non-bonding and σ* orbitals). Combination of the $2p_z$ atomic orbitals occur in much the same way as the $2p_y$ and $2p_x$, resulting in the formation of a π bond in the respective direction. The combination of these orbitals out of phase result in anti-bonding π orbital, which can participate in back donation to a metal centre. The contribution of the atomic orbitals of carbon and oxygen and the resulting molecular orbitals of CO are depicted in Figure 6.

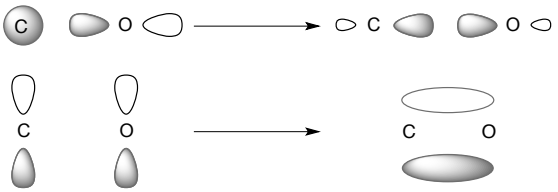

Figure 5: σ and π bond formation in CO

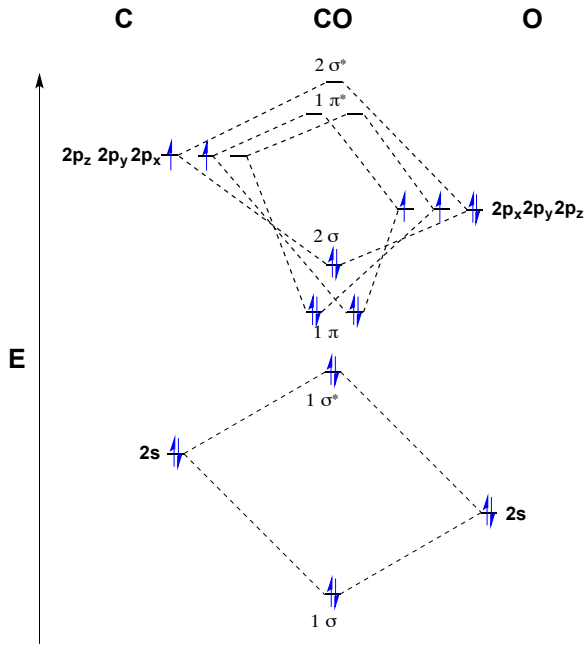

Figure 6: Molecular orbital diagram for carbon monoxide

1.5.2 Binding of CO to Transition Metal Centres

The majority of metal carbonyls exist as 18-electron species. This is a consequence of the bonding between the CO ligand and metal centre being covalent. The strength of the M−CO bond is dictated by the delocalisation of bonding electrons in the molecular orbitals formed between the metal and CO ligand. In carbonyl complexes, the CO ligand is bound to the metal atom by two types of bonding interaction (Figure 7). The lone pair of electrons situated on the carbon atom have the appropriate geometry to overlap with the atomic orbitals of the metal to form a σ (M−C) bond. The atomic orbitals of the metal used in this type of bonding are usually a combination of the s, p, d_{z^2} and $d_{x^2-y^2}$ atomic orbitals. The remaining filled d_{xy}, d_{xz} and/or d_{yz} orbitals of the metal are able to overlap with the empty π* orbital of the CO, and in doing so donate electron density back to the ligand (π-backbonding). This results in a strengthening (and therefore shortening) of the M−CO bond. As a result of the carbon anti-bonding orbital gaining electron density from the metal, the carbon-oxygen bond becomes weakened and lengthens. Early transition metal do not commonly form stable carbonyl complexes because they often exist in high oxidation states, and consequently do not contain filled d orbitals. Going across the period of the transition metal series the metal d orbitals become more electron rich. The increased electron density on the metal centre leads to the d orbitals becoming smaller and consequently unavailable for bonding. Therefore carbonyl complex become uncommon again towards the end of the transition metals series.

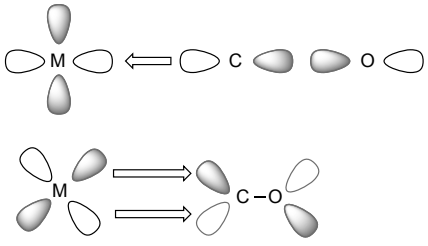

Figure 7: Carbon acts as a weak electron pair donor, forming a σ (M−C) bond (top). Empty π* orbital on carbon acts as π-acceptor, achieving π bonding *via* π-backbonding (bottom)

1.6 Development of Carbon Monoxide Releasing Molecules (CORMs)

1.6.1 Early CORMs

The investigation into using commercially available metal carbonyls as CO-releasing molecules (CORMs) was initiated by Motterlini *et al.* in 2000. Initial transition metal complexes screened for CORM viability (Figure 8) included iron pentacarbonyl ($Fe(CO)_5$, **3**), dimanganese decacarbonyl ($Mn_2(CO)_{10}$, **4**) and tricarbonyldichlororuthenium(II) dimer ($[Ru(CO)_3Cl_2]_2$, **5**). Direct addition of $Fe(CO)_5$ or $Mn_2(CO)_{10}$ to a myoglobin (Mb) solution did not display CO liberation *via* the conversion of Mb to carbonmonoxymyoglobin (MbCO). However both complexes released CO following exposure to light. This is in contrast to $[Ru(CO)_3Cl_2]_2$, which released CO spontaneously.

All of these early CORM models had problems. All are insoluble in aqueous media, $Fe(CO)_5$ and $Mn_2(CO)_{10}$ require photolysis to deliver CO and $Fe(CO)_5$ exhibits high toxicity issues. Further investigation into the CO release properties of $[Ru(CO)_3Cl_2]_2$ in DMSO revealed the complex dissociates into the tricarbonyl (*fac*-$[RuCl_2(CO)_3(DMSO)]$) and dicarbonyl (*cis-cis-trans*-$[RuCl_2(CO)_2(DMSO)_2]$) species following CO liberation. The amount of CO delivered was also low, liberating only $0.9\,mol^{-1}$ CO per CORM. Nevertheless, Motterlini *et al.* investigated the biochemical properties of both $Mn_2(CO)_{10}$ and $[Ru(CO)_3Cl_2]_2$. Neither complex displayed worrying cytotoxicity profiles in concentrations ranging from 40–210 $\mu mol\,L^{-1}$, and both displayed vasorelaxation activity operating *via* a cGMP-dependent pathway.[7]

Figure 8: Early CORMs investigated by Motterlini *et al.*[7,58]

With the desire to design a water soluble CORM, Motterlini *et al.* coordinated the biological ligand glycine to a ruthenium carbonyl metal centre. The glycinate ligand

rendered the complex less toxic and more water soluble. Indeed, $Ru(CO)_3Cl$(glycinate) (referred to as 'CORM-3') was the first example of a pharmacologically-active water-soluble CORM (**6**, Figure 8). CORM-3 has been effective in a number of *in vitro*, *ex vivo* and *in vivo* biological models.[8,26,58] However, there are issues associated with the complex which derive from its reactivity with water. Due to its rich aqueous chemistry, it is difficult to isolate in pure form. Infra-red (IR) analysis shows three distinct carbonyl peaks consistent with the *fac*-$Ru(CO)_3$ group at 2137, 2072 and 2058 cm^{-1}. The presence of an additional peak at 1985 cm^{-1} was initially thought to be a $Ru(CO)_2$ by-product. However, this was later discovered to be the result of a water-gas shift reaction of CORM-3, resulting from a deprotonation of the glycinate ligand (yielding $[Ru(CO)_2(COOH)Cl(glycinate)]^-$). Liberation of the carboxylic proton lowers the solution pH. Raising the pH results in the replacement of Ru−Cl by Ru−OH. Further acidification of $[Ru(CO)_2(COOH)Cl(glycinate)]^-$ results in liberation of the glycine ligand, yielding $[Ru(CO)_3Cl_3]^-$.[4]

1.6.2 Spontaneous CORMs

Spontaneous CO release usually proceeds *via* one of two possible mechanisms: thermal dissociation of the CO ligand or substitution of the CO ligand by a molecule present in the biological system. Thermal dissociation of CO involves the lengthening and breakage of the M−CO bond, creating a vacant site which can be occupied by a different ligand (usually a solvent molecule). For such a mechanism to proceed, the CORM itself must be relatively unstable to undergo thermal activation at biologically suitable temperatures (37 °C). Indeed, CO donation capabilities of CORMs which are thermally activated can be modulated *via* the *trans* effect. This observation was noted by Doctorvich and co-workers who reported a series of tetrachlorocarbonyliridate(III) complexes (**7**, Figure 9) harbouring nitrogen-based ligands *trans* to the CO.[59] Rate of CO release (rate of reaction) monitored under physiological conditions at 37 °C was observed to be approximately 20 times greater when 2-dimethylaminopyridine (π-acceptor) was *trans* to CO compared to Cl^- (weak σ-donor).

One CORM considered to release CO spontaneously as demonstrated *in vitro* and *in*

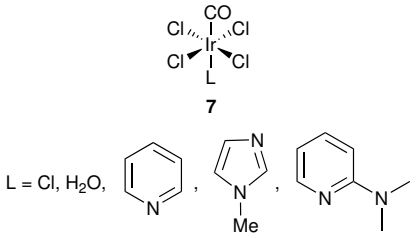

Figure 9: *Trans*-effect on CO release investigated by Doctorvich and co-workers[59]

vivo is CORM-3 (**6**, Figure 8). Although the precise CO release mechanism is not known, substitution of the chloride or glycinate ligand with an incoming electron-withdrawing molecule seems plausible. Indeed, CO release from **6** has been shown to be cysteine concentration dependant, suggesting an interaction between the CORM and the amino acid which facilitates CO release.[60] Of all the reported CORMs to date, **6** has received the most attention in terms of studies verifying its therapeutic actions. However, the ruthenium carbonyl complexes possesses a number of pitfalls which have ultimately hindered its clinical development. Not only are there issues regarding purification (mentioned above), but also its instability in aqueous solutions. This is a crucial setback in terms of drug delivery, causing the administrated CORM to release CO before reaching its medicinal target site. One strategy currently being employed to enhance cellular delivery is the generation of macromolecule-incorporating CORMs. Hubbell and co-workers[60] utilized polymeric nanocarriers in the sub-hundred nanometer range. The polymeric micelles comprised of a hydrophilic poly(ethylene glycol) block, a poly[$Ru(CO)_3Cl$(ornithinateacrylamide)] core responsible for CO release, and a hydrophobic poly(n-butylacrylamide) block (**8**, Figure 10). Comparing the CO release properties of **6** with the micelle-incorporated version found that the parent complex released slightly more CO (0.9 eq *vs* 0.76 eq). Of course, the high CO-loading capability of the micelle macromolecule means a significantly enhanced therapeutic efficiency of the system. This has been demonstrated *in vitro* where the CO-releasing micelle attributed significantly greater anti-inflammatory effects compared to **6** alone, which was surprisingly shown to be ineffective in this particular assay.

In another interesting study concerned with the *in vivo* CO release of **6**, Bernardes and co-workers reported spontaneous release of CO from metalloproteins.[61] Ruthenium complexes of the general formula $[Ru(CO)_3L_3]^{2+}$ are known to react with proteins

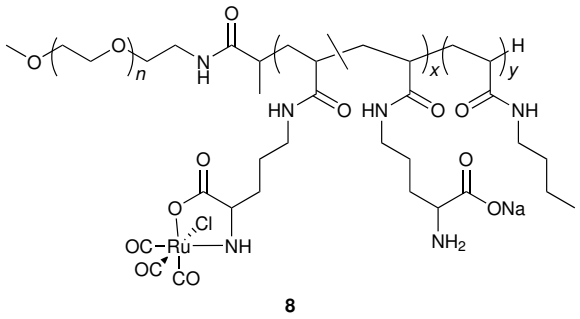

Figure 10: Micelles incorporating $Ru(CO)_3Cl$(amino acidate) structure reported by Hubbell[60]

yielding mono- and dicarbonyl ruthenium(II) protein adducts.[62] To this effect, Bernardes coordinated the hen egg white protein lysozyme (HEWL) to a $[Ru(CO)_2]^{2+}$ moiety *via* metalation of a surface-exposed histidine (His) functionality to yield HEWL-$[Ru(II)(CO)_2]$. The complex is thought to undergo a water-gas shift reaction, in which the released CO rapidly forms CO_2. In order to authenticate CO release, a 'turn on' fluorescent probe was employed which exhibits a fluorescent response specifically to CO. In developing metalloproteins which exhibit bio-selectively, reaction of $[Ru(CO)_2]^{2+}$ with bovine serum albumin (BSA) yielded BSA-$[Ru(II)(CO)_2]$, which was shown to release CO spontaneously in aqueous solution during *in vitro* studies using cultured cells and *in vivo* studies of mice models. Albumin has been shown to selectively accumulate in tumour tissues and offers an advantageous pathway to bio-distribute CO to cancer cells.

Romão and co-workers developed a series of CORMs of the general formula $[Mo(CO)_nCNR_{6-n}]$ with the aim of specifically protecting against acute liver failure. Previous work by Beck and co-workers examined the properties of a series of $Mo(CO)_3CNCH_2COOH$ complexes bearing different isocyanoacetate ligands.[63] These complexes were generally of low molecular size (an important consideration for drug development to ensure adequate cellular uptake, MW $<$ 500–600 g mol^{-1}) and displayed decent water solubility and stability under ambient conditions.

With this in mind, Romão explored the CO release properties of a series of molybdenum carbonyl complexes which varied with respect to number and structure of isocyanoacetate ligand, and consequently number of CO ligands (Figure 11).[64] *In vitro* studies of these

complexes revealed no uptake of the CORMs into the cultured cells. Biological activity was therefore evaluated *via in vivo* studies on mice proceeding acetaminophen-induced liver injury. Toxicity studies revealed complexes of the general formula $Mo(CO)_5L$ were lethal, with lower CO containing analogues ALF-785 (**9**) and ALF-795 (**10a**, Figure 11) producing no toxicity readings. CORMs **9** and **10a** administered to mice models of acetaminophen-induced liver injury resulted in a significant decrease in serum levels of the liver enzyme, alanine aminotransferase, which is associated with liver injury. Despite harbouring fewer CO ligands, **10a** activity superseded that of **9**. Following these encouraging results, the group generated a series of isocyanoacetate ligand derivatives to coordinate to a $Mo(CO)_3$ moiety to further enhance liver targeting and biological activity. One of the most influential factors demonstrated was the number of methyl substituents present on the isocyanoacetate molecule, with two methyl groups (ALF794, **10b**, Figure 11) producing the most desirable results.

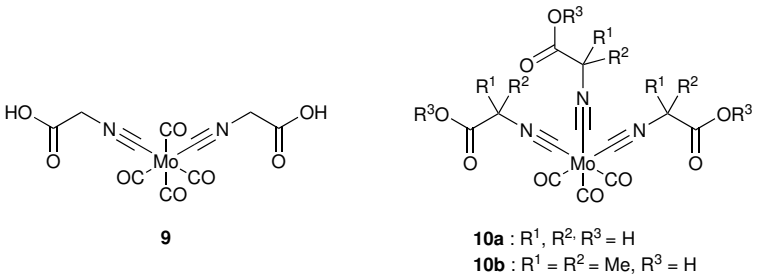

Figure 11: Molybdenum isocyanoacetate carbonyl complexes reported by Romão[64]

1.6.3 Enzymatic CORMs

Enzymatic activation of CORMs (so called ET-CORMs) represent a unique trigger mechanism by which CO is only liberated from the CORM in the presence of a specific enzyme. This strategy is particularly advantageous if an enzyme is overexpressed as a result of tissue damage or disease. In this sense, the ET-CORM becomes inducible (comparable to HO-1 activation) by responding to enzymatic changes in tissues to deliver site-specific therapeutic action. Incorporation of an ancillary ligand which features a functional group known to bind to a specific enzyme is likely to promote metabolic

decomposition of the drug, thereby triggering CO release. However, in designing ET-CORMs one must not only consider the enzyme's mode of action (substrate target) and location, but also its structure, in particular its active site. Enzymes which comprise of a haem co-factor may be unsuitable activators as the unbound CO will likely bind to the nearby haem, thereby inhibiting the therapeutic action of the ET-CORM. Furthermore, enzymatic activation could be achieved by a variety of different enzymes which all bind to the same substrate. Careful consideration of the ET-CORM coordination sphere may offer specific enzymatic binding and generate truly site-specific CO release.

The first explicit use of enzyme-triggered CO release was reported by Schmalz and co-workers, whom also coined the term 'ET-CORM'.[65] Earlier observation of the readily labile nature of an dienol-$Fe(CO)_3$ complex prompted the synthesis of a dienylester-$Fe(CO)_3$ precursor, which displayed greater stability under physiological conditions. Once the dienylester-$Fe(CO)_3$ precursor entered a cell it would be cleaved by intracellular esterases, converting back to the dienol-$Fe(CO)_3$ species which would then decompose, yielding Fe(III), the dienol ligand and three equivalents of CO (Figure 12, top). Schmalz put this concept into practise by investigating the esterase-triggered CO release of acyloxydiene-iron tricarbonyl complexes **11a**–**11b**, in addition to an diacetoxydiene-iron tricarbonyl complex **11c** and an esterase-insensitive control complex **11d** (Figure 12, bottom). ET-CORM activity was monitored *via* the myoglobin assay (Section 2.1.3) in the presence of an esterase enzyme. Under such conditions, CO liberation occurred. In the absence of any esterase, no CO release was detected.

Further to this work, Schmalz explored the structural influence of a series of acyloxy-cyclohexadiene-$Fe(CO)_3$ complexes on rate of CO release.[66] In this study, two regioisomers were used: one with the ester functionality positioned on the inner position of the diene ligand, and the other with the ester functionality at the outer position. Schmalz also assessed the influence of an aliphatic ester chain on rate of reaction. Their findings demonstrate that ester functionality at the outer position of the diene released CO quicker compared to those positioned at the inner position. Although the explanation for this remains unclear, it is thought the major influence stems from the stability of the formed intermediates (mechanism mentioned in Figure 12). Lengthening of the ester chain resulted in a significant decrease in rate of reaction. Indeed, *in vitro*

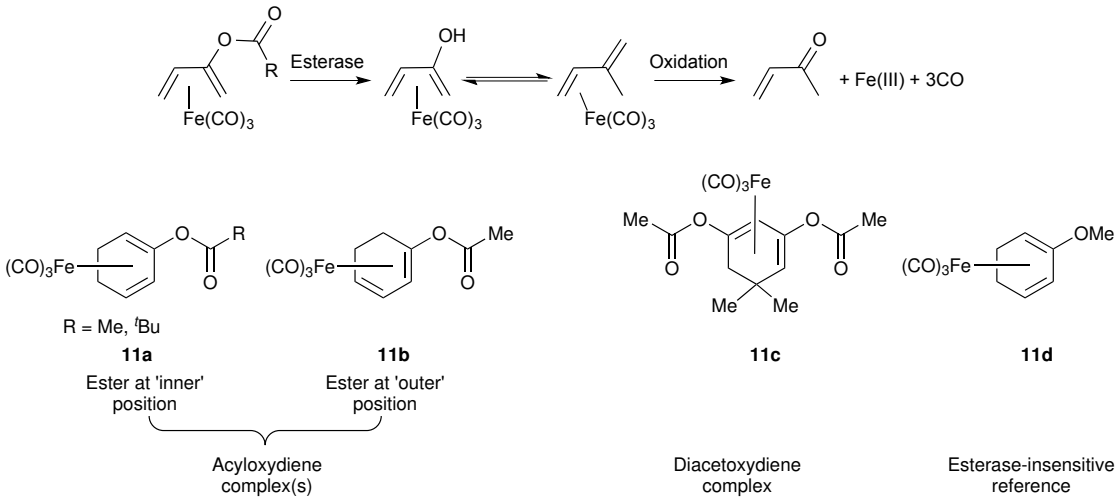

Figure 12: Top: Proposed enzymatic CO release mechanism. Bottom: $[Fe(CO)_3]$-based complexes used by Schmalz to establish ET-CORM activity[65]

studies revealed enzymatic release of CO was fastest from acetate (R = Me) groups with slower release from pivalates (R = ^{t}Bu) and palmitates ($C_{15}H_{31}$). In a further study, Schmalz and Yard[67,68] evaluated the biological activities of known ET-CORMs (**11a-11b**, Figure 13) with respect to toxicity, cytoprotective actions against hypothermic preservation damage and ability to inhibit TNF-α-mediated vascular cell adhesion molecule-1 (VCAM-1) expression. Similar to previous studies, the structure-activity relationship of ET-CORMs revealed ester functionality and position is crucial in influencing rate of reaction and biological response. Although none of the parent compounds from which the ET-CORMs are derived exhibited any cytotoxicity behaviour, the resulting ET-CORMs displayed significantly varying degrees of toxicity. Furthermore, only ET-CORMs with the mother compound cyclohexen-2-one (**11a** and **11b** series) displayed any protective actions against hypothermic preservation damage, with acetate ester functionality producing the greatest protection and palmitate the worst. All complexes reported a decreased in TNF-α-mediated VCAM-1 expression.

1.6.4 Co-Drug Assisted Release CORMs

Many research groups have explored CORM activation *via* administration with a co-drug. This strategy has been most successfully demonstrated in combination with

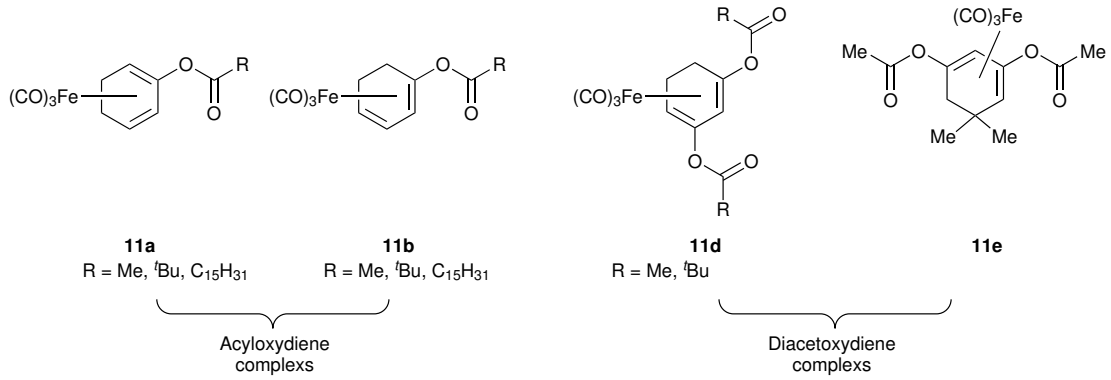

Figure 13: ET-CORMs investigated by Schmalz and Yard[67,68]

metal-based CORMs. CO can be readily substituted *via* an associative mechanism by an approaching ligand: the incoming ligand forms a new M−L bond, increasing the coordination number of the complex. This leads to the elongation and breakage of the M−CO bond. Activation of a pro-drug (CORM) through treatment with a co-drug will inevitably result in the generation of intermediate species following liberation of CO. One must ensure that not only the pro- and co-drugs are non-toxic, but any subsequent intermediate(s) display minimal detrimental effects towards tissues.

Liu and co-workers reported the synthesis of a diiron hexacarbonyl species featuring a bidentate thioglycerol bridge (**12**, Figure 14).[69] The presence of four hydroxyl groups on the bridging ligands arguments excellent water solubility. CO release was achieved *via* substitution by co-drug, cysteamine (CysA). The use of thioglycol and CysA is appropriate, with both having been used in medicinal applications, any emerging intermediate species should exhibit little/no harmful effects. However, the traditional myoglobin assay (Section 2.1.3) could not be employed here as the presence of the excess reducing agent (sodium dithionite) prompted CO release from the diiron complex. Spectroscopic analysis of the CO release behaviour revealed loss of one equivalent of CO following substitution of CysA, with further loss of CO resulting in the formation of a monoiron (Fe(II)(*cis*-CO)$_2$) species. The parent diiron complex consists of an 'Fe(I)Fe(I)'-core, which indicates an oxidative mechanism to form the later intermediates. Since the spectroscopic experiments were carried out in an inert atmosphere, Liu speculated the most probable source of oxidation was the labile thiol proton of the CysA co-drug. This idea was supported spectroscopically as the protonated and deprotonated forms were

identified as intermediate species following CO release. Under an open atmosphere, Liu reflected a similar first-step labilisation of CO by CysA would occur, followed by rapid oxidative destruction caused by molecular oxygen.

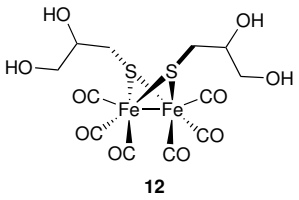

Figure 14: Diiron hexacarbonyl activated by CysA, reported by Liu and co-workers[69]

1.6.5 PhotoCORMs

An attractive and selective strategy is the photochemically-activated loss of CO from photosensitive CORMs. PhotoCORMs are inherently stable in the dark, and only release CO in response to stimulation by incident light of a specific wavelength. They have obvious topical applications, such as treatment of skin diseases, transdermal delivery of CO, or localised CO treatment to organs, tissues or tumours *via* photodynamic therapy technologies. The wavelength (and therefore energy) of incident light required to break the M−CO bond is of significant importance in the development of photoCORMs. The majority of carbonyl complexes will decompose following irradiation of ultra-violet (UV) light, thereby releasing their load of CO. However activation by UV light is damaging to the biological target and elicits poor tissue penetration depth. Excitation from longer wavelengths of light are less biologically harmful and can penetrate deeper into the skin, allowing the CORM to target sites deeper inside solid tissue.[70] Preferably, a photoCORM would be activated by near-infrared (near-IR) irradiation, as this region of the electromagnetic spectrum allows for the greatest tissue penetration without causing harm to tissues.[71] The development of photoCORMs has recently been reviewed in detail.[72]

The first explicit use of light to act as a trigger mechanism for CO release, and indeed the first coined use of the term 'CORM' came from Motterlini *et al.* in 2002.[7] As mentioned

above, simple metal carbonyls $Fe(CO)_5$ and $Mn_2(CO)_{10}$ were shown to only release CO when irradiated with 'cold light' over approximately one hour. Of course, these systems were not specifically designed to adhere photoCORM behaviour. Early photoCORMs designed specifically to release CO in response to stimulation from light required high energy, UV irradiation to liberate the bound CO. What constitutes a UV-activated or visible light activated photoCORM is not straight-forward. Typically one would classify the molecule as visible light activated if the absorption for the electronic transitions lie above 400 nm. However, commonly these electronic transitions are broad and may overlap between the UV and visible regions of the spectrum. For the purposes of this thesis, photoCORMs are divided based on the light source used in practical applications to release CO.

The first example of a CORM specifically designed to utilize light to release CO was reported by Schatzschneider and co-workers in 2008.[73] The reaction of $Mn(CO)_5Br$ with tris(pyrazolyl)methane (tpm) yielded $[Mn(CO)_3(tpm)]^+$ (**13**, Figure 15). The cationic manganese centre is water soluble and bears three CO ligands. The tpm ligand framework was chosen due to its synthetic ease. Also, further functionality could be introduced to the complex *via* substitution of the acidic methine proton. Upon irradiation with UV light (365 nm), the complex releases approximately two equivalents of CO and displayed promising anti-cancer properties against human colon cancer cells. However, when the photo-triggered CO release was surveyed by ultrafast laser spectroscopy, it was revealed that only one of the three CO ligands is photolabile. The loss of subsequent CO ligands was thought to most likely be a consequence of manganese oxidation.[74,75] Functionalisation of the tpm ligand framework (**14**, Figure 15) offered a gateway into achieving uptake by a specific type of cell. This type of targeted delivery has obvious advantages, especially when developing anti-cancer treatments. With this in mind, Schatzschneider successfully employed Pd-catalysed Sonogashira cross-coupling and alkyl-azide click chemistry to coordinate peptides to the tpm-manganese(I) tricarbonyl complex.[76] The resulting peptide CORM was shown to have a similar CO release profile to that of the parent complex. Using a similar approach, the group later successfully attached the tpm-manganese(I) complex to azido-modified silicium dioxide nanoparticles to act as a carrier. The resulting complex was shown to have similar CO

release properties to that of the parent complex.[77]

With the aim of gaining an insight into the extent to which overall charge and ligand sphere influenced CO release, Berends and Kurz performed a comparative study using the cationic species $[Mn(CO)_3(tpm)]^+$ (**13**, Figure 15) synthesised by Schatzschneider, and the neutral complex $[Mn(CO)_3(bpzaa)]$ (where bpzaa = *bis*-(pyrazolyl)acetic acid)(**15**, Figure 15).[75] Using a multi-analytical approach, incorporating IR, UV/Vis and electron paramagnetic resonance (EPR) spectroscopies, the pair established a step-wise mechanism by which CO ligands are replaced by solvato ligands. The absorption maxima for each complex lies at 349 nm and 361 nm, respectively, with loss of two equivalents of CO following UV (365 nm) irradiation. The postulated photoproducts undergo oxidation of the manganese metal centre without loss of the ligand architecture (IR data indicate a *cis*-$Mn(I)(CO)_2$ species).

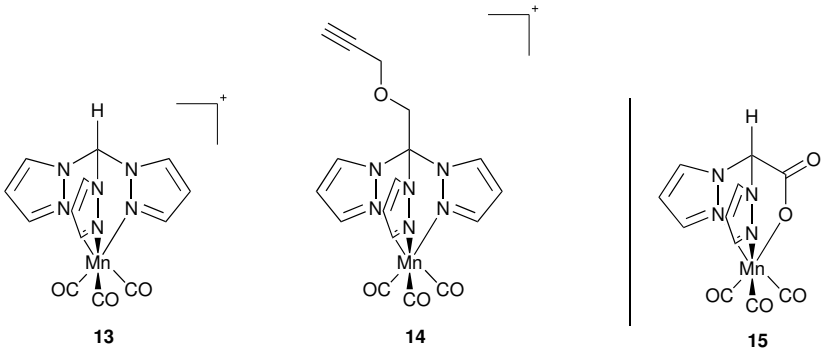

Figure 15: First photoCORM (left) and subsequent functionalised derivatives (middle) reported by Schatzschneider[76,77] with the neutral comparison complex (right) synthesised by Berends and Kurz[75]

The first documented use of the term 'PhotoCORM' came from Ford and co-workers in 2010.[78] Ford reported an air- and water-soluble tungsten(0) carbonyl complex bearing a tris(sulphonatophenyl)phosphine ligand (**16**, Figure 16). The complex comprised of five CO ligands, but upon UV irradiation (305–405 nm) only released one equivalent of CO. Following photolabilisation of CO, a water molecule coordinates to the vacant site. The slow liberation of additional CO from this secondary species is thought not be to photochemical, but a result of the oxidation of the tungsten metal centre.

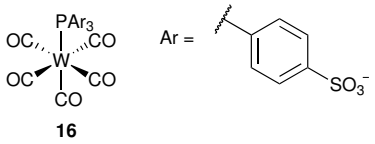

Figure 16: Tungsten-based photoCORM reported by Ford and co-workers[78]

Employing alkynyl chemistry, Lynam and co-workers successfully introduced a biologically-compatible sugar ligand onto a molybdenum carbonyl complex, yielding **17** (Figure 17).[79] The reported cyclopentadienyl-molybdenum photoCORM displayed excellent water solubility and was shown to release CO slowly in aqueous media. However, rate of reaction rapidly increased when the complex was irradiated with UV light (325 nm). In both instances, approximately two equivalents of CO were lost.

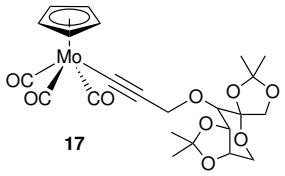

Figure 17: Mo-fructopyranose photoCORM reported by Lynam and co-workers[79]

The Spingler group developed a series of manganese and rhenium systems which incorporated tripodal nitrogen ligands bearing a central phosphorus linking atom.[80] The rhenium complexes displayed no absorption maxima greater than 320 nm and exhibited no photoCORM activity. The manganese complexes were shown to be stable in the dark whilst in the presence of myoglobin. Photoactivation at 365 nm showed ligand-dependent loss of CO within 60 minutes. Complexes featuring the imidazol-2-ylphosphane (**18**, Figure 18) ligand architecture liberated two equivalents of CO per metal centre, whereas those featuring the imidazol-4-ylphosphine (**19**, Figure 18) ligand framework only released one equivalent.

Extending on this work, Kunz synthesised two related 2-hydroxypropyl methacrylamide (HPMA)-based polymers to coordinate to an $Mn(CO)_3$ core.[81] The idea behind incorporating large macromolecules is to hone the delivery capabilities of the system. This is especially effective in the selective toxicity of cancer cells as such macromolecules are known to accumulate in tumour tissues, as described by the enhanced permeability

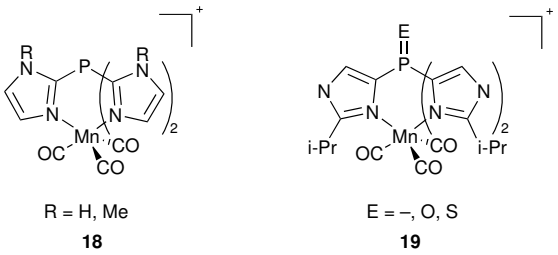

Figure 18: Manganese photoCORMs developed by Spingler[80]

and retention effect. The polymeric carrier coordinates to the manganese core *via* a bis(pyridylmethyl)amine architecture. The corresponding $Mn(CO)_3$–polymer conjugates (**20**, Figure 19) displayed photolytic release of CO under UV conditions. However, due to the polymer loading, turbidity of the solution may have influenced the myoglobin assay data.[82]

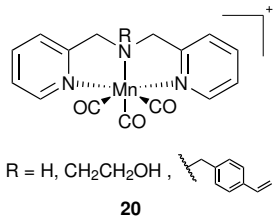

Figure 19: Polyermic bis(pyridylmethyl)amine-functionalised manganese complexes reported by Kunz[81]

Kodanko and co-workers reported the synthesis of the Fe(II) dicationic photoCORM, $[Fe(CO)(N_4Py)]^{2+}$ (**21**, Figure 20).[83] The complex exhibits excellent water-solubility and was shown to release CO in a triggered fashion following UV irradiation (365 nm). Investigating the biological applications of the photoCORM revealed photoinduced cytotoxicity behaviour against prostate cancer cell cultures. Further modification of the transition metal motif by attaching a peptide molecule (Ac-Ala-Gly-OBn) was achieved, although no CO release data, nor influence of the peptide on tissue- or cell-specific drug uptake was included.

Extending their earlier work on $Mn(CO)_4(C\wedge N)$ systems (where C∧N = *ortho*-metallated 2-phenylpyridine or benzoquinoline), Fairlamb and co-workers explored the CO release behaviour of a related $Mn(CO)_4(C\wedge N)$ complex (**22**, Figure 21).[84] The UV-activated

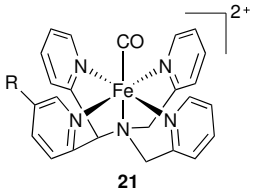

Figure 20: Monocarbonyl iron photoCORM reported by Kodanko and co-workers (R = H, Ac-Ala-Gly-OBn)[83]

(365 nm) photoCORM is thermally stable in the dark and releases up to three equivalents of CO. The photorelease behaviour was shown to operate *via* a step-wise process, by which the liberation of CO could be switched 'on and off' simply by starting/stopping the UV irradiation. Cell viability experiments pre- and post-irradiation revealed none of the degradation species infer toxicity issues to the cell cultures.

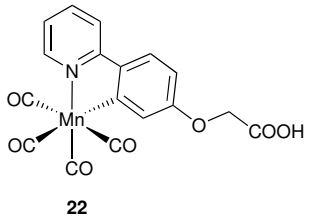

Figure 21: Manganese photoCORM reported by Fairlamb and co-workers[84]

Schatzschneider and co-workers furthered their photoCORM work on a range of ruthenium based structures incorporating 2,2′-bipyridine (bpy) ligands and related structures (**23-25**, Figure 22).[85] The strong MLCT (metal-to-ligand charge transfer) transitions make the ligand ideal for photoCORM development. Furthermore, the ligand framework can be readily modified to introduce biologically compatible functionalities. In this instance, attachment of a peptide nucleic acid (PNA) to the 2-(2′-pyridyl)pyrimidine complex yielded **23** (where X = N, R^1 = H and R^2 = PNA). Illumination of all complexes at 365 nm resulted in the liberation of one equivalent of CO. In the case of the PNA-derivative, the CO release behaviour remained identical to that of the parent complex.

An interesting sawhorse type ruthenium complex bearing carboxylic and amino acid molecules within the coordination sphere was developed by Zhang and co-workers.[86]

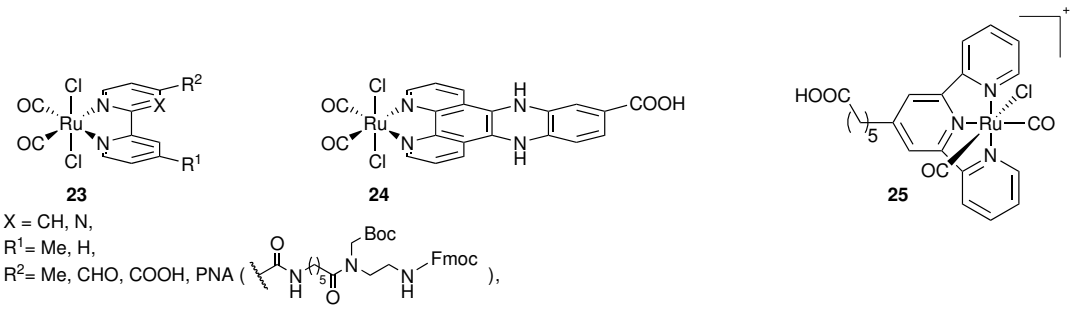

Figure 22: Ruthenium bi- and ter-pyridine photoCORMs derivatives reported by Schatzschneider and co-workers (Boc = *tert*-butyloxycarbonyl, Fmoc = 9-fluorenylmethyloxycarbonyl)[85]

The sawhorse complex, namely [Ru(μ^2-carbonylato)(O(C=O)R)$_2$(CO)$_2$]$_2$ (**26**, Figure 23) released CO when triggered by LED (light emitting diode) UV irradiation (365 nm). rate of reaction was shown to be dependent on the nature of the bridging ligand, which was varied from acetato- to arylcarbonxylato. Photolysis monitored by IR spectroscopy revealed the growth a new peaks following disappearance of peaks in the carbonyl region, which suggests the formation of a stable photoproduct. These intermediates were further analysed by ESI-MS, which indicated the replacement of one labile axial ligand with a solvent molecule.

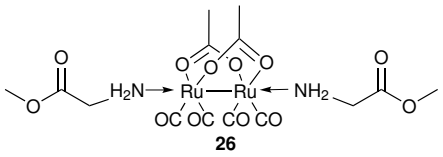

Figure 23: Sawhorse rutheium photoCORM reported by Zhang[86]

An essential feature of any given (photo)CORM is that its breakdown products ('*i*CORMs') post CO release must be non-toxic and excretable. One of the leading strategies to generate inactive, isolatable *i*CORMs is to employ ligands which incorporate more donor groups than there are labile CO ligands (Scheme 2). The idea being that once one CO ligand has been release from the metal centre, the additional donor group of the ligand, preferentially at the end of a pendant 'arm', will coordinate to the metal centre.

Schatzschneider and co-workers developed such photoCORMs using the tetradentate

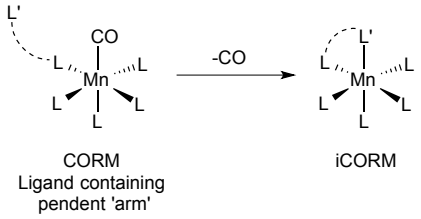

Scheme 2: Scheme depicting (photo)CORMs ligand framework comprising of additional pendant donor 'arms' which are able to coordinate to the metal centre following CO release

ligand, tris(2-pyridylmethyl)amine (tpa). The resulting cationic manganese photoCORM bears three labile CO ligands (**27**, Figure 24).[87] The complex is stable in the presence of myoglobin in the dark for up to 16 hours. Following UV illumination (365 nm) approximately three equivalents of CO were released. However, when kept in the dark for only 1 hour pre UV light activation, only two equivalents were photo-released. This suggests that release of the third CO equivalent operates *via* a non-photochemical mechanism. Of course, the developed tpa ligand only contains one pendent 'arm', which limits the number of isolatable *i*CORMs as this particular species can lose up to three CO equivalents. Schatzschneider reports that synthesis of a novel hexadentate ligand with one pendant donor group per CO is currently under preparation in their laboratory.

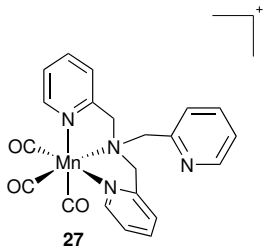

Figure 24: Manganese photoCORM with tetradentate ligand, including one pendent 'arm', reported by Schatzschneider and co-workers[87]

A series of photoactive tetracarbonyl manganese complexes (**28**, Figure 25) harbouring a 2-phenylpyridine ligand architecture have been developed by Fairlamb and co-workers.[88] The 2-phenylpyridine ligands were generated using a Suzuki-Miyaura cross coupling

reaction. Varying the substituent on the 4-position of the phenyl ring led to modulation of CO release properties. All complexes were shown to be stable in the absence of light, and only released CO to myoglobin following irradiation using a TLC lamp (365 nm). Investigations of photoCORM behaviours using an LED irradiation system operating at 365 nm and 400 nm led to significant increases in CO release capabilities.

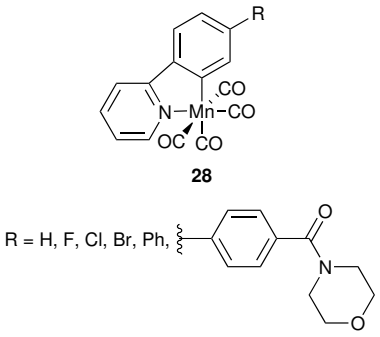

Figure 25: Tetracarbonyl phenylpyridine manganese photoCORMs reported by Fairlamb and co-workers[88]

The design of visible light activated photoCORMs has been at the forefront of field development during the past few years. Transition metal carbonyl complexes which partake in distinct metal-to-ligand charge transfer (MLCT) transitions have been shown to facilitate CO labilisation from the metal centre.[89] Indeed, the photoreactivity of a given metal complex is indicative of the electronic transitions possible. Ligand field transitions still occur, but are unlikely to cause photodissociation of CO due to the relatively high energy of the M−CO anti-bonding orbitals (Figure 26).

MLCT transitions, which are of high intensity and spectroscopically allowed, arise from the excitation of electrons from orbitals predominantly of metal character to orbitals predominantly of ligand character (Figure 27). This decrease in the electron density of the metal t_{2g} orbitals weakens the complex's backbonding capabilities and therefore facilitates CO loss. Complexes which are able to undertake such transitions generally featuring electron rich d orbitals and possess ligands fostering low lying empty π^* orbitals (such as pyridines or diimines).

The more successful candidates consist of d^6 metal centres, including Mn(I), Re(I), Fe(II) and Ru(II). Of course, success in designing visible light activated photoCORMs also

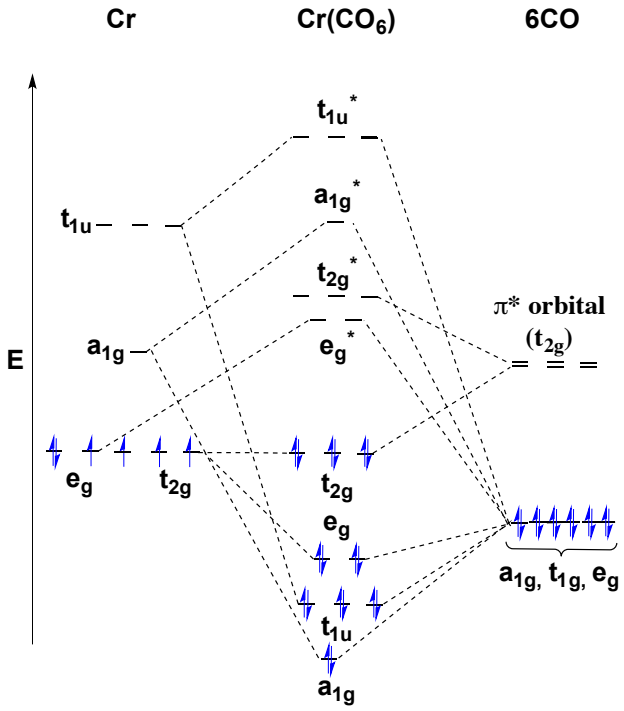

Figure 26: Molecular orbital energy level diagram for carbonyl complex, $Cr(CO_6)$

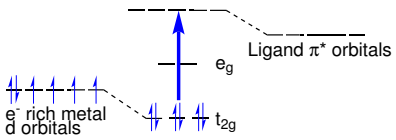

Figure 27: Metal to ligand charge transfer (MLCT) of an octahedral d^6 complex

revolves around the synthesis of photosenstive ligands suitable for coordination to metal centres, which are able to facilitate MLCT transitions. The design principles which allow for visible light driven CO release can be rationalised using DFT (density functional theory) and TD-DFT (time-dependent density functional theory) calculations.[90]

Surveying the literature, the first demonstrated visible light activated release of CO was reported by Westerhausen and co-workers in 2011.[91] The previously known iron complex, dicarbonylbis(cysteamine)iron(II) (so-called CORM-S1, **29**, Figure 28) was shown to release approximately two equivalents of CO following irradiation with visible light (470 nm). The complex architecture consists of two cysteamine ligands, which were purposely chosen due to their degradation to cysteine. Interestingly, the complex bears no organic chromophore ligand framework, which limits the possibility of further modification.

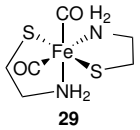

Figure 28: CORM-S1, developed by Westerhausen and co-workers[91]

Inspiration for photoCORM development can originate in a number of different forms. Ford and co-workers built theirs on the basis of *fac*-Re(bpy)$(CO)_3(X)^+$ (bpy = 2,2′-bipyridine, X = halide) complexes, which are well-known CO oxidation catalysts and exhibit luminescent properties.[92] Probing the CO release behaviour of these complexes revealed photodissociation (405 nm) of one equivalent of CO. It is important to note that the quantum yield (Section 2.2.1) in the UV-region (365 nm, 0.21) is greater than the visible range (405 nm, 0.11). Due to the complexes exhibiting poor water solubility, Ford incorporated the hydroxylated ligand $P(CH_2OH)_3$ to solubilse the complex. Scheme 3 shows the active photoCORM (**30**) and photoproduct (**31**). Notably, photolysis of the rhenium complex leads to a detectable shift in the luminescent band. In aqueous solution a strong emission band at 515 nm is observed, which red-shifts to 585 nm for the photoproduct. This provides a crucial insight into the cellular uptake behaviour of the photoCORM *in vitro*.

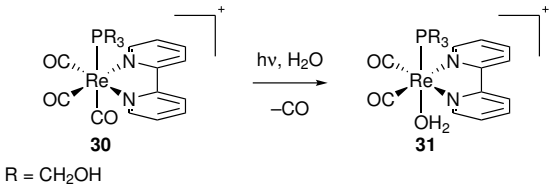

Scheme 3: Luminescent rhenium photoCORM reported by Ford and co-workers[92]

Photorelease of CO from the hydrogenase-inspired $Na_2[(\mu\text{-}SCH_2CH_2COO)Fe(CO)_3]_2$ was reported by Fan and co-workers.[93] This diiron system consists of six labile CO ligands and a water solubilizing dithiolate bridge containing carboxylate end groups (**32**, Figure 29). When shielded from light, the complex is both air- and water stable. In the presence of strong donor molecules (such as PMe_3), the complex releases CO *via* a nucleophilic substitution reaction. Photochemical liberation of all six CO ligands was achieved within 30 minutes following broadband visible light irradiation. Quantification

of CO release behaviour was reported following irradiation at 390 nm.

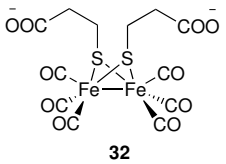

Figure 29: Anionic diiron-based photoCORM reported by Fan and co-workers[93]

Quantification of breakdown products post CO release, in terms of structure, toxicity and biological activity, is an integral part of understanding CORM behaviour. One leading strategy to contain any subsequent photoproducts is to bind the metal-ligand moiety to a macromolecular carrier. This methodology was utilised by Smith and co-workers, who developed a number of dendrimer macromolecules bound to an $Mn(CO)_3$-core.[94] Smith reported two metallodendrimers: a tetranuclear and octanuclear $Mn(CO)_3$ functionalised system (**33**). In addition, a mononuclear analogue (**34**) was synthesised in order to quantify the scaling effect of additional metal centres (Figure 30). Photochemical activation at 410 nm liberated two out of the possible three CO ligands per metal centre, with the dendrimers taking approximately twice as long to release CO compared to the monomeric system.

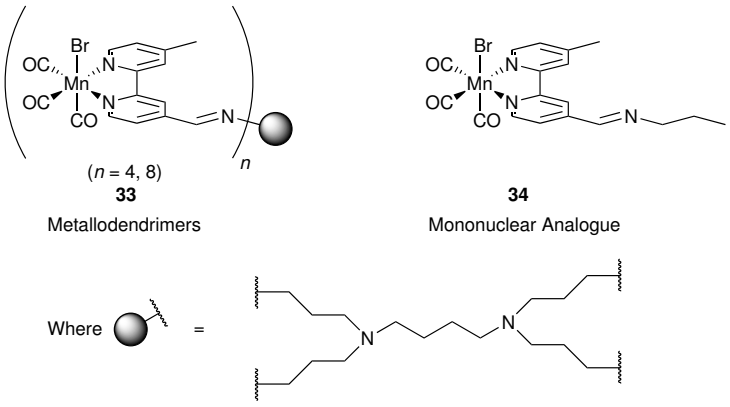

Figure 30: Manganese-based matallodendrimers and monomeric analogue reported by Smith and co-workers[94]

Development of photoCORMs which incorporate the biocompatable scaffold vitamin B_{12} was originally examined by Bogdanova and co-workers in 2012.[95] Reaction of

$[Re(CO)_2Br_4][Et_4N]_2$ with cyanocobalamin (vitamin B_{12}) resulted in the formation of a 17-electron rhenium dicarbonyl species (so-called 'Re-B_{12}CORM', **35**, Figure 31). Such systems exhibit superior water solubility and biocompatability compared to the parent metal complex. Furthermore, the Re-B_{12}CORM derivatives display improved stability in aqueous aerobic media as well as cytoprotective actions against ischemia-reperfusion injury. The complex does release CO, but not under photoillumination. More recently, Bogdanova and co-workers revealed cellular uptake problems with the Re-based system.[96] Development of a vitamin B_{12} scaffold capable of intracellular uptake of an inorganic motif was achieved by complexation of a $Mn(CO)_3$-core with the vitamin B_{12} molecule *via* the ribose sugar moiety (so-called 'Mn-B_{12}CORM', **36**, Figure 31). Photoinduced CO release from Mn-B_{12}CORM was firstly probed *via* IR spectroscopy. When shielded from light, no observable changes occurred. Exposure to blue LED (470 nm) illumination resulted in a steady decrease of all carbonyl peaks over three hours. Furthermore, exposure to green (496 nm) Ar laser irradiation resulted in slower labilisation of the three CO ligands. In order to verify the cellular uptake issue with Re-B_{12}CORM had been addressed, the cytoprotective actions of Mn-B_{12}CORM were demonstrated on a cell culture of fibroblasts.

Bengali and co-workers examined the photorelease properties of a $Mn(CO)_3$ fragment supported by the sterically hindered DAB (1,4-diaza-1,3-butadiene).[97] The complex in question, namely *fac*-[$Mn(CO)_3$(^{i}Pr$_2$Ph−DAB)] (**37**, Figure 32) (where ^{i}Pr$_2$Ph − DAB = *N*,*N*′-bis(2,6-di*iso*propylphenyl)-1,4-diaza-1,3-butadiene) is unstable when exposed to ambient light. In such conditions, a thermal reaction occurs which results in the separation of the diimine ligand with formation of $Mn(CO)_4Br$. The complex has an absorption maxima at 582 nm, and CO release behaviour was monitored *via* IR spectroscopy following visible light (560 nm) illumination. The IR spectrum showed a gradual decrease in all carbonyl peaks, with no evidence of intermediate photoproducts forming. Bengali speculates the photolytic cleavage of CO is driven by a MLCT transition originating from a combination of the Mn−CO π and bromide p orbitals to the π* orbitals of the diimine ligand. The outcome of which reduces the extent of back-bonding to the CO ligand which facilitates CO loss. Extraction of the bromide by $TlPF_6$ in a CO atmosphere yielded the cationic species, [$Mn(CO)_4$(^{i}Pr$_2$Ph-DAB)]$^+$

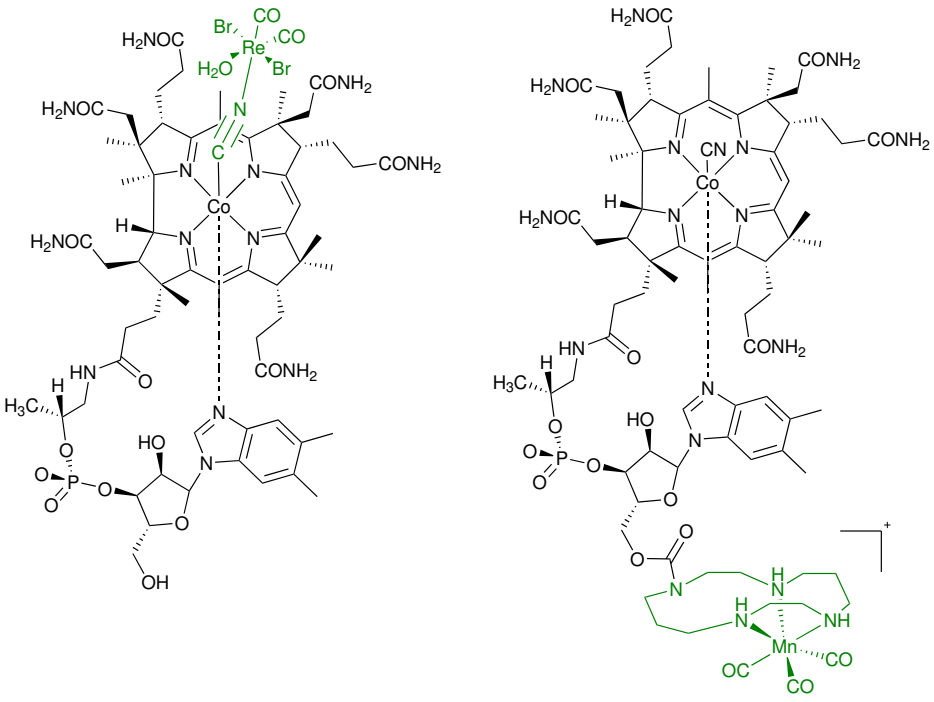

Figure 31: Left: Re-vitamin B_{12} CORM attached *via* a C≡N linkage.[95] Right: Mn-vitamin B_{12} PhotoCORM ligated *via* the ribose moiety[96]

(**38**, Figure 32). Dissolution results in loss of the axial CO by the solvent molecule. Furthermore, the cationic analogue displays enhanced thermal reactivity resulting in loss of CO. However, due to the loss of the halide, the ligand does not dissociate from the complex in ambient light. With respect to its photolytic CO release, the latter complex releases CO at a decreased rate compared to the parent complex.

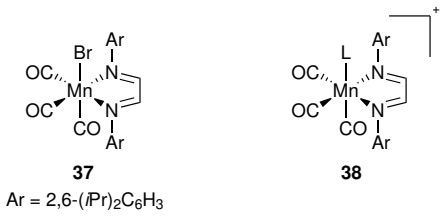

Figure 32: Left: Neutral manganese tricarbonyl complex including the sterically bulky DAB ligand. Right: Related cationic manganese tetracarbonyl complex

Work done by Mascharak and co-workers established absorptivity of carbonyl complexes can be systematically increased by extending the conjugation system of the ligand

framework (Figure 33).[98] Using a variety of structurally similar ligands featuring a pyridine and quinoline moiety, as well as conjugated aromatic nitrogen donors, Mascharak synthesised a series of manganese(I) carbonyl complexes which progressively displayed a red shift of the absorption band. These ligands all coordinated to the manganese(I) metal centre in a bidentate fashion, with the sulfur containing ligand (qmtpm) eliciting the most substantial shift furthest into the visible. A key observation of this work is the significant red shift observed when comparing complexes bearing halide ligands and those featuring other donors. For example, the electronic transition of *fac*-[Mn(qmtpm)$(CO)_3$(MeCN)][ClO_4] at 435 nm is significantly shifted to 535 nm in *fac*-[Mn(qmtpm)$(CO)_3$Br].

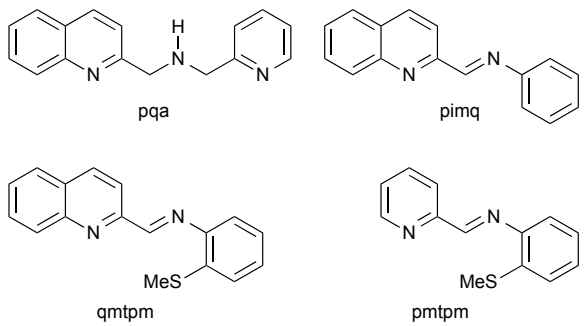

Figure 33: Bidentate ligands containing coordinating nitrogen donors synthesised by Mascharak[98]

Mascharak later synthesised ruthenium analogues featuring the qmtpm ligand, which coordinated in a meridional fashion (Figure 34).[99] In contrast to the manganese species (where the ligand binds in a bidentate fashion), in the ruthenium complexes the ligand coordinates in a tridentate fashion. This particular study focused on the photoactivity of two complexes, $[Ru(Cl)(CO)(qmtpm)(PPh_3)]^+$ (**39**) and $[Ru(Cl)(CO)_2(qmtpm)]^+$ (**40**) following irradiation in the 300–450 nm wavelength range. The CO release behaviour of both complexes was examined in acetonitrile. In the case of **39**, small spectral changes were observed when the complexes was kept in the dark in the presence of myoglobin. Slow release of CO was thought to facilitate through the strong *trans*-effect of the PPh_3 ligand. Indeed **40**, which contains no PPh_3 ligand is fully stable in such conditions. rate of reaction was shown to be dependent on the illumination wavelength. Moreover,

visible light activated CO release was only achievable with the PPh_3-containing complex. Irradiating with a light cut-off at 380 nm yielded a significantly enhanced rate of reaction compared to a cut-off filter at 440 nm.

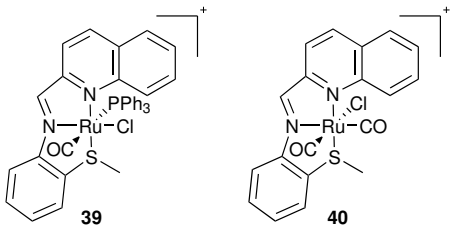

Figure 34: Ruthenium-based photoCORMs reported by Mascharak[99]

Following this work, Mascharak described the photorelease behaviour of two complexes featuring the bidentate ligand 2-phenylazopyridine (azpy), namely, *fac*-[MnBr(azpy)$(CO)_3$] (**41**) and *fac*-[Mn(azpy)$(CO)_3(PPh_3)]^+$ (**42**, Figure 35). The azpy ligand was specifically implemented into the coordination sphere due to its strong π-acidity in order to enhance MLCT transitions in the visible region. In this study, substitution of a halide ligand with PPh_3 resulted in a blue-shift in the absorption spectrum, along with a decrease in rate of reaction. This observation is consistent with the expected behaviour of systems which utilise π-acceptor ligands, which are known to stabilise low-lying orbitals by withdrawing electron density from the metal centre, resulting in an increase in the energy required for MLCT transitions. Photorelease of CO from **41** upon exposure to visible light (with a 520 nm cut-off filter) showed quick CO release within minutes.

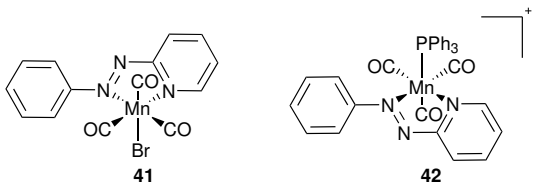

Figure 35: *fac*-[MnBr(azpy)$(CO)_3$] and *fac*-[Mn(azpy)$(CO)_3(PPh_3)]^+$ reported by Mascharak[100]

More recently, Mascharak made use of the benzothiozole-derivative ligand, 2-(2-pyridyl)-

benzothiazole (pbt).[101] Like other benzothiozole ligands, pbt exhibits strong anti-tumour activities and acts as a stable fluorophore. By complementing these two characteristics of the ligand architecture, Mascharak developed the biologically trackable, anti-cancer photoCORM, *fac*-[$MnBr(CO)_3$(pbt)] (**43**, Figure 36). This complex displays a 'turn-on' fluorescent nature following labilisation of CO. Illumination with broadband visible light causes dissociation of the pbt ligand, which in turn is responsible for the fluorescence observed. This phenomenon provides a pathway to quantify uptake of the drug to target cells. Fluorescence imagining studies with human breast cancer cell lines revealed loss of the pbt ligand from the metal centre, along with a 50 % reduction in cell viability following visible light irradiation.

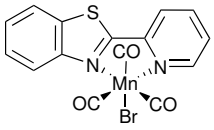

43

Figure 36: Fluorescent manganese photoCORMs reported by Mascharak[101]

Delving into the rational design principles for visible light activated CORMs developed by Mascharak, Zobi and co-workers analysed the absorption shift of *fac*-$Mn(CO)_3$ complexes featuring 2,2′-azopyridine ligands modified with either an electron-donating or electron-withdrawing substituent (**44**, Figure 37).[102] As mentioned above, Mascharak reasoned visible light activation of manganese carbonyl complexes is based on two fundamental strategies: increasing the conjugation of aromatic ligand framework, which results in the stabilisation of the LUMO orbital associated with MLCT transitions, and substitution of π-acid ancillary ligands with ligands containing σ-donors or π-basic functionality, leading to an decrease in the HOMO–LUMO gap. Methodical substitution of ligand functionality from weakly electron-donating groups (CH_3) to weakly electron-withdrawing (Br) and strongly electron withdrawing groups (CF_3) resulted in an red shift of absorption maxima between 330–693 nm. TD-DFT calculations and UV/Vis spectroscopy data indicated that presence of an electron-withdrawing group caused a decrease the HOMO–LUMO gap with a subsequent bathochromic shift of the absorption band. In the presence of an electron-donating substitutent, the HUMO–LUMO gap

increases, resulting in an hypsochromic shift of the absorption band.

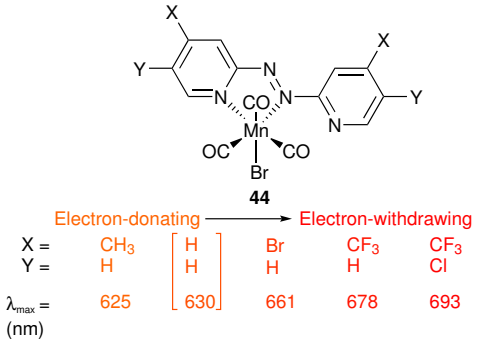

Figure 37: Systematic introduction of electron-donating to electron-withdrawing substituents, and their influence of absorption maxima[102]

1.6.6 Non-Organometallic CORMs

The vast majority of reported CORMs contain a transition metal centre with bound CO ligands. Beside organometallic compounds, there are a handful of non-organometallic compounds that are able to release CO. Included in these is the boroncarboxylate compound, $Na[H_3BCO_2]$ (termed 'CORM-A1'). This water soluble CORM has been shown to release CO at a significantly slow rate under physiological conditions. Its CO release is pH-dependent, with rate of reaction from CORM-A1 gradually increasing as pH decreases from 7.0 to 5.5. Motterlini *et al.* characterised its therapeutic potential by adding the CORM to aortic rings which had been precontracted with phenylephrine. Vasorelaxation was observed 33 minutes after addition. After liberation of the CO equivalent, which originates from the carboxyl group, the compound is rendered inactive (termed '*i*CORM-A1'), and vasorelaxation properties cease. The ability of CORM-1A to induce vasorelaxation was partially inhibited by a sGC inhibitor, and unaffected by an inhibitor of K_{ATP} potassium channels. The vasodilatation elicited by CORM-A1 was markedly increased in the presence of sGC activator YC-1, suggesting a direct cGMP-dependent pathway.[103]

Liao and co-workers developed the visible light activated unsaturated cyclic α-diketone, **45** (Scheme 4).[104] Synthesis of the organic molecule occurs *via* a Diels–Alder reaction.

Illumination with visible light (470 nm) resulted in release of two equivalents of CO. However, in water the ketone functional groups form an equilibrium with the corresponding hydrate. CO release from the α-diketone system involves activation of one carbonyl group by the other. Therefore to prevent hydration of the α-diketone system, Liao encapsulated the anthracene molecule in a hydrophobic micelles (the inner, hydrophobic micelle prevented hydration). The fluorescent nature of the anthracene molecule allowed for the trackable delivery of CO to biological targets. Micelles encapsulated with the organic photoCORM were incubated with leukemia cells. Photochemical activation of the molecule was studied by fluorescence microscopy, which detected a bright blue fluorescence corresponding to anthracene derivatives following CO release.

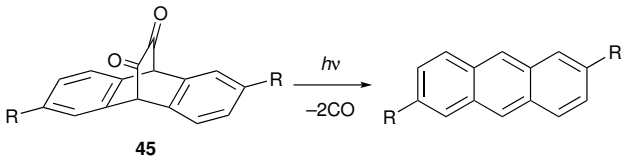

45

R = H, $(OC_2H_4)_2OMe$, OC_8H_{17}

Scheme 4: Visible-light activated unsaturated cyclic α-diketone reported by Liao and co-workers[104]

The strategy of incorporating a chromophore into organic-based photoCORMs has also been utilized by Klán and co-workers, who reported a series of *meso*-carboxy BODIPY (COR-BDP) derived compounds (**46**, Figure 38).[105] Previous studies of the frontier orbitals of various chromophores identified the boron-dipyrromethene (BODIPY) molecule as being suitable for visible light driven CO release.[106] The reported compounds are soluble in aqueous solutions and exhibit no cytotoxicity. The absorption maxima (where R^1 = H and R^2 = Me) lies at 502 nm with complete decomposition of the molecule following illumination at 500 nm. By comparison, the COR-BDP molecule bearing the 3,5-distyryl groups caused a bathochromical shift in the absorption spectrum to 652 nm, which trailed to approximately 750 nm. This red shift is consistent with the addition of further π-conjugation into the chromophore structure. Both compounds released CO in a controllable manner, with liberation of CO ceasing once irradiation was halted.

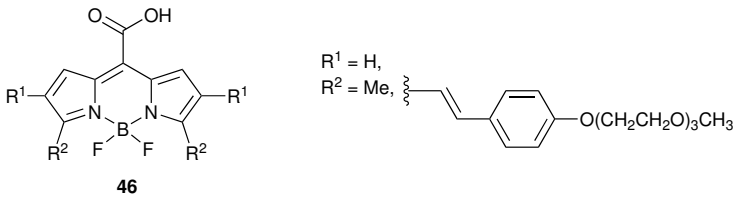

Figure 38: Visible to near-IR activated *meso*-carboxy BODIPY (COR-BDP) derived compounds reported by Klán and co-workers[105]

1.7 Design Principles for the Ideal (Photo)CORM

The development of metal carbonyl complexes to act as CORMs is extremely challenging. Just like any other pharmaceutical drug, CORMs must adhere to a stringent set of requirements. Far removed from the traditional settings of dried organic solvents and oxygen-free conditions, CORMs should exhibit stability and solubility in aerobic aqueous media. Crucially, the ideal CORM would satisfy the appropriate pharmaceutical characteristics (ADME: administration, distribution, metabolism, excretion). The administrated CORM must remain intact in the circulation system and only become active once the targeted tissues have been reached. Liberation of CO must be tightly controlled, with subsequent intermediate breakdown products exhibiting a non-toxic response before being efficiently excreted.

The challenge for synthetic chemists is to incorporate intelligent and rational design principles into the CORM 'drug sphere' in order to generate complexes with the appropriate pharmaceutical properties. Metal-based CORM design can be broken down into three fundamental levels; the transition metal, the coordination sphere and the drug sphere (Figure 39). Although CORMs are not restricted to being transition metal based, for metal-based CORMs the choice of which metal to utilize is critical. The majority of metal carbonyl complexes employ metals from groups 6, 7 and 8 (Cr, Mo, Mn, Re, Fe and Ru) due to their tendency to form stable 18-electron complexes. Metals from groups 3, 4 and 5 (Sc, Ti and V triads) are generally avoided due to their oxygen sensitivity, so too are metal from groups 9 and 10, which are characterised by electronically unsaturated 16-electron complexes. Surveying the literature, the most popular choice of transition metal include manganese, iron and ruthenium. Mn(I) carbonyl complexes are

generally oxidatively stable and are able to incorporate a wide variety of ancillary ligands. However, concerns have been raised regarding manganese flux across the blood-brain barrier causing neurotoxicity.[107] Iron is readily used in organisms, and although excess iron can be damaging, Fe-based CORMs offer a promising platform for the development of CORMs. So too does ruthenium, which has already been incorporated into leading CORMs such as CORM-3.

Careful consideration of the ancillary ligands in the CORM coordination sphere means pharmacological parameters such as water-solubility, biocompatability, biodistrubution and breakdown product profile can be meticulous tuned in the drug sphere. Of course, the coordination sphere must contain at least one M−CO bond. Reactivity of which can be influenced not only by the nature of the metal centre, but also by the ancillary ligands present. The composition of the coordination sphere will represent the fundamental properties exhibited by the CORM, namely responding to trigger mechanisms to release CO, accelerating CO substitution or providing stability following CO release. Coordinating ancillary ligands/biomolecules harbouring desirable functionality at their distal sites allows for the development of a drug sphere which adheres to the appropriate ADME and targeting behaviours.

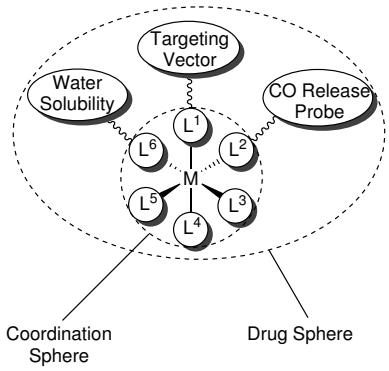

Figure 39: Depiction of CORM drug sphere, where L^1 harbours a targeting vector controlling biodistrubution, L^2 bears a CO-release probe, L^3, L^4 and L^5 represent CO, halide or co-ligand and L^6 imparts water solubility

1.8 Direction of Research

The field of carbon monoxide releasing molecules is still in its infancy. With the enormous variety of transition metal carbonyl complex possible, the field is rapidly expanding with novel CORMs being reported each year. Of particular interest is the development of photoactivated CORMs (photoCORMs) which offer advanced spatial and temporal control over CO release. While the mechanism of light-induced CO release is well established, activation *via* damaging UV irradiation still dominate the literature. Development of visible-to-near IR activated CORMs offer maximal tissue penetration and minimal irradiation damage to tissue.

Taking inspiration from the [Fe]-hydrogenase active site,[108,109] we have identified a family of group 8 carbonyl complexes with the potential to act as photoCORMs. These complexes comprise of a unique 5-membered ferracyclic ring, featuring a low spin Fe(II) metal centre harbouring two *cis*-CO ligands, with a potential third CO functionality 'hidden' in the carbamoyl metallocycle. We recognised that such a CO-rich metal centre comprising a pyridyl chromaphore could provide a platform on which to build accessible photoCORMs activated by visible light. Not only does the pyridyl ligand offer flexible functionality modification, but also the possibility to extend the chromaphore π-system to shift the absorption band of the complex. Substitution of a halide ligand for thiolated saccharide molecules results in the formation of water-soluble dimeric species which are also visible light activated. Analogous ruthenium carbonyl complexes are also reported and the synthesis of florescence derivatized chromophores are investigated. PhotoCORM behaviour is assessed using IR spectroscopy and the myoglobin assay. Beyond chemical synthesis, *in vitro* studies into the anti-inflammatory properties of these novel iron-based complexes have been carried out on THP-1 cells administrated with the endotoxin, lipopolysaccharides (LPS).

Chapter 2

Assessing CORM Activity

2.1 Detection of CO release

The clinical development of leading CORMs require precise quantification of their CO release capabilities. Analytical methods can be employed to fully define the fundamental CO release properties for a given CORM, providing data verifying important parameters including molar equivalents of CO released per mole of active CORM, rate and mechanism of CO release and identification of potential intermediate species. However, monitoring a compounds CO release is not always straightforward as a large number of variables need to be tightly controlled. For instance, factors such as assay solution, temperature and presence of potential activators such as oxygen, light or assay-dependent molecules can all impact CO release behaviour and thereby results in unreliable data. In this section, the analytical techniques used to monitor CO release are discussed.

2.1.1 Infra-Red Spectroscopy

Perhaps the most obvious and easily accessible technique available to follow CO release is infra-red (IR) spectroscopy. Signature vibrational bands for metal-bound carbonyls typically appear in the 1800–2100 cm^{-1} region. The exact position of each band depends on the extent of backbonding exhibited by the metal d orbitals towards each

carbonyl ligand present: increased electron density into the π* orbital of the carbon atom strengthens the M−C bond whilst weakening the carbon-oxygen bond, which corresponds to a lowering of the wavenumber (energy) at which the carbonyl bond vibrates (as seen in the IR spectrum). It is on this basis that ligation influences of other ligands within the drug sphere can be assessed. Monitoring CO release is straightforward: the intensity of the carbonyl vibration decreases following a trigger stimuli. However, this method is limited to behaviour exhibited in pure organic solvents or deuterium oxide (D_2O), as transmittance in aqueous solution is poor.

IR spectroscopy is a powerful tool when it comes to identifying intermediate (*i*CORM) species. New vibrational bands which appear at a similar rate to the disappearance of the carbonyl band(s) is indicative of the formation of an intermediate species. A particularly helpful insight is whether or not the ligand architecture of the active CORM detaches from the metal centre following CO liberation. This is of fundamental importance as the freed ligand could have profound biological implications *in vitro* and *in vivo*. It should also be noted that gaseous by-products dissolved in solution can be detected and quantified.

One advantage of monitoring CO release *via* IR spectroscopy is the procedure requires no technique-dependent species which would influence CORM activity. Indeed, the CO release capability of the diiron complex reported by Liu and co-workers could not be analysed by the traditional myoglobin assay (section 2.1.3) as the reducing agent present influenced CO liberation.[69] Therefore a combination strategy was employed, where IR monitoring of the solution every 10 minutes was correlated with the spectral decay observed *via* UV/Vis spectroscopy. IR monitoring can also be employed for substances requiring light activation. Depending on the time scale of the reaction, activity can be monitored on an interval time frame using solution aliquots. Alternatively, an IR probe can be incorporated into the set-up design, and time-resolved CO loss can be measured *in situ* by directly irradiating the solution cell.

Furthermore, IR spectroscopy is not limited to solution-based analysis. Gas phase IR spectroscopy takes measurements from the head-space above the solution where the intensity of gaseous CO can be recorded. To quantify the amount of CO in the

head-space, a calibration curve is obtained using known CO quantities.

2.1.2 UV/Vis Spectroscopy

UV/Vis spectroscopy provides an insight to the types of electronic transitions taking place. This is particularly helpful for the practical application of photoCORMs, as it allows for the refinement of the irradiation wavelength used to trigger CO release. Furthermore, liberation of CO is often accompanied by distinct spectral changes as an intermediate (*i*CORM) species forms. Combining this detection method with IR spectroscopy could provide mechanistic information such as whether the ligand architecture has altered, or detached from the transition metal centre. Moreover, addition of a CORM to an aqueous, aerobic environment could fundamentally alter its CO release profile. This was the case for the diketone photoCORM developed by Liao and co-workers, where the active species underwent a hydration reaction in the presence of water.[104] UV/Vis spectroscopy revealed this hydrated species did not possess the absorption transition responsible for visible light triggered CO liberation. UV/Vis spectroscopy is also a useful means to investigated CO loss from an aerobic aqueous solution. Ford and co-workers reported a trianionic tunsten photoCORM capable of releasing CO in aerated media.[78] The photo-induced liberation of CO was characterised by an increase in the absorption spectrum at 410 nm. Interestingly, the complex underwent a 'back reaction' (in a CO atmosphere) in which the observed spectral changes reversed, yielding a final spectrum similar to that of the initial photoCORM.

2.1.3 Myoglobin Assay

The most widely used detection method of CO release is the myoglobin (Mb) assay. This method relies on UV/Vis-spectroscopic changes as the newly liberated CO converts dexoymyoglobin (deoxy-Mb) to carboxymyoglobin (MbCO). The UV/Vis spectroscopy profile of deoxy-Mb is an intense, single-hump band at 557 nm, which shifts to the double-hump profile of MbCO, with peaks at 540 nm and 577 nm (Figure 40). The

assay is conducted in a phosphate buffer saline (PBS) solution at physiological pH 7.4 and a temperature of 37 °C.

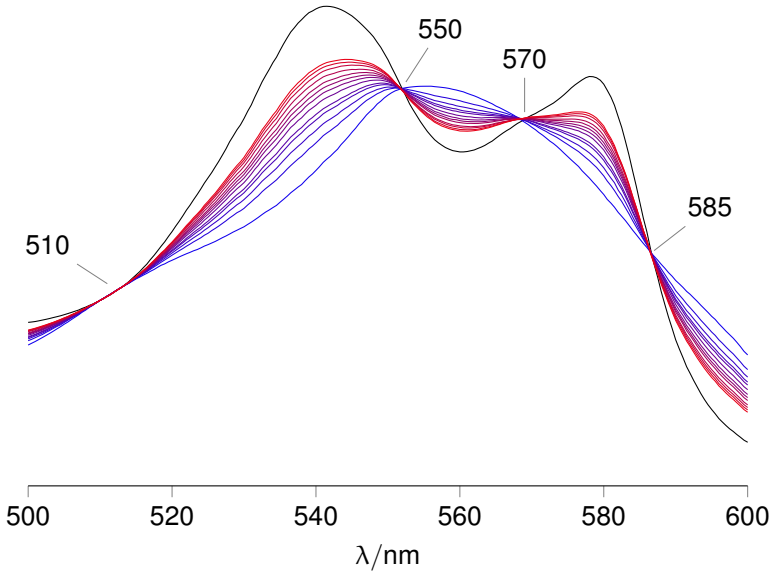

Figure 40: An example spectra of the conversion of deoxy-Mb (blue) to MbCO (red) elicited *via* CORM activity ($MbCO_{max}$ in black, isosbestic points labelled)

For this experiment to be valid, the amount of deoxy-Mb present in the assay must exceed the potential CO release capabilities of the CORM in order to prevent premature saturation of the deoxy-Mb solution. Once the spectral changes have plateaued, the amount of CO released can be determined. The solution is then saturated with gaseous CO to give the total MbCO ($MbCO_{max}$) reading.

Although the myoglobin assay represents the principle method for reporting CORM behaviour, the assay suffers from a number of issues.[82] Firstly, the myoglobin solution is only stable for a short period of time, so fresh solutions must be prepared prior to each experiment. Furthermore, the assay must be completed under an inert atmosphere to prevent the formation of oxymyoglobin. This limitation is particularly pronounced for CORMs which require oxidation to fully complete CO liberation, as is the case of the ET-CORMs reported by Schmalz and co-workers.[65,66] In fact, the assay requires an excess of reducing agent, sodium dithionite, to convert the myoglobin to the CO-scavenging deoxy-Mb. The CO release capability of the diiron CORM developed by Liu

and co-workers was shown to be influenced by this reducing agent, therefore a reliable profile of CO release could not be obtained *via* the Mb assay.[69] More recently, evidence has immersed to suggest CO release from CORM-2 and CORM-3 (**5** and **6**, respectively, Figure 8) is modulated in the presence of sodium dithionite.[110] In fact, no liberation of CO was detected from either complex using CO electrodes (Section 2.1.6), presumably due to the lack of sodium dithionite.[42]

Additionally, the source of reducing agent is important, as commercially available dithionite is often not pure enough for such experiments. Turbidity, which is especially likely in CORMs incorporating macromolecules, can effect the accuracy of the data collected. Another factor to consider is the UV/Vis absorption profile of the CORM itself. This is particularly relevant for highly coloured metal complexes (often photoCORMs) which exhibit absorbance bands which overlap with the absorption bands of the myoglobin. Species with strong bands in the 500–600 nm region are likely to affect the spectra. However, one can get around this issue by using internal reference points known as isosbestic points. Isosbestic points are points in a spectra where two interconverting species (deoxyMb $\longrightarrow$ MbCO) overlap. They act as an internal references because the points are constant and unchanging throughout the conversion. Therefore any deviation from the isobestic points can be corrected for. The myoglobin assay contains four isobestic points at 510, 550, 570 and 585 nm. Typically data treatments ensure the spectra intersect at isosbestic point 510 nm, which could possibly lead to non-aligned spectra at the remaining isosbestic points.

The amount of MbCO formed *via* CORM activity is based on the assumption that 0 % MbCO is present in the deoxyMb spectra. Therefore the absorption reading at 540 nm at this point represents 0 µM MbCO. Before calculating the amount of MbCO formed during the assay, the total amount of MbCO formed following gaseous CO saturation ($MbCO_{max}$) is calculated (Equation 1, $\epsilon_{540} = 15.4\,mM^{-1}\,cm^{-1}$).

$$MbCO_{max} = \left(\frac{OD_{540}}{\epsilon_{540}}\right) \times 1000 \tag{1}$$

Using the $MbCO_{max}$ value, a new extinction coefficient (ϵ_2) value can be calculated

(Equation 2) in order to account for the growing absorbance at 540 nm (ΔOD_{540}). For this calculation, the isobestic point at 510 nm is traditional employed ($OD_{ISO\text{-}510}$).

$$\epsilon_2 = \left(\frac{\Delta OD_{540} - \Delta OD_{ISO\text{-}510} \times 1000}{MbCO_{max}} \right) \quad (2)$$

Using the newly calculated ϵ_2, the concentration of MbCO converted from deoxyMb *via* CORM CO release can be determined (Equation 3).

$$MbCO = \left(\frac{\Delta OD_{540} - \Delta OD_{ISO\text{-}510}}{\epsilon_2} \right) \times 1000 \quad (3)$$

The myoglobin assays allows a rate of MbCO formation to be determined, which offers a means to quantify the rate of CO released from the active CORM species. However, one must be careful when deriving kinetic parameters by this method. The majority of reported CORMs possess more than one labile CO ligand. This adds a degree of complexity to calculating rate constants: each intermediate will have its own kinetic profile, which would ideally be determined independently.[82]

2.1.4 Gas Chromatography

Gas chromatography represents a method of quantifying the amount of gaseous substances in a head-space of a particular volume. This strategy can be applied to monitor the amount of CO released from a CORM. This detection method is independent of solvent used, presenting an opportunity to monitor CO release from an aerobic aqueous environment (due to the poor solubility of CO in water). Of course, solution factors such as pH and presence of biological species (*e.g.* amino acids in media) could influence CO release.

2.1.5 Florescent Probe

Detection of small signalling molecules including NO and H_2S has been achieved *via* the use of florescent probes.[111,112] Chang *et al.* developed a florescent probe featuring a

borondipyrromethene difluoride (BODIPY) core for the detection of CO.[113] This first generation carbon monoxide probe (COP-1, Figure 41) comprises a palladium(0) motif, which quenches the compounds fluorescences. In a highly selective reaction involving only CO (other biologically relevant signalling molecules such as NO and H_2S eliciting no reaction), COP-1 exhibits a 'turn on' fluorescence at 503 nm following coordination of CO with liberation of palladium(0).[114] *In vitro* studies have shown that cells incubated with COP-1 displayed increased fluorescence following CORM administration compared to cells without. Furthermore, cell viability studies revealed the compound elicits no cytotoxicity issues.

As the fluorescence of COP-1 is triggered specifically by CO, it offers a unique platform to monitor the cellular uptake and biodistribution of a given CORM. Schatzschneider and co-workers successfully employed COP-1 to access the CO release capability of an $Mn(CO)_3$-based photoCORM.[115] Incubation of the photoCORM with COP-1 in the dark resulted in only very weak fluorescence, whilst strong fluorescence was observed following irradiation at 365 nm. However, the florescence of the supernatant fraction appeared to be much stronger than the fluorescence of the cell-containing fraction. This demonstrated that the majority of the active CORM remained in the supernatant fraction at the time of irradiation, illustrating the complexes poor cellular uptake behaviour.

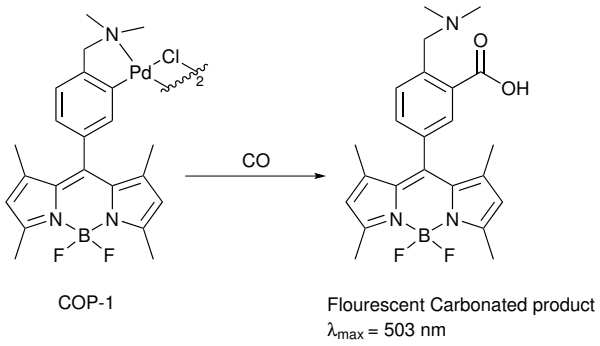

Figure 41: 'Turn-on' fluorescence exhibited by COP-1 upon reaction with CO

2.1.6 Electrodes

Electrodes have been utilized for the detection of signalling molecules, CO and NO. One particular dual electrode system to mention is the two platinum microelectrode system featuring an Ag/AgCl reference electron, all coated with an PTFE gas permeable membrane. One of the platinum microelectrodes (250 µm in diameter) is plated with tin. The second platinum disk is much smaller at 25 µm in diameter. Surface modification as well as size alterations between these two sensing disks results in an apparently separate sensitivity ratios of NO and CO at each microelectrode. Indeed, CO oxidation occurs more favourably at the tin-coated electrode than the platinum electrode. By employing a calibration curves, simultaneous detection of CO and NO from either electrode allow for the concentration of CO and NO to be determined.[114,116]

2.2 PhotoCORM Considerations

2.2.1 Quantum Yield

For a reaction to be classified as being photochemical, it must adhere to two fundamental photochemical laws: the Grotthuss–Draper law states a photochemical reaction can only take place following light absorption,[117] and the Stark–Einstein law states one photon will only activate one molecule for a subsequent reaction.[118] This is known as the 'photoequivalence law'. The quantum yield (Φ) of a reaction is a unitless measurement of the efficiency of a photochemical process. By definition, quantum yield is the number of moles of product produced per mole of monochromatic light absorbed (Equation 4). A photochemical process in which all molecules absorb all photons will have a quantum yield near 1.0. The exception to this is photopolymerization, where the moles of activated monomers divided by the moles of photons absorbed is likely to exceed 1.0. Deactivation of the excited state *via* a non-radiative return pathway (transitions without photon emission), rather than through fluorescence processes will lower the quantum yield measurement.

$$\Phi = \frac{\text{moles of product produced}}{\text{moles of photons absorbed}} \tag{4}$$

Typically, the quantum yield is measured at a specific wavelength of irradiation. Measurements obtained from broadband light sources will be less precise. One disadvantage of quantum yield measurements is that they provide no insight into why a photochemical process is efficient. Furthermore, the quantum yield value of a molecule is dependent on any competing processes occurring. Therefore the fluorescence (and therefore quantum yield value) of a molecule can be limited by these competing processes despite the photochemical reaction efficiency being high.

2.2.2 Release Kinetics

The half-life, $t_{1/2}$, of an drug can be defined as the time it takes for the active species to lose half of its activity. The half-life is a constant and implies an exponential decay with an intrinsic rate can be applied to the photochemical reaction, regardless of conditions. However, this is not the case. There is no intrinsic rate constant (nor half-life) associated with the photoliberation of CO. Moreover, the rate at which a CORM releases CO is directly dependent on the experimental or biological environment in which the rate is being measured, with absorbance of the solution being a critical parameter. The latter will of course depend on the nature and concentration of the species in solution, in particular any daughter products of initial CO release. For example, the kinetics associated with the photochemical dissociation of CO from the photoCORM is likely to be unique for that species, and each photoactive intermediate species would have a separate kinetic profile. Quantum yield is therefore the preferred measure for comparing the photochemical activation of photoCORMs.

2.3 *In Vitro* Activity Studies

Beyond quantifying CO release, the clinical development of CORM systems relies on building a pharmacokinetic profile for the active species by collecting data from a number of *in vitro* and *in vivo* biological studies. To date, the majority of reported CORMs lack the prerequisites required for clinical development: display low toxicity pre- and post CO release, have predictable biodistribution, exhibit a known therapeutic action and adhere

to suitable ADME behaviour (which requires stability and solubility in aerobic aqueous media). A pharmacokinetic profile for a given CORM may include biodistribution studies,[119] cell viability studies,[84,93] cytoprotection assays[83,95] and anti-inflammatory assays.[60]

2.3.1 Cytotoxicity

Traditionally, the primary *in vitro* biological study preformed measures the cytotoxicity profile of the CORM system. This information is essential, as further therapeutic studies would be redundant if the complex displays unsatisfactory toxicity. Furthermore, metal-containing CORMs often form intermediate species following CO release, which could produce toxicity issues.

Cell viability can be studied using a number of assays, the most common of which is the alamar blue assay[120] and the MTS cell proliferation assay.[121] Both represent colourimetric sensitive assays for the quantification of viable (living) cells. The alamar blue assay contains the active ingrediant resazurin (blue, non-fluorescent) which is continuously reduced to resorufin (red, highly fluorescent) in cells. During the MTS cell proliferation assay, viable cells within a cell culture are treated with a MTS tetrazolium compound, which is reduced *via* NADPH-dependent dehydrogenase enzymes present in metabolically active cells. The reduced tetrazolium compound forms a formazan dye, which has an absorbance at 490–500 nm. In both assays, spectrophotometric measurement of the formation of resorufin (in the alamar blue assay) and formazan dye (in the MTS assay) act to quantify the number of viable cells present in each assay.

The above assays both respond to the cellular metabolism of viable cells. The lactate dehydrogenase (LDH) assay[122] differs from these by quantifying the number of dead cells. LDH is a cytosolic enzyme present in viable cells. Following cell death, or compound-induced death of a cell, the soluble LDH is released into the cell culture media. Extracellular LDH catalyses the reduction of NADH to NAD^+. LDH activity can be measured *via* monitoring the absorbance peak for NADH at 340 nm. Alternatively, the assay could contain a tetrazolium salt (similar to the MTS cells proliferation assay) which is reduced by NADH to form the strongly coloured dye, formazan.

2.3.2 Anti-Cancer

Treatment of epithelial cancers, including prostate and breast cancer are limited to chemotherapies from compounds including taxol, doxorubicin and *cis*-platin. Contrary to the cytoprotective actions mentioned in Section 2.3.1, CO has the ability to induce apoptosis in cancer cells.[9,123] Furthermore, administration of CO acts to sensitize cancerous cells to chemotherapy whilst exhibiting a protective influence over normal cells against chemotherapeutic toxicity. Furthermore, exposure to CO whilst undergoing chemotherapy treatment (with either doxorubicin or camptothecin) enhances tumour cell death compared to the effects of chemotherapy alone. Otterbein and co-workers attributed this to a disruption of the metabolic state of the cancer cell *via* targeting the mitrochondria and modulating its activity (noted by an increased production of ROS and oxygen consumption), ultimately leading to mitochondrial collapse. By decreasing the synthetic pathways of nucleotides and amino acids whilst increasing oxidative metabolism, the cancer cell effectively becomes metabolically exhausted. This intense mitochondrial oxidative stress results in the complete breakdown of the cell-cycle and death of the tumour cell.[124] Indeed, selective accumulation of CORMs to tumour cells with targeted CO release offers a promising and novel anti-cancer treatment. This is especially appealing for cancers which display resistance to traditional chemotherapy treatment, and could also act to prevent the migration of cancer cells to other organs.

Exogenously supplied CO (either in the form of gaseous CO or *via* CORM-2) has been shown to inhibit pancreatic cancers *via* the suppression of the intracellular signalling pathways including phosphatidylinositol-3 kinase (PI3K)/Akt, the downstream pathway of which has been shown to contribute to cancer neovascularisation.[125] Indeed, human pancreatic cancer cell lines administrated with CORM-2 displayed inhibition of the akt phosphorylation signalling pathway. To attribute this outcome to CO, proliferation of pancreatic cancer cells exposed to CO-enriched synthetic air (500 ppm, 24 h) was shown to be significantly reduced compared to cells exposed to air. Mice carrying human pancreatic xenografts administrated with CORM-2 or gaseous CO (500 ppm, 24 h) exhibited reduced tumour volumes, limited tumour neovascularisation and significantly

enhanced survival rate compared to models administrated with the inactive, *i*CORM-2 control.[126] The observed anti-cancer properties of CO seem to oppose the effects elicited by NO. Indeed, inducible expression of nitric oxide synthase has been correlated with microvessel density in human gastric cancer.[127]

2.3.3 Anti-inflammatory

One of the fundamental therapeutic actions of CO is the inhibition of pro-inflammatory cytokines and the up-regulation of anti-inflammatory cytokines.[5,28,30] Inflammation can be readily induced following administration of endotoxin, lipopolysaccharides (LPS). Hubbell and co-workers evaluated the anti-inflammatory activity of the micelle-protected CORM-3 by monitoring the LPS-induced production of the pro-inflammatory transcription factor, NF-κB.[60] This was achieved *via* addition of LPS to a cell line transfected with a reporter plasmid expressing a secreted embryonic alkaline phosphatase (SEAP) gene. Expression of this gene is influenced by a promotor which responds to NF-κB. NF-κB activation can therefore be correlated with the amount of secreted SEAP. Indeed, addition of LPS caused the secretion of SEAP *via* NF-κB activation, which was suppressed in the presence of the active CORM species.

Alternatively, inflammation can be monitored *via* the Enzyme Linked Immuno Sorbent Assay (ELISA, Figure 42). Administration of LPS to macrophages promotes the production of pro-inflammatory cytokine, TNF-α. The ELISA assay allowed the concentration of TNF-α to be determined spectrophotometrically: The cell supernatants (which contains the TNF-α) are added to wells coated with a TNF-α antibody, known as the 'capture antibody', followed by the addition of an TNF-α antigen, which binds to the immobilized antibody. Next, a biotinylated monoclonal antibody is added and binds to the immobilized antibody. Addition of the enzyme, streptavidin-peroxidase binds to the biotinylated antibody, which acts on a substrate solution to produce a coloured product. The absorbance intensity is directly proportional to the concentration of TNF-α, determined by plotting against a standard curve of known cytokine concentration. In this thesis, the anti-inflammatory effects of the developed photoCORMs systems are analysed *via* the ELISA assay.

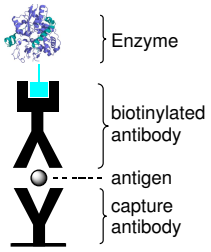

Figure 42: Representation of the 4-membered sandwich used in the ELISA assay

2.4 Summary

The development of CORMs from the Schlenk line to clinical applications requires an analytical insight from a range of physical techniques. To ascertain the fundamental CO release characteristics of a novel CORM, spectroscopic analysis (predominantly IR spectroscopy) can be readily employed to yield a qualitative release profile. Once CORM activity and trigger mechanism has been established, a quantitative evaluation can be obtained *via* the myoglobin assay. The myoglobin assay represents the principle analytical method for quantifying CO release. Although the assay exhibits a number of pitifuls, the method remains relatively easy to reform, does not require uncommon spectroscopic equipment, and results in the quantifiable description of a CORM CO release capability. Progress in the field is becoming ever more dependent on the development of reliable methods to study CORM behaviour *in vitro* and *in vivo*. The progress of *in vitro* testing has been promising, with techniques assessing CORM toxicity and gauging therapeutic activity in a measurable and compatible manner. In this thesis, the quantitative assessment of photoCORM activity is achieved using the myoglobin assay to verify CO release, in combination with the ELISA assay to authenticate anti-inflammatory properties in a rounded evaluation of the developed systems.

Chapter 3

Group 8 Metallocyclic PhotoCORMs

3.1 Introduction

To date, the development of photoCORMs has predominantly focused on neutral and cationic manganese(I) systems. In particular, the Mascharak group have reported a number of visible light activated photoCORMs.[98–101] These comprise of $Mn(CO)_3$-cores functionalised with bidentate ligands bearing nitrogen donors and an extended π systems (Section 1.6.5).

In his exploration of developing photoCORMs, Mascharak proposed certain design principles to achieve photolabilisation of CO from low energy irradiation. This included ligand architectures incorporating a heteroatomic extended conjugation system featuring low-lying orbitals.[89,100] The extended π-system acts to shift the absorption maxima of the complex in a bathochromic fashion. Ligands fostering low lying empty π* orbitals promote MLCT transitions, which are thought to be a predominate step in the photodissociation of CO. Furthermore, Zobi and co-workers established substitution of electron withdrawing groups onto the ligand framework decreases the HOMO–LUMO gap, thereby facilitating MLCT transitions at lower energies.[102]

The development of photoCORMs based on manganese is perhaps not surprising as one of the first complexes observed to release CO *via* photolysis was $Mn_2(CO)_{10}$ (**4**, Figure 8). Indeed, the biological studies performed by Motterlini *et al.* advocated a promising

platform from which the field of Mn-based photoCORMs could advance.[7] However, despite being one of the most utilized transition metals, worries over manganese derived neurotoxicity persist.[107]

It is reasonable to propose that CORMs featuring transition metals which occur naturally in biology possess an edge over those that do not. For instance, iron is essential in the biology for the majority of life on earth. In the human body iron governs the uptake of oxygen in red blood cells as part of the haemoglobin molecule. Not only this, iron is implicated in an array of highly complex processes such as the production of metalloproteins, development of the immune system and is essential for the cognitive development of children. Furthermore, the body has evolved sophisticated mechanisms to excrete iron and maintain a non-toxic, homoeostatic quantity. In the event the levels of iron in the body fall below the homoeostatic threshold, the body recovers by reducing the production of haemoglobin. However, it should be stated that an excess of iron can be dangerous. For example, ROS are readily generated *via* Fenton chemistry.[128]

The venture of iron-based CORMs began with the photoactivation of $Fe(CO)_5$ (**3**, Figure 8) reported by Motterlini *et al.*[7] However, this simple carbonyl exhibited poor water solubility and high toxicity. Westerhausen and co-workers reported a water soluble iron-based photoCORM harbouring two cysteamine ligands (**29**, Figure 28). The complex released CO following irradiation of visible light (470 nm).[91] Unfortunately, further chemical enhancements to the complex were limited due to the fact the drugs sphere bears no organic chromophore to modify. Kodanko and co-workers reported the water soluble dicationic photoCORM **21** (Figure 20).[83] Photo-dissociation of CO was achieved *via* irradiation with UV light (365 nm). However, the complex displayed worrying cytotoxicity (at 10 µM) following CO release due to the ability of $Fe(N_4Py)^{2+}$ to inhibit cellular growth. The photoCORM was further modified *via* the incorporation of a short peptide. This could govern the complex tissue delivery, and offers a potential opportunity to induce cellular death through a combination of CO and $Fe(N_4Py)^{2+}$ release. This type of selectivity and toxicity would be desirable for cancer treatments. Moving away from photo-induced CO release, Liu and co-workers reported the diiron hexacarbonyl complex, **12** (Figure 14) which released CO following substitution with cysteamine.[69] Unlike $Fe(CO)_5$, the diiron complex bears two thioglycol ligands fostering

four hydroxyl groups which renders the complex completely water soluble. Co-drug assisted release of CO resulted in the formation of a monoiron species which was shown to release further quantities of CO *via* oxidation.

Biocompatability issues could also be minimised by designing CORMs based on naturally occurring complexes. The [Fe]-hydrogenase enzyme harbours an active site which consists of two *cis* carbonyl groups and a chelating pyridine-acyl ligand architecture. The natural system is thought to coordinate to a protein-bound sulfur, whilst the identify of the sixth ligand remains unclear, although it is thought to be solvent (**47**, Figure 43).[129] Isolation of the active site was only possible in conditions of low light, which point to a potentially exploitable platform for photoCORM development. Previous work in our group reproduced a synthetic model of this active site ($\mathbf{Y1_{Fe}}$, Figure 43).[108,109] This synthetic analogue features a low spin Fe(II) metal centre, bears *cis* carbonyl groups and surrogates a pyridine-carbamoyl ring instead of an pyridine-acyl ring. Furthermore, the complex incorporates an bromide ligand (instead of a sulfur) *trans* to one of the CO ligands. This is advantageous: Mascharak demonstrated complexes fostering halide ligands displayed a red shift in absorption compared to complexes bearing other ligands.[98] Moreover, the bromide provides a platform to further modify the complex *via* substitution reactions involving thiolates. The sixth ligand comprises a labile solvent molecule, which can be reversibly replaced by CO under a CO atmosphere.

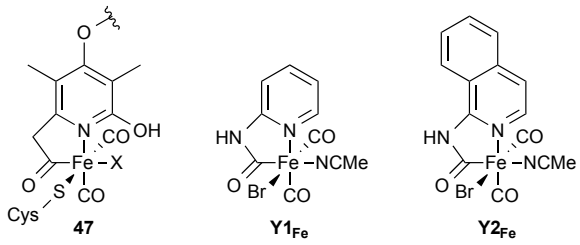

Figure 43: **47**: Fe-hydrogenase enzyme active site (X = solvent, Cys = Cysteine). $\mathbf{Y1_{Fe}}$: Synthetic analogue. $\mathbf{Y2_{Fe}}$: Modified photoCORM

This iron-based complex adopts all the prerequisite design principles for photoCORM development: the pyridyl ligand provides a chromophore for light absorption which

could be extended or chemically modified. The coordination sphere contains a total of three potentially labile CO equivalents: two metal-bound CO ligands and a third CO functionality 'hidden' in the 5-membered ferracyclic ring. This chapter discusses the synthesis, structure and photoCORM behaviour of $\mathbf{Y1_{Fe}}$. Building on this, we increased the conjugation of the ligand architecture to yield $\mathbf{Y2_{Fe}}$ and probe the influence on CO release. In addition, the chemistry of ruthenium analogues complexes is discussed, including a comparison between the choice of metals (Fe *vs* Ru) and its impact of visible light-induced CO labilisation.

3.2 Synthesis of Ferracyclic Complexes

The initial synthesis of $\mathbf{Y1_{Fe}}$ was reported by Turrell *et al.* in 2010.[108] Insight into the formation of this carbonyl complex revealed the intermediate salt comprised a cationic protonated 2-aminopyridine fraction and a ferracyclic dibromo anion fraction ($\mathbf{X1_{Fe}}$).[109] Therefore we adapted the literature procedure by adding two equivalents of 2-aminopyridine (Scheme 5). This not only improved the reliability of the reaction, but also drove the equilibrium towards the formation of the precipitate product, which resulted in a slightly improved yield of $\mathbf{Y1_{Fe}}$ (51 % *vs* 46 %). This chemistry was extended *via* the reaction of $Fe(CO)_4Br_2$ with 1-aminoisoquinoline at −40 °C to yield $\mathbf{X2_{Fe}}$ and $\mathbf{Y2_{Fe}}$.

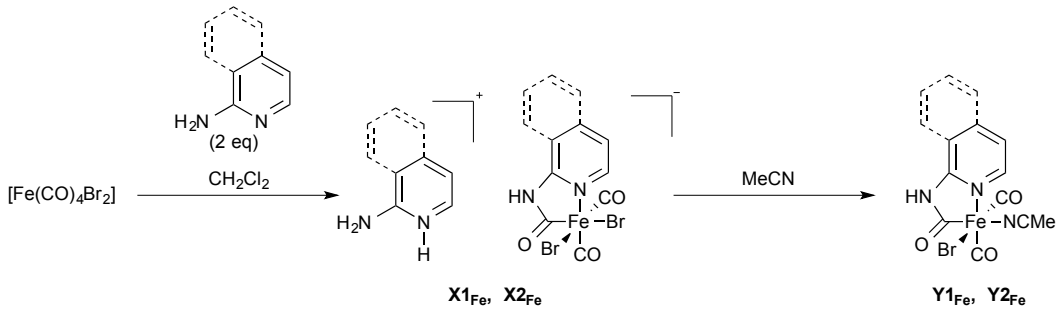

Scheme 5: Synthesis of charged intermediate species and neutral ferracyclic photoCORMs

The formation of $\mathbf{Y1_{Fe}}$ and $\mathbf{Y2_{Fe}}$ can be monitored *via* IR spectroscopy. The IR

spectra for $\mathbf{Y1_{Fe}}$ consists of three bands for a *cis* dicarbonyl at 2047 cm^{-1} and closely positioned signals at 1995 and 1982 cm^{-1}. The three carbonyl bands suggests the presence of multiple geometric isomers in solution. Attenuated total reflection (ATR) IR is consistent with a *cis* dicarbonyl geometry (1984 and 2046 cm^{-1}). Formation of the five-membered carbomoyl ring is observed with peaks at 1666 and 1621 cm^{-1}. The solvent molecule is only weakly coordinating, and is reversibly replaced with CO whilst under a CO atmosphere.[108]

X-ray crystallography confirms the presence of the carbamoyl functionality, with the two carbonyl ligands retaining a *cis* geometry: one carbonyl being *trans* to the chromophore nitrogen and the other located *trans* to the bromide ligand. The carbamoyl CO bond length (1.227(5) Å in $\mathbf{Y2_{Fe}}$ · MeCN) is significantly longer than the carbonyl ligands (1.127(2) Å and 1.130(5) Å in $\mathbf{Y2_{Fe}}$ · MeCN), suggesting the carbamoyl CO bond is predominately double bond in character whereas the two carbonyls are of triple bond character.

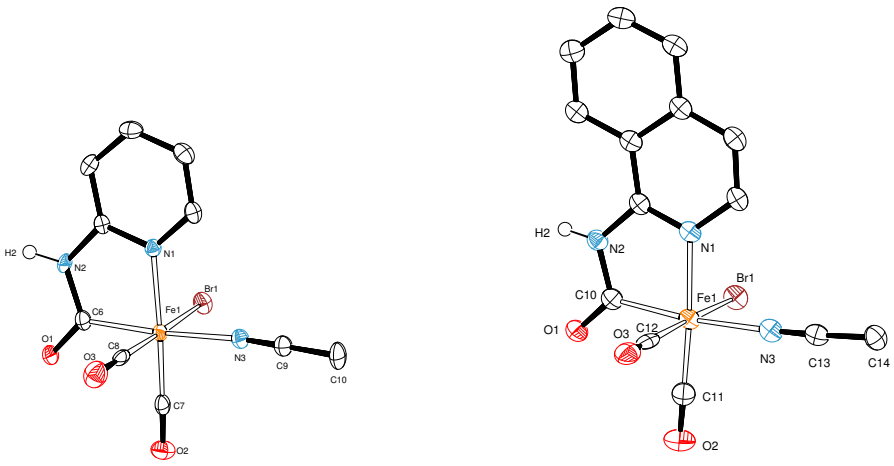

Figure 44: ORTEP representation of $\mathbf{Y1_{Fe}}$ · MeCN (left) and $\mathbf{Y2_{Fe}}$ · MeCN (right) showing 50 % ellipsoids; non-coordinated MeCN and hydrogen atoms except for H(2) have been omitted for clarity

In DMSO, $\mathbf{Y1_{Fe}}$ exhibits a broad MLCT absorption band centred at 260 nm with a pronounced tail trailing into the visible region near 500 nm, giving the complex a yellow appearance. Comparison of the λ_{max} value of $\mathbf{Y2_{Fe}}$ reveals a similar profile with a significant additional absorbance band at 335 nm due to the additional conjugation

system of the aminopyradyl framework (Figure 45). The extinction coefficient of these two complexes in the visible region report at 1500–2000 $\mathrm{M}^{-1}\,\mathrm{cm}^{-1}$.

A comparison of the electronic absorbance profiles for the neutral complexes and charged intermediate species are also shown in Figure 45. The structures of the charged $\mathbf{X1_{Fe}}$ and $\mathbf{X2_{Fe}}$ species are shown in Scheme 5. In both cases, the iron centre has an octahedral geometry with *cis* carbonyl ligands. The sixth ligand consists of a bromide ligand, which is replaced by solvent to give the corresponding neutral complex. The electronic absorption spectra of the charged species displays a hypsochromic shift with a less-predominant tail in the visible region compared to the neutral species.

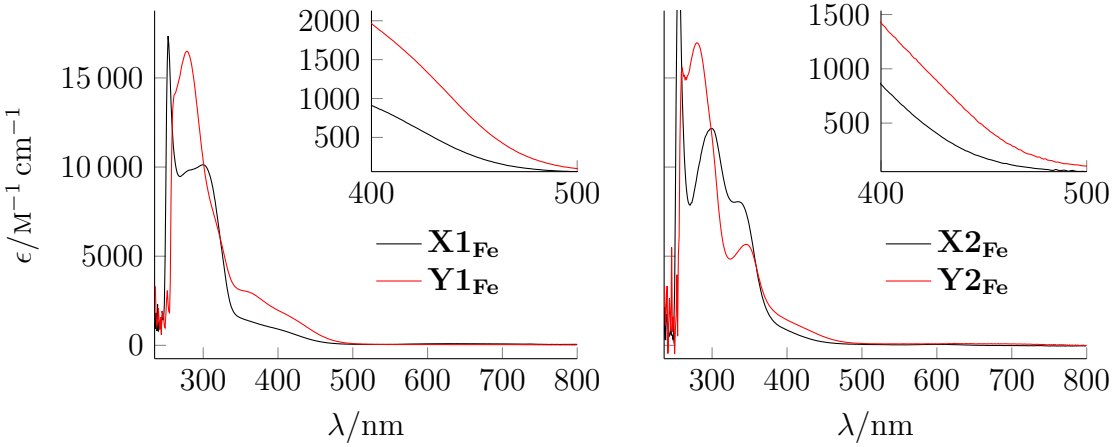

Figure 45: Comparison of the electronic absorption spectra of $\mathbf{Y1_{Fe}}$ with $\mathbf{X1_{Fe}}$ (left) and $\mathbf{Y2_{Fe}}$ with $\mathbf{X2_{Fe}}$ (Right) in DMSO

A number of important parameters must be considered when designing the ligand architecture. First, despite the red shift influence on absorptivity elicited *via* an extended conjugation system, the subsequent increase in hydrophobicity of the complex results in aqueous solubility issues. Second, to ensure adequate cellular uptake, the developed CORM should not exceed a molecular size of 500–600 $\mathrm{g\,mol}^{-1}$. These two factors ultimately limit the size of the conjugation systems.

An alternative strategy is the addition of heteroatoms onto the conjugation system to further modulate absorption. To this effect we employed 2-aminopyrimidine, which harbours a N-donor atom within the ring system. Unfortunately, only the intermediate salt product ($\mathbf{X3_{Fe}}$, Figure 46) was isolable, with IR evidence of the neutral species

in solution (2055, 2004, 1992, 1981, 1668 and 1617 cm^{-1}). Similarly, we incorporated an additional amine functional group ($-NH_2$) onto the ligand architecture in order to examine any shifts in the absorption spectrum. Addition of 2,6-diaminopyridine to $Fe(CO)_4Br_2$ resulted in the precipitation of a yellow solid ($\mathbf{X4_{Fe}}$, Figure 46). Dissolution in acetonitrile yielded an IR profile with the expected characteristic peaks (2056, 2000, 1655 and 1640 cm^{-1}). However, characterisation of the neutral species beyond IR was not unsuccessful.

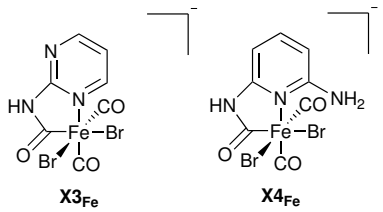

Figure 46: Structure of intermediate anionic complexes, $\mathbf{X3_{Fe}}$ and $\mathbf{X4_{Fe}}$

Figure 47 shows the profound difference in the absorption spectra for $\mathbf{X3_{Fe}}$ and $\mathbf{X4_{Fe}}$ in DMSO. Addition of an amine functional group onto the ligand framework results in a substantial red shift of the MLCT band compared to ligand systems which incorporate an N-donor atom into the conjugation system. Anionic product $\mathbf{X4_{Fe}}$ exhibits strong MLCT bands at 259 nm and 340 nm, the latter of which trails into the visible region. Compare this to $\mathbf{X3_{Fe}}$, which displays absorptivity only in the UV-region (299 nm). A non-negligible absorbance is observed trailing into the visible, although the molar extinction coefficient value in this region is minimal.

Interrogation of the UV/Vis spectra for the intermediate salt substituents reveal a hypsochromic shift of the MLCT band compared to that of the neutral complexes. Furthermore, the intermediate species may participate in stronger backbonding to the CO ligands, perhaps as a consequence of the anionic charge. For these reasons, we decided to focus our efforts on the development of the neutral complexes as photoCORMs.

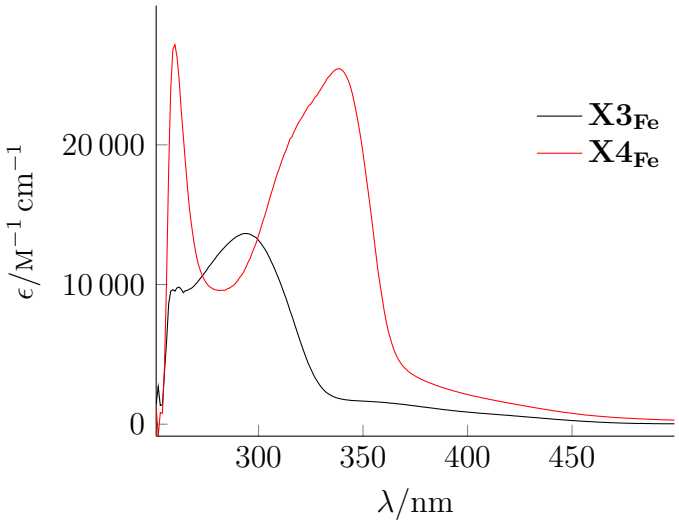

Figure 47: Electronic absorption spectra of $\mathbf{X3_{Fe}}$ (black) and $\mathbf{X4_{Fe}}$ (red)

3.3 Quantification of CO Release Behaviour

3.3.1 IR Spectroscopy

The primary method employed to establish photo-induced release of CO from $\mathbf{Y1_{Fe}}$ was IR spectroscopy. A solution of $\mathbf{Y1_{Fe}}$ shielded from light is stable for extended periods of time. Complex $\mathbf{Y1_{Fe}}$ exhibits three strong bands for a *cis* dicarbonyl at 2047 cm^{-1} and close signals at 1995 and 1982 cm^{-1}, which is indicative of two isomers present in solution. The carbomoyl stretch is seen at 1666 and 1621 cm^{-1}. Photo-induced CO release was achieved using a KL5125 fibre optic light source, which included a light intensity/brightness control ('low power' 0.216 W and 'high power' 0.840 W). This lamp produces a broadband of visible light. Steady progress of the photolysis of CO is shown in Figure 48. A subtle shift is observed as the peak at 2047 cm^{-1} decreases to a new wavenumber at 2042 cm^{-1}. Notably, the two distinct peaks at 1995 and 1982 cm^{-1} merge into a single, averaged peak at 1989 cm^{-1} following CO release. This suggests the presence of only one isomer in solution after initial CO loss. Figure 48 displays the decrease in intensity of the carbonyl peak at 2047 cm^{-1} *vs* time.

With regards to $\mathbf{Y2_{Fe}}$, prior to illumination the IR spectra consisted of a distinct carbonyl band at 2053 cm^{-1} with two carbonyl signals at 1999 and 1989 cm^{-1}. The carbamoyl bands are observed at 1662 and 1613 cm^{-1}. Notably, the carbonyl vibrations

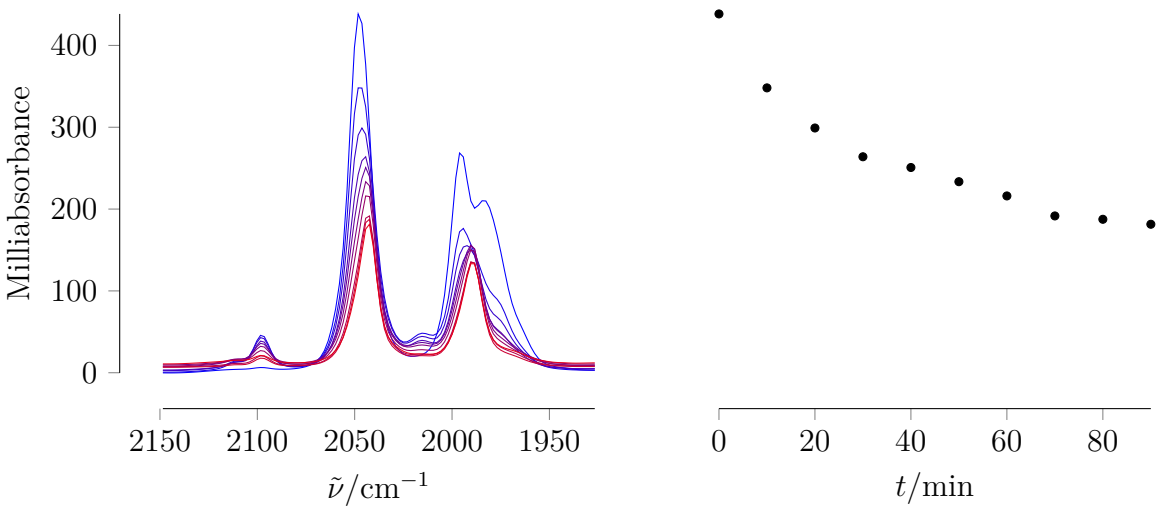

Figure 48: Left: Infrared Spectra of $\mathbf{Y1_{Fe}}$ during visible light ('high power') triggered CO release in THF. Data ranges from 0 min (blue, prior to illumination) to 90 min (red), measured at intervals of 10 min. Right: Carbonyl intensity at 2047 cm^{-1} decrease over time of illumination

of $\mathbf{Y2_{Fe}}$ are found at a higher wavenumber than the corresponding peaks of $\mathbf{Y1_{Fe}}$. Replacement of pyridine for isoquinoline (with more conjugation in the ligand frame) leads to reduced backbonding to the carbonyl ligands, which consequently weakens the M−CO bond and increases the labilisation of CO. Figure 49 shows CO release triggered *via* visible light. Again, loss of CO is characterised with subtle shifts of the vibrational bands.

Initial CO loss from $\mathbf{Y1_{Fe}}$ and $\mathbf{Y2_{Fe}}$ is accompanied with the appearance of a new signals at 2098 and 2017 cm^{-1}, which indicates the formation of a potential intermediate species. The most obvious explanation is the coordination of a solvent ligand following the sequential release of CO. However, this intermediate species is short lived, with the signal intensity rapidly decreasing with subsequent CO release. Furthermore, precipitation of an insoluble '*i*CORM' product slowly appeared over the course of the experiment. Attempts to characterise this by mass spectrometry did not yield identifiable molecular ions.

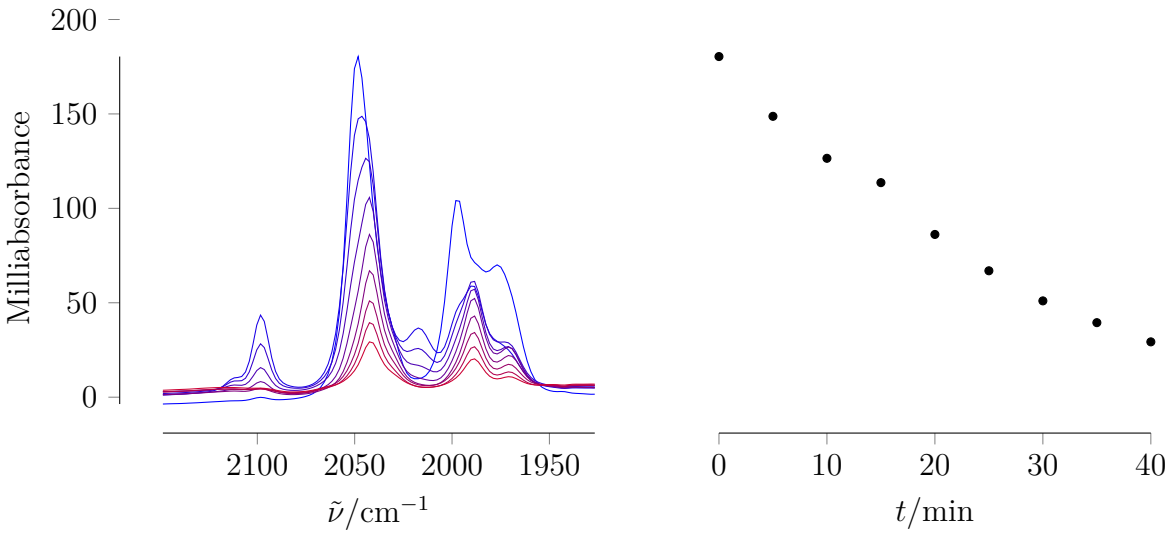

Figure 49: Left: Infrared Spectra of $\mathbf{Y2_{Fe}}$ during visible light ('high power') triggered CO release in THF. Data ranges from 0 min (blue, prior to illumination) to 40 min (red), measured at intervals of 10 min. Right: Carbonyl intensity at 2049 cm^{-1} decrease over time of illumination

3.3.2 Myoglobin Assay

Light-induced CO release from $\mathbf{Y1_{Fe}}$ and $\mathbf{Y2_{Fe}}$ has been investigated using the myoglobin assay (Section 2.1.3). The assays were completed following irradiation with a broadband visible light source. More specifically, the photoCORMs were irradiated at 'low power' (0.216 W) and 'high power' (0.840 W) visible light. Neither complex released CO when kept in the dark in the presence of Mb and sodium dithionite. Despite the extended conjugation system of $\mathbf{Y2_{Fe}}$, the CO release properties of each complex is markedly similar under the same light conditions (50).

The CO release rates and quantum yield (Section 2.2.1) measurements are summarised in Table 1. Figure 50 shows the formation of MbCO *via* photoCORM activity. Both complexes yielded reproducible results which were verified at three different concentrations (10, 20 and 30 µM) in independent experiments. The CO release capabilities of each complexes is dependant on the intensity of light used. Irradiation of 'low power' visible light (dashed lines) were markedly similar for both complexes which correlates with the near identical quantum yield values obtained. The CO release properties following illumination with 'high power' visible light (solid lines) establish

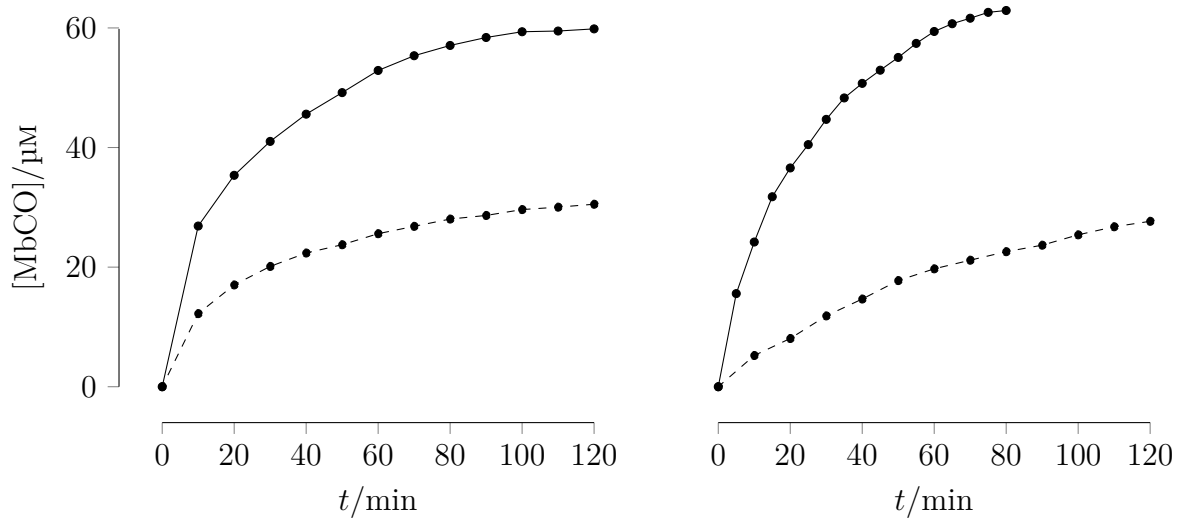

Figure 50: Plot of the amount of MbCO formed *via* CO liberated from $\mathbf{Y1_{Fe}}$ (30 μM, left) and $\mathbf{Y2_{Fe}}$ (30 μM, right) (Dashed: 'low power' (0.216 W) irradiation, Solid: 'high power' (0.840 W) irradiation)

the fundamental preference for employing ligand architectures harbouring larger conjugation systems. For instance, two equivalents of CO are liberated from $\mathbf{Y2_{Fe}}$ after 80 minutes of illumination, whereas the same equivalents are release from $\mathbf{Y1_{Fe}}$ after 120 minutes. Indeed, the apparent rate of CO release is significantly greater in $\mathbf{Y2_{Fe}}$. This is reflected in the quantum yield measurements, where the light absorbed by $\mathbf{Y2_{Fe}}$ following intensity irradiation exceeded that of $\mathbf{Y1_{Fe}}$.

Table 1: Table showing rates of CO release and quantum yield for $\mathbf{Y1_{Fe}}$ and $\mathbf{Y2_{Fe}}$

Complex	Average Apparent Rate (μM/ min)		Quantum Yield	
	0.216 W Irradiation $\times 10^{-3}$	0.840 W Irradiation $\times 10^{-3}$	0.216 W Irradiation $\times 10^{-4}$	0.840 W Irradiation $\times 10^{-5}$
$\mathbf{Y1_{Fe}}$	7.7(10)	15.9(6)	1.54	1.39
$\mathbf{Y2_{Fe}}$	7.9(6)	23(4)	1.58	1.49

3.4 Ruthenium Analogues

A survey of the literature shows ruthenium has been employed in a variety of CORM systems, although predominately utilized in thermal CORMs. Motterlini *et al.* reported the CO release capabilities of the ruthenium-based CORM-2 (**5**, Figure 8) in 2002.[7] However, this complex suffered from poor solubility in aqueous media. Water solubility was enhanced *via* the coordination of a glycinate ligand to the ruthenium metal centre, yielding CORM-3 (**6**, Figure 8), which is probably the most well-known and widely tested CORM to date. Despite this, clinical development of CORM-3 has been hindered over concerns regarding purification and instability in water and human plasma. Moreover, the complex is thought to undergo a water-gas shift reaction, in which CO is liberated following attack by water to generate CO_2.[119]

Hubbell and co-workers employed polymeric nanocarriers to capture the ruthenium carbonyl core in an attempt to modulate the CO-delivery of CORM-3.[60] The resulting micellar-CORM (**8**, Figure 10) was shown to release CO at a slower rate compared to the parent complex. Furthermore, CO release from the micelles was demonstrated to alleviate inflammation *in vitro* and reduce the cytotoxicity effect elicited from the $Ru(CO)_3Cl$(amino acidate) moiety.

Enhancement of CO delivery through the chemical modification of CORM-3 was also embarked upon by Bernardes and co-workers. Exploiting the chemical instability of the ruthenium carbonyl, Bernardes reports the reaction of CORM-3 hydrolytic decomposition products with proteins *via* a histidine residue.[119] The resulting metalloproteins displayed spontaneous CO release in aqueous media, and were shown to inhibit inflammatory cytokine production. Furthermore, incorporation of the protein albumin exhibited biodistribution tendencies towards tumour cells *in vivo*.

In the field of photoCORMs, Schatzchneider and co-workers developed a number of ruthenium(II) carbonyl complexes featuring polypyridyl ligand architectures (**23**–**25**, Figure 22).[85] These complexes exhibit strong MLCT transitions between 299–326 nm and release CO in response to UV irradiation at 365 nm. Visible light activated ruthenium photoCORMs were first reported by Mascharak in 2013.[100] These complexes fostered

ligand architectures featuring extending conjugation systems. This section discussion the synthesis, structures and photoCORM properties of a series of stable Ru(II) carbonyl complexes, namely $\mathbf{Y1_{Ru}}$, $\mathbf{Y2_{Ru}}$, $\mathbf{Y4_{Ru}}$ and $\mathbf{Y5_{Ru}}$ (Figure 51).

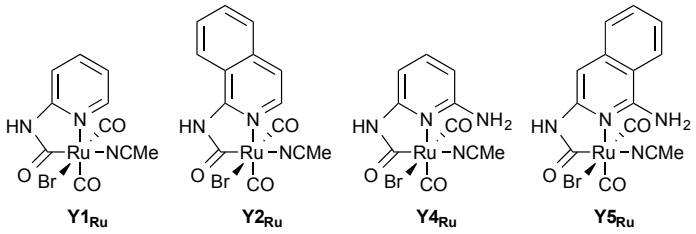

Figure 51: Structures of analogous ruthenium carbonyl complexes

3.4.1 Synthesis of Ruthenium Complexes

Unlike $Fe(CO)_5$, $Ru(CO)_5$ is unstable and must be freshly prepared *via* the method reported by Baird and co-workers.[130] Photoillumination of $Ru_3(CO)_{12}$ (ν_{CO} 2061, 2032 and 2012 cm^{-1}) using a UV-lamp under an atmosphere of CO readily yields a colourless solution of $Ru(CO)_5$ (ν_{CO} 2037 and 2002 cm^{-1}). Cooling to $-40\,°C$ followed by dropwise addition of Br_2 liquid results in the precipitation of $Ru(CO)_4Br_2$ as a yellow solid.[131]

The synthetic pathways of the ruthenium complex is analogous to that of the iron complexes: reaction of $Ru(CO)_4Br_2$ with 2-aminopyridine (2 Eq) in dried dichloromethane resulted the evolution of CO gas and rapid formation of a white precipitate. The precipitate redissolved in the coordinating solvent, acetonitrile. However, owing to the stronger metal–ligand bond strength exhibited by the ruthenium complexes, a halide extracting agent ($AgPF_6$) was required to isolate the neutral complex. Isolation of the isoquinoline derivative followed an identical reaction pathway. Homogeneous X-ray quality crystals were isolated upon cooling. Both complexes harbour the anticipated five-membered metallocyclic ring featuring a carbamoyl functionality, *cis* carbonyl ligands, one bromide and one solvent (MeCN) ligand (Figure 52).

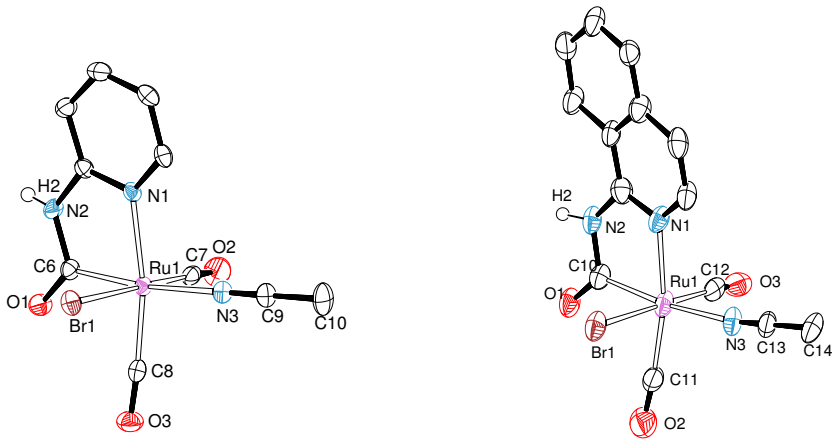

Figure 52: ORTEP representation of $\mathbf{Y1_{Ru}}$ · MeCN (left) and $\mathbf{Y2_{Ru}}$ · MeCN (right) showing 50 % ellipsoids; non-coordinated MeCN and hydrogen atoms except for H(2) have been omitted for clarity

Table 2 shows a comparison of the bond lengths of $\mathbf{Y1_{Fe}}$ and $\mathbf{Y1_{Ru}}$. Bond lengths of the ruthenium complex are typically around 0.1 Å longer than for the iron structure. The bond lengths of the carbamoyl functionality [1.229(3) Å] and [1.238(3) Å] in the both complexes are longer than the metal bound carbonyl ligands ($\mathbf{Y1_{Fe}}$: [1.136(3) Å] and [1.086(3) Å], $\mathbf{Y1_{Ru}}$: [1.136(3) Å] and [1.088(3) Å]). This suggests the carbamoyl functionality is of double bond character whilst the metal bound carbonyl ligands are triplets. Moreover, in both complexes, the carbonyl ligand *trans* to the bromide is shorter than the carbonyl trans to the pyridinyl ligand.

Table 2: Comparison of metrical data for $\mathbf{Y1_{Fe}}$ · MeCN and $\mathbf{Y1_{Ru}}$ · MeCN

	Bond distance/Å	
	$\mathbf{Y1_{Fe}}$ · MeCN	$\mathbf{Y1_{Ru}}$ · MeCN
M−Br	2.4632(5)	2.5613(3)
M−C(6)	1.931(2)	2.012(2)
M−C(7)	1.782(3)	1.884(3)
M−C(8)	1.811(3)	1.909(3)
M−N(1)	1.992(2)	2.112(2)
M−N(3)	2.022(2)	2.187(2)
C(6)−O(1)	1.229(3)	1.238(3)
C(7)−O(2)	1.136(3)	1.136(3)
C(8)−O(3)	1.086(3)	1.088(3)

Initial investigations into the CO release capabilities of $\mathbf{Y1_{Ru}}$ and $\mathbf{Y2_{Ru}}$ focused on monitoring the carbonyl vibrational peaks *via* IR spectroscopy in response to irradiation. A solution of $\mathbf{Y1_{Ru}}$ exhibits three strong carbonyl bands; one at 2061 cm^{-1} and two closely positioned signals at 1998 and 1990 cm^{-1}. Two carbamoyl peaks are observed at 1671 and 1622 cm^{-1}. With regards to $\mathbf{Y2_{Ru}}$, the IR profile consists of the same characteristic peak pattern: three carbonyl peaks at 2061, 2000 and 1991 cm^{-1} and two carbamoyl signals at 1667 and 1631 cm^{-1}.

Comparison for the positions of the carbonyl vibrational bands of the iron and ruthenium complexes reveal the latter reside at a much higher wavenumber (approximately 2047 *vs* 2061 cm^{-1}). The strengthened carbon-oxygen bonds of the ruthenium carbonyls suggest a weakened M−C bond and increased labilisation of CO. Indeed, the larger 4d molecular orbitals of the ruthenium metal centre participates in less efficient overlap with the π^* orbital of the CO ligand, whereas the iron complexes participate in stronger backdonation due to the more efficient overlap of the 3d molecular orbitals. This is a distinct advantage of designing ruthenium-based CORMs over iron-based CORMs. Unfortunately, examination of the UV/Vis spectrum for $\mathbf{Y1_{Ru}}$ and $\mathbf{Y2_{Ru}}$ reveal that neither complex display absorbance bands in the visible region (Figure 54). Unsurprisingly, visible light triggered CO release experiments were unsuccessful. However, monitoring the IR bands in response to UV-irradiation results in rapid loss of the carbonyl bands. Since $\mathbf{Y1_{Ru}}$ and $\mathbf{Y2_{Ru}}$ do not release CO under irradiation of our visible light source, we can be confident that the utilised KL5125 fibre optic lamp only emits wavelengths in the visible region. This acts as a verification tool to authenticate the activation of the iron based photoCORMs *via* visible light.

Incorporation of the isoquinoline ligand results in a significant red shift in absorbance, as well as a greater molar extinction coefficient value compared to the less conjugated, pyridine ligand. The enhanced stability and robustness of the ruthenium analogues lead to the successful isolation of the neutral complex $\mathbf{Y4_{Ru}}$, for which only the charged iron species could be obtained. As incorporation of heteroatoms into the pyridyl conjugation system appeared to have little influence on the electronic absorption spectra, we decided not to pursue this ligand architecture any further. Instead, we designed a ligand framework which combined the extended conjugation system of the isoquinoline

ligand with the presence of an additional amine substituent. Reaction of sodamide with *o*-cyanobenzyl chloride resulted in a variety of aminoheteroaromatic substances including 1-amino-3-formamidoisoquinoline (**48**). This was isolated through a series of water washes, and refluxed with sodium hydroxide to yield 1,3-diaminoisoquinoline (**49**, Scheme 6).[132]

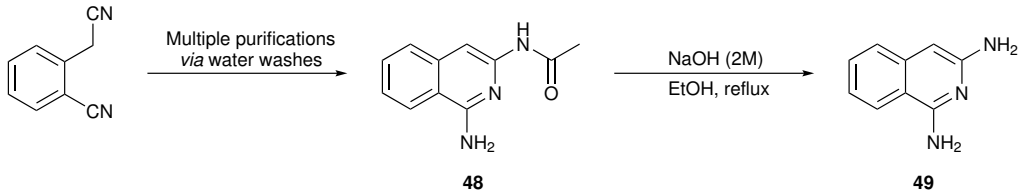

Scheme 6: Scheme for the synthesis of ligand architecture, 1,3-diaminoisoquinoline[132]

The structures of $\mathbf{Y4_{Ru}}$ and $\mathbf{Y5_{Ru}}$ were confirmed *via* X-ray crystallography (Figure 53). Both complexes bear the characteristic five-membered metallocyclic ring, with bound *cis* dicarbonyl ligands. However, the occupation of the sixth ligand (*trans* to the carbamoyl linkage) of $\mathbf{Y5_{Ru}}$ is unique: the bromide ligand occupies the sixth position, with the solvent ligand *trans* to CO. Although the geometry of the complex would be dynamic in solution, it is thought this distinctive geometry is a consequence of crystal packing. Further to this, coordination of the ligand architecture differs from that observed for $\mathbf{Y2_{Fe}}$ and $\mathbf{Y2_{Ru}}$.

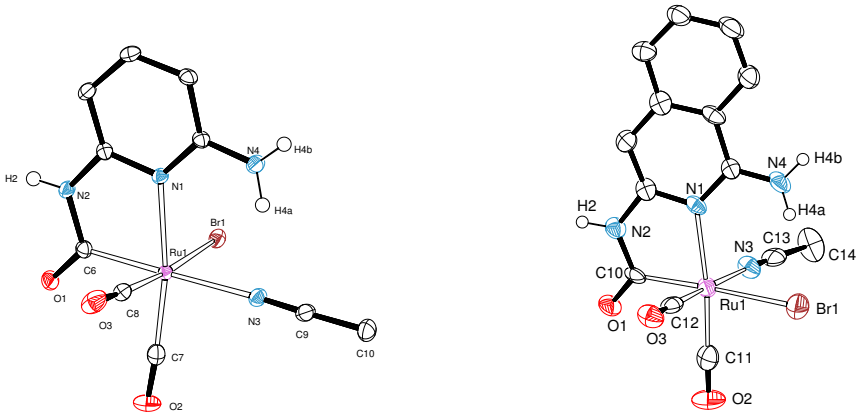

Figure 53: ORTEP representation of $\mathbf{Y4_{Ru}}$ (left) and $\mathbf{Y5_{Ru}}$ · MeCN (right) showing 50 % ellipsoids; hydrogen atoms except for H(2) have been omitted for clarity

The IR spectra for $\mathbf{Y4_{Ru}}$ further confirmed the *cis* carbonyl geometry is maintained (2066 and 2003 cm^{-1}). This was also demonstrated in observing the IR spectra for $\mathbf{Y5_{Ru}}$, with carbonyl signals at 2065 and 2003 cm^{-1}. Although small, based on the stretching frequencies there is a clear strengthening of the C≡O bond in $\mathbf{Y4_{Ru}}$ and $\mathbf{Y5_{Ru}}$ compared to $\mathbf{Y1_{Ru}}$ and $\mathbf{Y2_{Ru}}$. This could be a consequence of reduced back-donation, implying that the NH_2-substituted ligands are poorer electron donors to the metal. The ability of the ligand to donate to the metal depends on the availability of electron density in the pyridyl lone pair, and this may be *reduced* by the inductive effect of the NH_2-substituent.

Examination of the UV/Vis spectrum for $\mathbf{Y4_{Ru}}$ showed incorporation of an additional amino functional group onto the ligand architecture produced a marked increased in the absorption band at 340 nm. The combination of the extended conjugation system and presence of an additional donor functional group results in $\mathbf{Y5_{Ru}}$ displaying an absorption band in the visible region of the spectrum. Despite the notable absorbance peak >400 nm, investigations *via* IR spectroscopy and myoglobin assay revealed no liberation of CO following visible light irradiation.

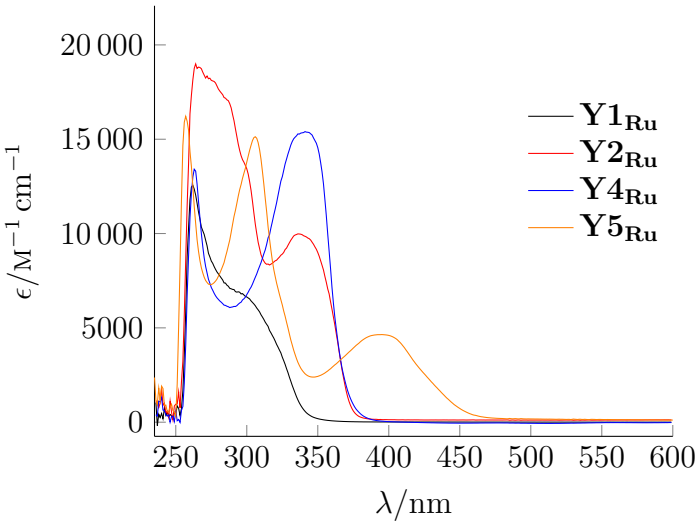

Figure 54: Electronic absorption spectra of $\mathbf{Y1_{Ru}}$, $\mathbf{Y2_{Ru}}$, $\mathbf{Y4_{Ru}}$ and $\mathbf{Y5_{Ru}}$ in DMSO

3.5 Summary

A synthetic route for the generation of metallocyclic carbonyls based on iron and ruthenium has been established. Alterations of the ligand conjugation system modulates the complexes absorption properties. Ligand architectures featuring an additional amine substituent result in a strong MLCT absorbance shifted towards higher wavelengths. Isolation of the corresponding anionic intermediate was successful, with IR evidence of the neutral species in solution. Complexes $\mathbf{Y1_{Fe}}$ and $\mathbf{Y2_{Fe}}$ participate in visible light triggered CO release, as demonstrated *via* IR monitoring and quantified *via* the myoglobin assay. The corresponding ruthenium analogues act as UV-active photo-CORMs. Modification of the ligand framework to incorporate amine substituents was successful. Synthesis and coordination of new ligand 1,3-diaminoisoquinoline resulted in a substantial bathochromic shift of the complexes absorption profile.

Chapter 4

Group 8 Carbonyl Complexes Bearing Thiolated Saccharides

4.1 Introduction

The generation of organometallic CORMs which satisfies the appropriate pharmaceutical properties is extremely challenging. Indeed, organometallic carbonyl complexes are typically reactive towards oxygen and moisture, and as such, are exclusively synthesised in anaerobic conditions, employing dried solvents and inert atmospheric gases. Such complexes would not survive aerobic media and are not suitable for biological applications. There are a small number of exceptions; radiopharmaceutical complexes of the general formula $[M(CO)_3L_3]^+$ (where M = ^{99m}Tc and Re) exhibit excellent air stability and water solubility.[133] Unfortunately, as none of these complexes release CO, little information for CORM development can be obtained from them.

According to Motterlini and Otterbein, the clinical development of CO-releasing carbonyl complexes is dependent on the complex demonstrating a number of pharmaceutical characteristics. These include appropriate water solubility and stability, sufficient biocompatibility, low toxicity pre- and post-CO release and rapid excretion of any '*i*CORM' intermediates.[123] Furthermore, the active species should exhibit sufficient stability to allow administration of the drug (*via* pill, intravenous or topical application), survive the circulation system and only become potent at the targeted tissues.

Through the rational design of the drug sphere it is possible to transform simple carbonyl complexes from their apparent bio-incompatible origins and develop systems suited for biological applications. The coordination of specific ancillary ligands tailored to impart desirable pharmacological properties can modulate traits such as water solubility, toxicity and biocompatibility. Moreover, CORM conjugates can be developed *via* linkages to frameworks including nanoparticles and polymeric cages.[134] In terms of complex stability, a 'happy middle-ground' must be found to, on the one hand, ensure adequate administration and structural integrity *in vivo*, whilst still being susceptible to triggered CO release.

Of course, a CORMs structural integrity and CO release behaviour should not change in the presence of water. Ford and co-workers reported a trianionic tunsten carbonyl complex (**16**, Figure 16) which exhibited a slow back reaction in the presence of water. In this case, water induced CO release was detected *via* IR and UV/Vis spectroscopy.[78] Liao and co-workers experienced similar issues in the development of a α-diketone CORM (**45**, Scheme 4), which was deactivated following hydration of the carbonyl functional groups in the presence of water. To overcome this, the CORM was encaptured in a protective micelle.[104]

Water solubility can be conferred to hydrophobic complexes with the aid of nano-carriers. Nano-carriers are constructed using amphiphilic polymers, where the CORM is encaptured in a lipophilic interior and water solubility is achieved by a hydrophilic exterior. This techniques was used by Zheng and Ford to encage a manganese carbonyl photoCORM bearing two hydrophobic triphenylphosphine ligands. The nanoparticles utilized here consisted of a up-converter component, which absorbed near-IR irradiation and re-emitted visible irradiation that could be re-absorbed by the closely embedded photoCORM.[135]

A survey of the literature revealed the first CORMs to demonstrate water solubility include CORM-3 (**6**, Figure 8) and CORM-A1 (Section 1.6.6).[103,136] The water solubility of **6** is achieved *via* coordination of the biogenic glycine ligand to the ruthenium metal centre. On the other hand, CORM-A1 is a sodium boranocarbonate species and does not contain a transition metal centre. Both complexes contain a carboxylic acid functional

group which is thought to impart water solubility. Indeed, functional groups which particulate in hydrogen bonding increase the overall hydrophilicity of the complex. Conversely, ligand architectures of predominately hydrocarbon character will increase the complexes hydrophobicity. The strategy of employing biologically-compatible ligands was also utilized by Liu and co-workers, who reported the diiron hexacarbonyl complex, **12** (Figure 14). Water solubility was achieved *via* the thioglycol linkages between the two iron centres which harboured a total of four hydroxyl groups.[69] Similarly, the diiron system **32** (Figure 29) developed by Fan and co-workers employ two bridging linkages, each consisting of a deprotonated carboxylic acid functional group which confer water solubility.[93]

An attractive strategy to impart both biocompatibility and water solubility is the incorporation of a sugar moiety onto the active CORM species. Sugars play a number of essential biological roles in the human body, including molecular recognition. Furthermore, they naturally occur with varying repeating units (monosaccharides, oligosaccharides and polysaccharides) all of which are rich in hydrophilic hydroxyl groups. Utilizing sugar components could promote drug delivery to specific tissues, as well as reduce toxicity and influence biodegradation.[137] Lynam and co-workers reported a photoCORM featuring fructopyranose **17**, (Figure 17) which rendered the complex water soluble. Despite being water soluble, the complex suffers from poor stability in aqueous media, liberating CO at a slow rate in the absence of irradiation.[79] Bogdanova and co-workers developed two photoCORMs which incorporated a vitamin B_{12} scaffold. Re-B_{12}CORM (**35**, Figure 31) suffered from cellular uptake issues which was overcome in Mn-B_{12}CORM (**36**, Figure 31), where the carbonyl complex was attached to the vitamin scaffold *via* a ribose sugar moiety. The tricarbonyl ruthenium CORM, ALF-492 (**2**, Figure 3) contains a galactose-derived ligand which significantly enhances the water solubility and biocompatibility of the complex. Furthermore, the sugar moiety confers preferential delivery to the liver by interacting with asialoglycoprotein receptors.[48]

The natural [Fe]-hydrogenase active site (**47**), which our metallocyclic carbonyl complexes are based on, possesses a thiolate functional group in place of the halide (Figure 43). Previous work in our group has successfully demonstrated the substitution of the halide for simple thiolates.[108] Coordination of an aliphatic thiolate resulted in

the generation of a dimeric species, in which the thiolate acts as the bridging linkage. Monomeric species could be isolated by employing bulky aromatic thiols which prevent dimerisation (Figure 55). Building on from the bio-inspired photoCORMs discussed in Chapter 3, this chapter is concerned with enhancing the water solubility and biocompatibility of our complexes. The synthesis, structures and CO-release capabilities of the iron and ruthenium metallocyclic complexes modified with thiolated saccharides is discussed.

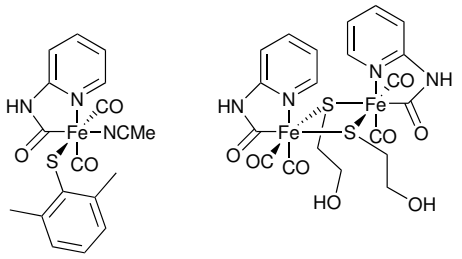

50 **51**

Figure 55: Previously isolated monomeric and dimeric thiolated species[108]

4.2 Synthesis of Ferracyclic Complexes bearing Thiolated Saccharides

Naturally occurring substances have been shown to have beneficial influences on CORM behaviour.[61,119,133,134] One avenue for promoting biocompatibility and water solubility is the coordination of saccharide molecules. Furthermore, carbohydrates can act as biomarkers for molecular recognition, which could play a critical role in drug delivery. An appropriate candidate is 1-thio-β-D-glucose, which could be reliably synthesised following the procedure reported by Davis and co-workers (Scheme 7).[138]

The 1-thio-β-D-glucose could be coordinated to the iron metal centre *via* substitution of the halide (Scheme 8). The reaction was completed in dry methanol and follows the same pathway previously observed for simple thiolates.[108] Introduction of the monosaccharide was accompanied with new IR absorbances (in MeOH) at 2046, 2025 and 1977 cm^{-1} for $\mathbf{D1_{Fe}}$ and at 2048, 2025 and 1980 cm^{-1} for $\mathbf{D2_{Fe}}$. Mass spectral analysis produced hits

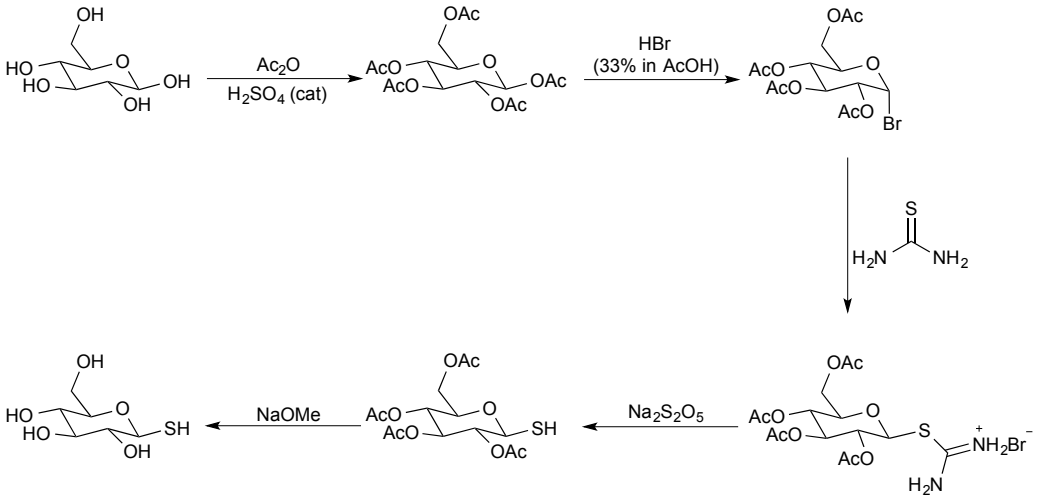

Scheme 7: Synthesis of 1-thio-β-D-glucose[138]

corresponding to a dimeric structure. X-ray quality crystals of $\mathbf{D2_{Fe}}$ were obtained following slow evaporation of the solvent.

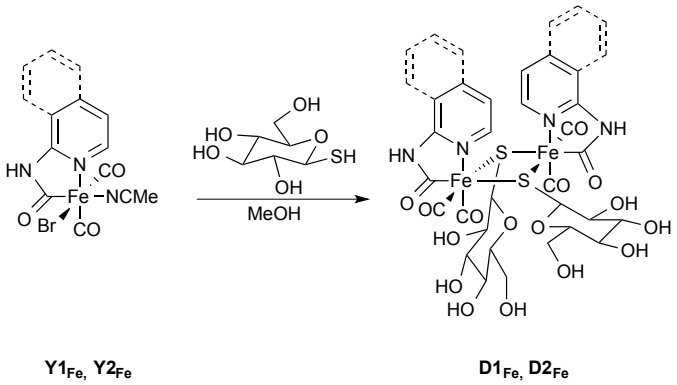

Scheme 8: Synthesis of ferracyclic photoCORMs bearing thiolated saccharide ligands

As shown in Figure 56, two thioglucose molecules acts as bridging linkages between the two metal centres. Clearly, the ring structure of the sugar is not sufficiently bulky to prevent dimerisation. The thioglucose derivatives proved to be significantly more soluble in aqueous media compared to the first generation complexes. $\mathbf{D1_{Fe}}$ which bear the smaller pyridyl ligand framework was shown to be completely soluble in water. The presence of the extended aromatic system of $\mathbf{D2_{Fe}}$ seemed to hinder total water solubility, requiring small traces (2 %) of DMSO to achieve complete dissolution.

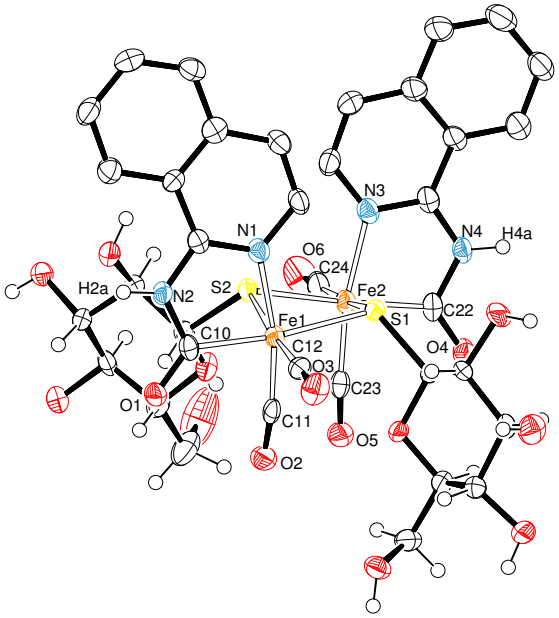

Figure 56: ORTEP representation of $\mathbf{D2_{Fe}} \cdot 2\,\mathrm{MeOH} \cdot 1.5\,H_2O$ showing 50 % ellipsoids; solvent molecules and hydrogen atoms bound to carbon have been omitted for clarity

The electronic absorbance profiles further demonstrate the dimeric nature of the new complexes; the molar extinction coefficient values appear to be much greater than the parent complexes. However, on a per metal basis, we find similar molar extinction coefficients values. $\mathbf{D1_{Fe}}$ exhibits a strong MLCT absorbance band at 303 nm which (like the parent complexes) trails into the visible region of the spectrum. The extended conjugation system of $\mathbf{D2_{Fe}}$ generates MLCT absorption bands at 282 and 288 nm with an additional absorbance at 337 nm which trails into the visible. Both complexes have a yellow appearance. The molar extinction coefficients in the visible region appears to be greater in the dimeric species ($>2000\,\mathrm{M^{-1}\,cm^{-1}}$) compared to the parent complexes ($1500–2000\,\mathrm{M^{-1}\,cm^{-1}}$). All complexes are stable in DMSO in the absence of light. However, these complexes break down with loss of CO when expose to visible light

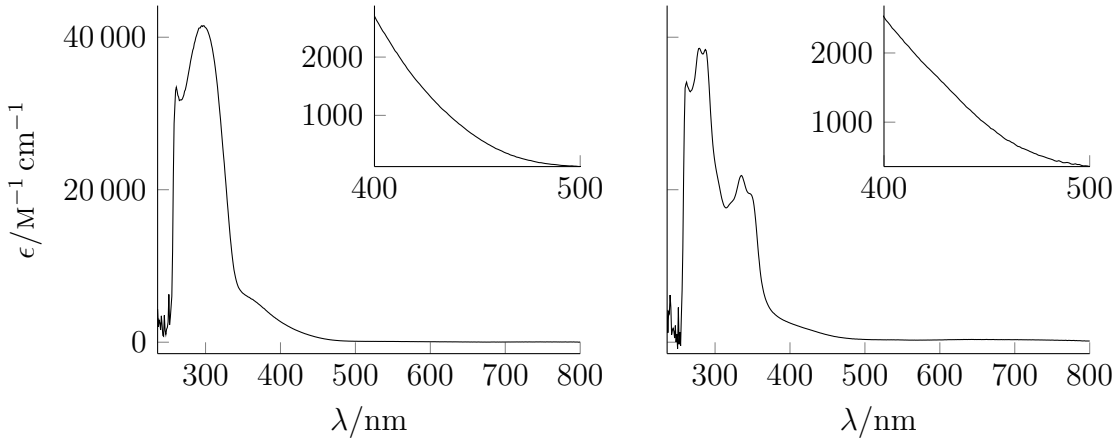

Figure 57: Comparison of the electronic absorption spectra of $\mathbf{D1_{Fe}}$ (left) and $\mathbf{D2_{Fe}}$ (right) in DMSO

4.2.1 Quantification of CO Release

4.2.2 IR Spectroscopy

The IR profile for $\mathbf{D1_{Fe}}$ contains carbonyl peaks at 2046, 2025 and 1977 cm^{-1}. The carbomoyl absorbance is observed at 1674 and 1622 cm^{-1}. The extended conjugation system of $\mathbf{D2_{Fe}}$ gives rise to carbonyl stretches observed at approximately the same wavenumbers: 2048, 2025, 1980, 1675 and 1622 cm^{-1}. Photo-dissociation of each complex was screened using a broadband visible light source operated at two different powers; 'low power' (0.216 W) and 'high power' (0.840 W). Figure 58 shows the contrasting CO-release capability of $\mathbf{D2_{Fe}}$ when exposed to each light intensity. Following 'low power' irradiation, steady release of CO was observed over a time course of 60 min. CO release behaviour was significantly enhanced following 'high power' irradiation, where rapid CO loss was observed within the first 10 min.

Inspection of the dimeric species quantum yield values (Table **??**) reveal an approximate 6 fold increase under 'high power' conditions compared to the first generation complexes. This offers an explanation of the marked difference in CO release behaviour observed at the two different light intensities.

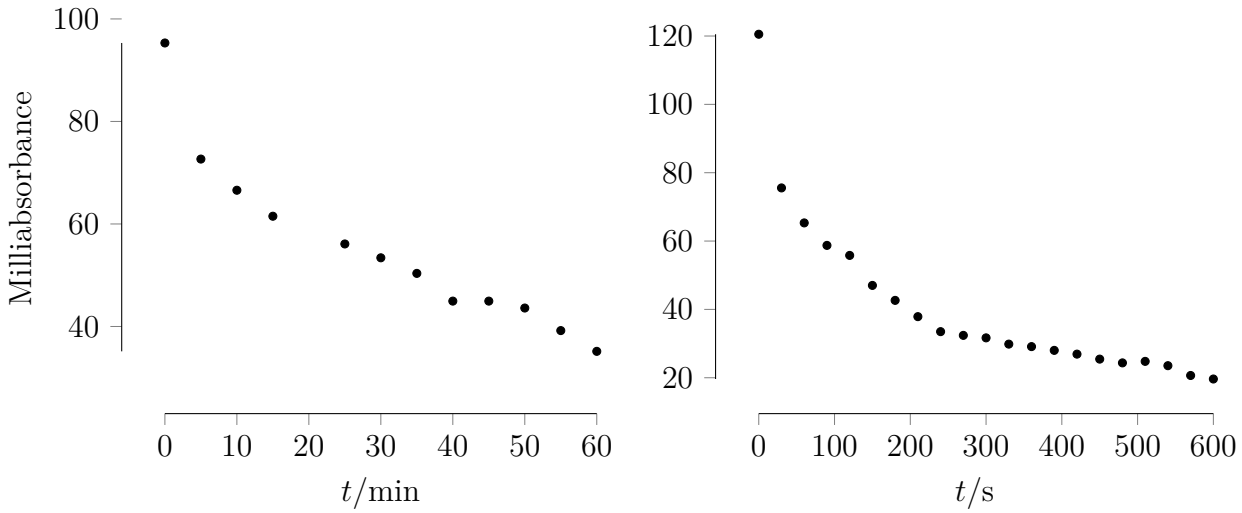

Figure 58: IR carbonyl intensity at 2037 cm^{-1} of $\mathbf{D2_{Fe}}$ following visible light irradiation at 'low power' (left) and 'high power' (right) in DMSO

Table 3: table showing rates of CO release and quantum yield for first generation complexes $\mathbf{Y1_{Fe}}$ and $\mathbf{Y2_{Fe}}$, and second generation $\mathbf{D1_{Fe}}$ and $\mathbf{D2_{Fe}}$ complexes

Complex	Average Apparent Rate (µM/ min)		Quantum Yield	
	0.216 W Irradiation $\times 10^{-3}$	0.840 W Irradiation $\times 10^{-3}$	0.216 W Irradiation $\times 10^{-4}$	0.840 W Irradiation $\times 10^{-5}$
$\mathbf{Y1_{Fe}}$	7.7(10)	15.9(6)	1.54	1.39
$\mathbf{Y2_{Fe}}$	7.9(6)	23(4)	1.58	1.49
$\mathbf{D1_{Fe}}$	17.1(15)	107(6)	1.70	9.31
$\mathbf{D2_{Fe}}$	17.5(4)	111(4)	1.74	9.67

4.2.3 Myoglobin Assay

The CO release behaviour of the thioglucose derivatives was quantified using the myoglobin assay. For these measurements, dissolution of $\mathbf{D1_{Fe}}$ was achieved in pure water whilst $\mathbf{D2_{Fe}}$ required a H_2O-DMSO (49 : 1) mixture. Visible light-induced CO release was monitored at 'low power' and 'high power'. Figure 59 displays the marked difference in response between these two light intensities.

For both complexes, steady liberation of CO is observed following 'low power' irradiation. Increasing the light intensity rapidly accelerates photodissociation of CO. Furthermore,

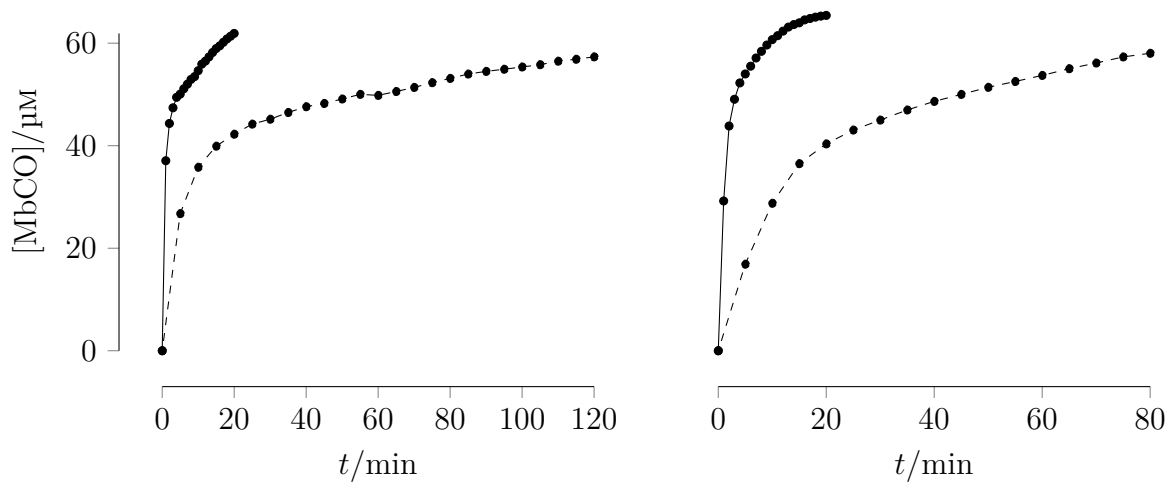

Figure 59: Plot of the amount of MbCO formed *via* CO liberated from $\mathbf{D1_{Fe}}$ (30 µM, left) and $\mathbf{D2_{Fe}}$ (30 µM, right) (Dashed: 0.216 W irradiation Solid: 0.840 W irradiation)

the assay suggests a change in mechanism: analysis of the myoglobin data of the monomeric species reveal the rate of MbCO formation can be fitted using a single exponential function, whereas the dimeric complexes require a two-term exponential growth (Figure 60). This is indicative of a two-step process in which initial CO loss occurs rapidly following irradiation of visible light, followed by slower release of a second CO equivalent. This is suggestive of the formation of an intermediate species, and possible breakage of the dimeric system following CO release. Unfortunately, we have been unable to identify or isolate any such intermediates.

Surprisingly, assay data from $\mathbf{D1_{Fe}}$ and $\mathbf{D2_{Fe}}$ confirmed the release of only one CO equivalent per metal centre. In contrast, both metal bound CO molecules are liberated from the parent monomeric complexes, $\mathbf{Y1_{Fe}}$ and $\mathbf{Y2_{Fe}}$. In order to understand this contrasting difference in CO release capability, we employed density functional theory (DFT). This allows for the prediction of spectroscopic properties from frontier orbital energies extracted from structures with optimised geometries.

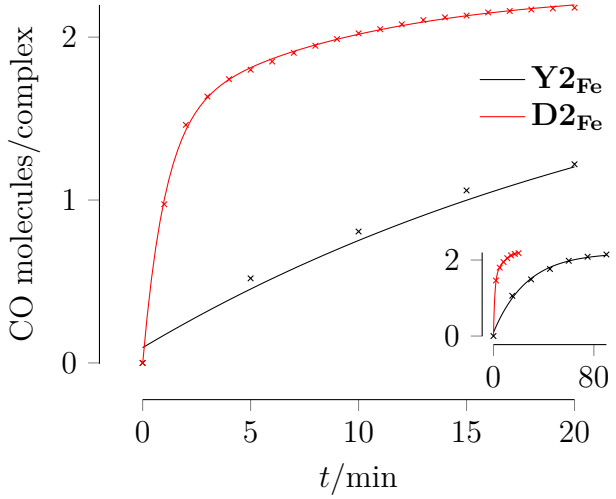

Figure 60: Comparative plot of the amount of MbCO formed *via* CO liberated from **Y2$_{Fe}$** (30 µM, black) and **D2$_{Fe}$** (30 µM, red) following 0.840 W Irradiation. Points: experimental data; Lines: exponential fits. Inset shows full time course for release from **Y2$_{Fe}$**

4.3 DFT Calculations

Modern computational processing power means that simulation of molecular properties is almost routine for many classes of compound. DFT methods in particular offer a balance between computational complexity and accuracy of results which is useful for organic and organometallic systems of up to roughly fifty atoms. In particular, geometry optimisation and the subsequent prediction of ground state properties is now extremely common in guiding understanding of reactive intermediates.

The disposition of molecular orbitals is automatically available from DFT optimisations of ground state structure. These calculations make it possible to examine the principal locations of the frontier orbitals. The nature of the lowest unoccupied molecular orbital (LUMO) is significant in predicting light-driven CO dissociation. Transfer of electron density into this anti-bonding orbital will facilitate CO loss where the nodal planes occur between the metal and carbonyl group(s). Thus DFT calculation of LUMO data provides insight into the readiness of a system to liberate CO. In systems bearing multiple carbonyl ligands, DFT can also suggest which groups are most likely to be

labile.

We employed this strategy in an attempt to rationalise how the substitution of the thiolate ligand may have altered the metal 3d orbital contribution to the bound CO ligands. These DFT calculations were based on optimized structured using X-ray coordinates when possible. Optimized structures showed good agreement in terms of bond lengths and angles with the respective X-ray structures. Figure 61 shows the highest occupied molecular orbital (HOMO) and lowest unoccupied molecular orbital (LUMO) for complex $\mathbf{Y1_{Fe}}$. The calculated electronic transitions within the range of absorbances experimentally observed to release CO (*i.e.* ≥400 nm) include HOMO → LUMO (448 nm), HOMO-1 → LUMO-1 (419 nm) and HOMO → LUMO-1 (407 nm). We have focused on the molecular orbital (MO) electron densities of the HOMO and LUMO orbitals in order to examine their relative contributions to facilitate CO loss.

Through DFT we can predict the likely positions of these orbitals and evaluate whether there is sufficient MO overlap between the metal d orbitals and the orbitals of the carbonyl to facilitate CO loss. For $\mathbf{Y1_{Fe}}$, the HOMO and LUMO molecular orbitals are distributed such that there is adequate overlap with both carbonyl ligands.

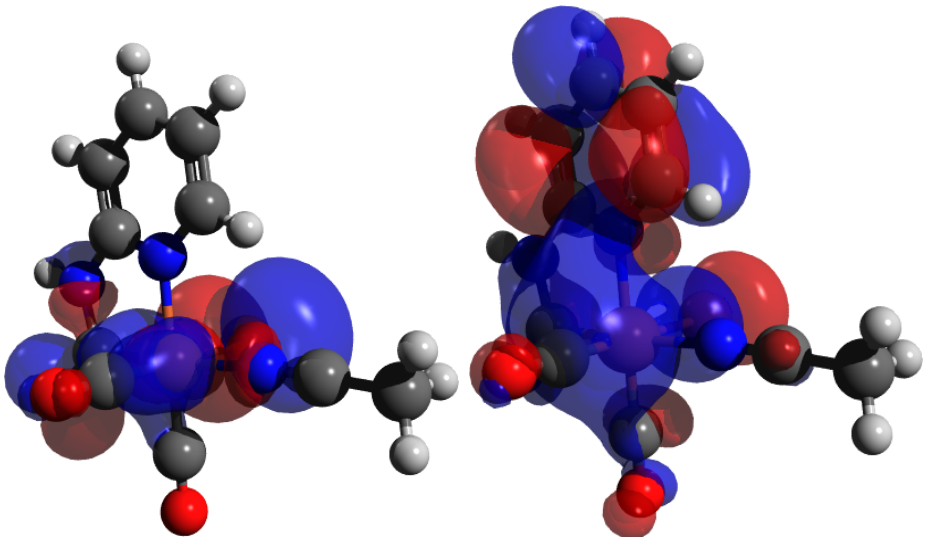

Figure 61: Simulated HOMO orbitals (left) and LUMO orbitals (right) of complex $\mathbf{Y1_{Fe}}$

The DFT calculations performed for $\mathbf{D1_{Fe}}$ would be much more computationally demanding due to simulating the high number of terminal hydroxyl groups. We decided to model the thiolate substitute as a simple methyl thiolate.

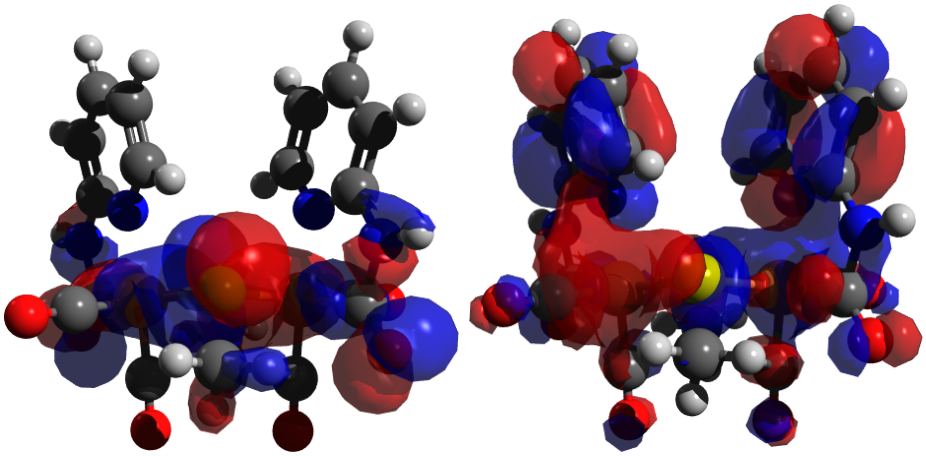

Figure 62: Simulated HOMO orbitals (left) and LUMO orbitals (right) of complex $\mathbf{D1_{Fe}}$

As shown in Figure 62, the molecular orbital contribution to the carbonyl ligand *trans* to the pyridyl architecture is significantly less pronounced compared to that of the parent complex. These findings correlate with the observed experimental behaviour that only one metal bound CO (per metal centre) is liberated during photolysis.

This fundamental change in MO contribution is thought to be a direct result of replacing the halide for thiolate. However, the dimeric nature of the thioglucose derivatives is also likely to play a critical role in modulating molecular orbital locations. In order to associate the decreased labicity of the CO ligand with either the introduction of the thiolate, or the dimeric structure (or indeed both), DFT simulation of a monomeric structure fostering a thiolate ligand was performed.

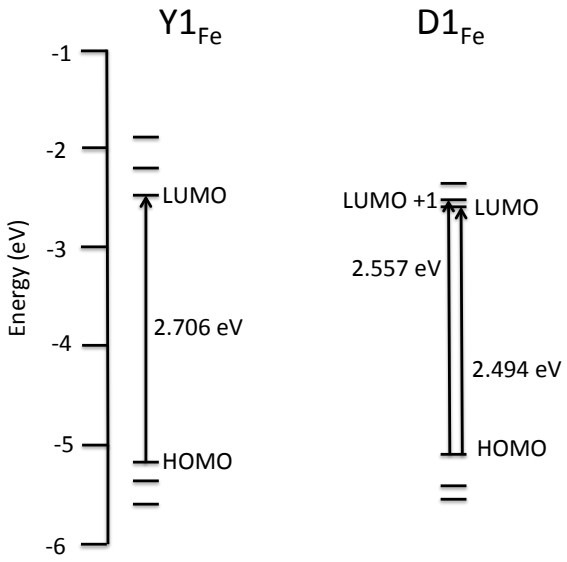

Figure 63: Calculated energy diagram for $\mathbf{Y1_{Fe}}$ (left) and $\mathbf{D1_{Fe}}$ (right). Most likely transitions are in accordance with experimental observations.

This entailed DFT calculations on a five coordinate ferracyclic structure analogous to 'half' the dimeric structure. As shown in Figure 64, the monomeric thiolate derivative possesses adequate HOMO/LUMO coverage of both M−CO bonds. The data therefore suggests the dimeric nature is responsible for the lessened CO release capabilities of $\mathbf{D1_{Fe}}$ and $\mathbf{D1_{Fe}}$.

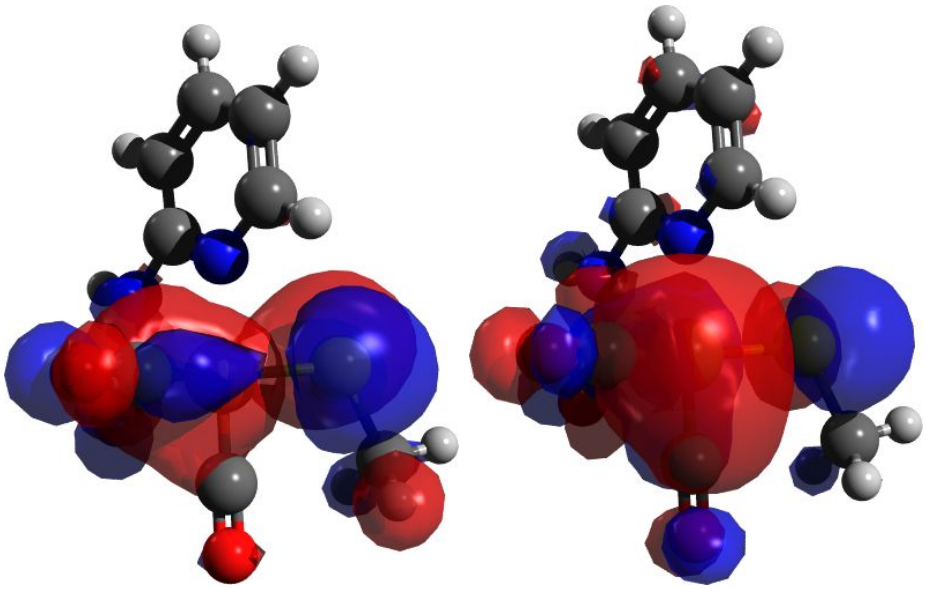

Figure 64: Simulated HOMO orbitals (left) and LUMO orbitals (right) of a five-coordinate monomeric structure bearing a thiolate ligand

4.4 Synthesis of Ruthenium Metallocycles Bearing Thiolated Saccharides

To enhance the water solubility and biocompatibility of our ruthenium carbonyls, we replicated the introduction of a thiolated saccharide ligand. Treatment of $\mathbf{Y1_{Ru}}$ with 1-thio-β-D-glucose quickly yielded $\mathbf{D1_{Ru}}$. This chemistry was extended for the remaining ruthenium analogues in the synthesis of $\mathbf{D2_{Ru}}$, $\mathbf{D4_{Ru}}$ and $\mathbf{D5_{Ru}}$ (Figure 65). Conveniently, the generation of these ruthenium derivatives could be achieved *via* reaction of 1-thio-β-D-glucose with the ruthenium salt intermediate, thereby eliminating the requirement to obtain the neutral complex following halide extraction.

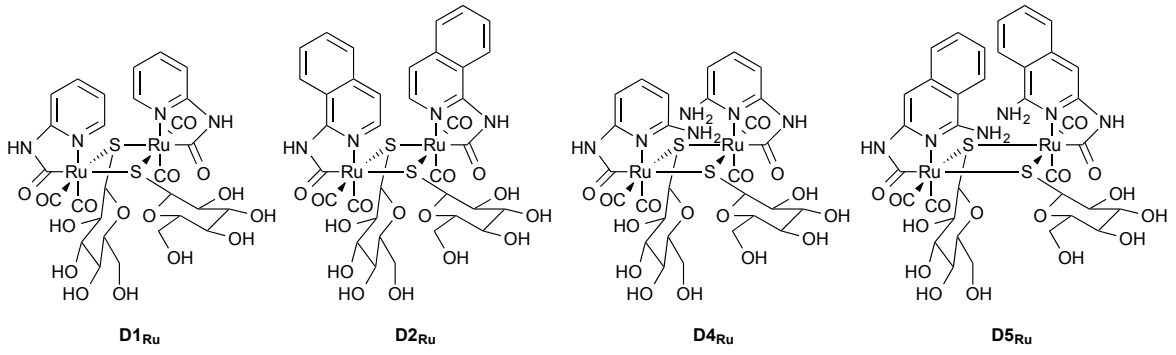

Figure 65: Ruthenium metallocycles bearing thiolated saccharides

The IR spectra of $\mathbf{D1_{Ru}}$, $\mathbf{D2_{Ru}}$, $\mathbf{D4_{Ru}}$ and $\mathbf{D5_{Ru}}$ exhibit a characteristic shift in carbonyl bands upon thiolate coordination to lower wavenumber. Furthermore, $\mathbf{D1_{Ru}}$ and $\mathbf{D2_{Ru}}$, which consist of the pyridine and more conjugated isoquinoline architectures each display a carbonyl stretch at 2060–2062 cm^{-1}. Along with this, the spectra exhibits another carbonyl peak at 2047–2050 cm^{-1} which features a shoulder absorption. However, for $\mathbf{D4_{Ru}}$ and $\mathbf{D5_{Ru}}$, in which the ligand framework bears an additional amine group, the two carbonyl bands observed (2060–2062 cm^{-1} and 1993–1994 cm^{-1}) did not feature any shoulder absorbances.

Introduction of the monosaccharide yielded a dimeric structure analogous to the iron structures, which was confirmed *via* X-ray crystallography (Figure 66). Light yellow prism shaped crystals of $\mathbf{D2_{Ru}}$ were isolated *via* the slow evaporation of methanol. The

coordination geometry around the ruthenium centre is distorted octahedral, featuring *cis* carbonyl ligands: one *trans* to the nitrogen atom of the pyridine ligand, and the other *trans* to the thiolate bridge.

Table 4 shows a comparison of the iron and ruthenium structure bond lengths. The metal − ligand bond lengths are uniformly longer in the ruthenium structure.

Table 4: Comparison of metrical data for $\mathbf{D2_{Fe}} \cdot 2\,\mathrm{MeOH} \cdot 1.5\,H_2O$ and $\mathbf{D2_{Ru}} \cdot 3\,\mathrm{MeOH} \cdot 1.5\,H_2O$

	Bond distance/Å	
	$\mathbf{D2_{Fe}} \cdot 2\,\mathrm{MeOH} \cdot 1.5\,H_2O$	$\mathbf{D2_{Ru}} \cdot 3\,\mathrm{MeOH} \cdot 1.5\,H_2O$
M(1)−S(1)	2.372(3)	2.442(2)
M(1)−N(1)	2.019(5)	2.126(5)
M(1)−C(10)	1.926(5)	2.022(5)
M(1)−C(11)	1.786(6)	1.900(6)
M(1)−C(12)	1.782(7)	1.900(6)
C(10)−O(1)	1.239(6)	1.242(6)
C(11)−O(2)	1.136(7)	1.131(7)
C(12)−O(3)	1.135(8)	1.128(8)

The electronic absorption spectra for $\mathbf{D1_{Ru}}$, $\mathbf{D2_{Ru}}$, $\mathbf{D4_{Ru}}$ and $\mathbf{D5_{Ru}}$ are shown in Figure 67. In DMSO, $\mathbf{D1_{Ru}}$ exhibits a MLCT absorption band predominately of UV-character, with a peak absorbance at 260 nm and a broad energy band at 306 nm, which trails to 350 nm. The extended π-system of $\mathbf{D2_{Ru}}$ results in a fundamental increase in the molar extinction coefficient. Furthermore the spectra reveals an additional peak at 337 nm, which is characteristic of previous complexes fostering this ligand architecture.

When comparing the absorption spectra between the corresponding iron and ruthenium carbonyls, of significant importance is the extent to which each absorption extends. For example, when comparing $\mathbf{D2_{Fe}}$ and $\mathbf{D2_{Ru}}$, the absorption band consequence of the isoquinoline ligand framework resides at 337 nm for both complexes. However, in the case of the iron derivative, the absorption band trails significantly beyond the UV-region and well into the visible. In contrast, the respective ruthenium equivalent exhibits an absorption band which rapidly falls off at approximately 375 nm. Indeed, it is the

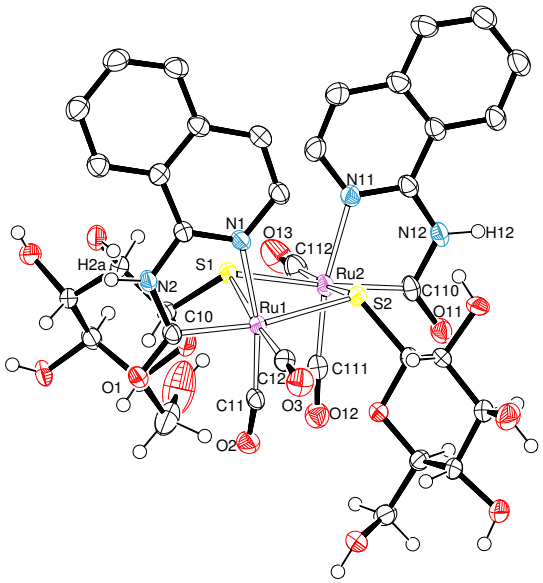

Figure 66: ORTEP representation of $\mathbf{D2_{Ru}} \cdot 3\,\mathrm{MeOH} \cdot 1.5\,H_2O$ showing 50 % ellipsoids; solvent molecules and hydrogen atoms bound to carbon have been omitted for clarity

nature of the transition metal centre, as well as the ligand architecture, which dictates the fundamental photosensitivity of these complexes.

The photosensitivity of the system towards lower energies is enhanced considerably upon the inclusion of an additional nitrogen donor atom onto the ligand system ($\mathbf{D4_{Ru}}$). It is clear to see the absorption profile consequence of this modification strategy trumps that of simply extending conjugation system, at least in terms of extinction coefficients. However, the ligand framework which harbours both the extended conjugation system and an additional nitrogen donor group produces the greatest bathochromic shift. The electronic absorption spectra for $\mathbf{D5_{Ru}}$ displays absorption bands at 258 and 314 nm in the UV-region, with a strong absorption band at 388 nm which trails into the visible.

IR monitoring of $\mathbf{D5_{Ru}}$ revealed the complex releases CO upon irradiation with 'high power' and 'low power' visible light (Figure 68). This is in contrast to the corresponding monomeric complex ($\mathbf{Y5_{Ru}}$) which proved to be inert towards visible light.

Visible light activation of $\mathbf{D5_{Ru}}$ was confirmed *via* myoglobin assay (Figure 69). CO

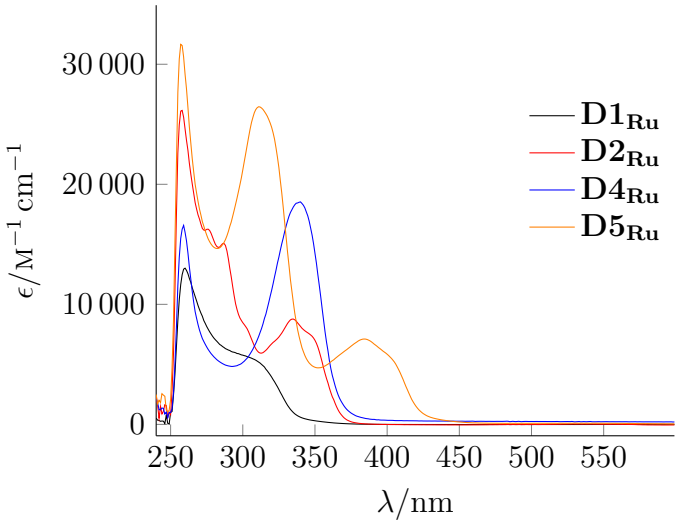

Figure 67: Electronic absorption spectra of $\mathbf{D1_{Ru}}$, $\mathbf{D2_{Ru}}$, $\mathbf{D4_{Ru}}$ and $\mathbf{D5_{Ru}}$ in DMSO

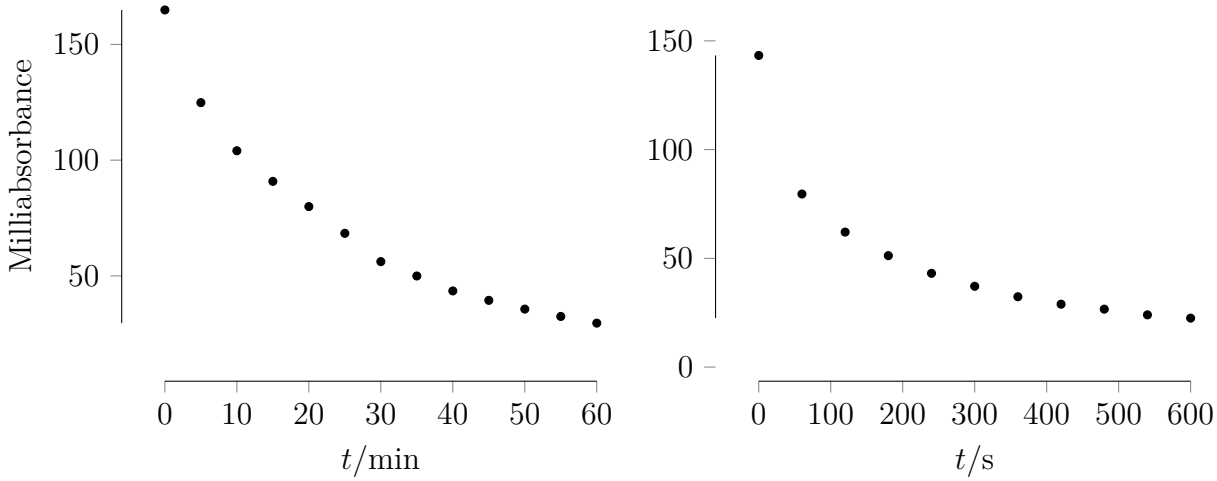

Figure 68: IR carbonyl intensity at 2050 cm^{-1} of $\mathbf{D5_{Ru}}$ following visible light irradiation at 'low power' (0.216 W, left) and 'high power' (0.840 W, right) in DMSO

release behaviour following 'high power' irradiation is similar to that observed for $\mathbf{D1_{Fe}}$ and $\mathbf{D2_{Fe}}$; all three complexes released two equivalents of CO within 20 minutes. However, there is a stark difference in CO release capability upon irradiated using 'low power' visible light. Complexes $\mathbf{D1_{Fe}}$ and $\mathbf{D2_{Fe}}$ successfully released two CO equivalents over the course of two hours, whereas $\mathbf{D5_{Ru}}$ only released approximately one equivalent.

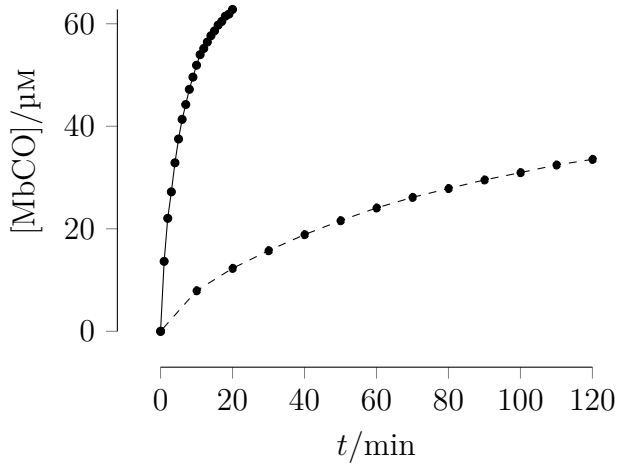

Figure 69: Plot of the amount of MbCO formed *via* CO liberated from $\mathbf{D5_{Ru}}$ (30 μM) (Dashed: 'low power' (0.216 W) irradiation, Solid: 'high power' (0.840 W) irradiation)

4.5 Summary

In summary, we have demonstrated that the water solubility of the parent complexes can be significantly enhanced following coordination of thioglucose. The resulting dimeric iron carbonyl complexes undergoes CO liberation in response to irradiation with visible light. In contrast to the monomeric parent complexes, which was shown to liberate both metal bound CO ligands, the thioglucose derivatives have been observed to only release one equivalent per metal centre.

Inspection of the molecular orbital contribution *via* DFT modelling offers an explanation

for this surprising difference. In the first generation complexes, both CO groups exhibit significant LUMO contributions which facilitate labilisation by irradiation. In contrast, DFT calculations reveal the LUMO position in the dimeric structures is localised on only one of the CO position. The lack of photodissociation of the second CO group is likely due to the distinct absence of LUMO contribution at the M−CO bond. Further inspection suggests the determining factor is not the substitution of the thiolate for halide, but a direct result of the dimeric structure.

The CO release behaviour can be modulated *via* the intensity (or brightness) of the visible light irradiation. For $\mathbf{D1_{Fe}}$, the rate of CO release is vastly increased in response to 'high power' irradiation, such that generation of MbCO during the myoglobin assay plateaued after only 20 minute. The same concentration of MbCO required six times (120 minute) the irradiation time following application of 'low power' visible light.

The synthetic route for incorporation of a thiolated sugar moiety has also been established for the ruthenium metallocycles. The increased light sensitive of the dimeric species results in $\mathbf{D5_{Ru}}$ releasing CO following visible light activation. This is in contrast to the corresponding monomeric species, $\mathbf{Y5_{Ru}}$ which requires higher energy UV-irradiation.

Chapter 5

In vitro Anti-Inflammatory Assays

5.1 Introduction

Quantifying CORM activity in terms of rate and equivalents of CO released is well established. Indeed, IR spectroscopy (Section 2.1.1) can be readily employed to monitor CO loss over time and the myoglobin assay (Section 2.1.3) can provide quantitative data on the amount of CO liberated. However, studies detailing CORM activity *in vitro* are comparatively rare. This aspect of CORM development is vitally important, as drug behaviour in biological systems (*in vitro* and *in vivo*) could completely contradict results observed in the chemistry lab. The most common *in vitro* investigation performed is cell viability, which accesses the impact of the drug on cell survival (Section 2.3.1). Cell viability assays have been reported for a number of CORM systems.[90,92,93,104]

In 2002, Green and co-workers became the first research group to administer carbonyl complexes capable of mimicking the therapeutic actions of gaseous CO in biological systems.[7] This study evaluated the cytotoxicity and cardiac protection provided by $Mn_2(CO)_{10}$ (**4**) and $[Ru(CO)_3Cl_2]_2$ (**5**, Figure 8). Complex **4** displayed no detectable cytotoxicity at concentrations in the range 0–100 µmol L^{-1}. Assessments of **5** also displayed no cytotoxicity across a range of useful concentrations (0–400 µmol L^{-1}), but did exhibit toxicity issues at very high concentrations (>400 µmol L^{-1}) after prolonged periods of time. Complexes **4** and **5** were shown to alleviate vessel contractility: *in vitro* studies using aortic ring models which had been precontracted with phenylephrine

showed rapid and significant vasodilatory effects following administration of **5**. The therapeutic action of this ruthenium carbonyl was attributed to CO, as addition of myoglobin (which scavenges free CO) significantly reduced the overall vasodilatation observed. Infusion of N^G-nitro-L-arginine methyl ester (L-NAME) into rats hearts caused an increase in the coronary perfusion pressure (CPP). Administration of **4** or **5** was shown to alleviate this condition. In the case of **4**, light-activated CO release resulted in a delayed onset of vasoconstriction with significantly lower levels of CPP. Administration of this carbonyl complex without light activation produced no vasodilatation effect.

Building upon this work, Motterlini and co-workers evaluated the biological actions of the first water soluble CORM, CORM-3 (**6**, Figure 8).[58] Cardiac protection by **6** was demonstrated in models of ischemia-reperfusion injury and cardiac allograft rejection. Complex **6** was shown to cause vasorelaxation in a concentration dependent manner using precontracted aortic rings. Moreover, a long-lasting protective effect was observed: higher concentrations of contracting agent were required to re-contract the aortic rings after CORM administration.[8] Later, Motterlini and co-workers introduced a series of iron-based CORMs including **52** (Figure 70).[35] Cell viability demonstrated no detectable cytotoxicity issues at concentration range 10–100 µmol, with toxicity issues becoming pronounced at >200 µmol. Vasodilatation was monitored using isolated aortic rings precontracted with phenylephrine, and anti-inflammatory properties were observed following administration of the endotoxin, lipopolysaccharide (LPS).

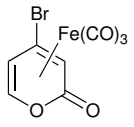

52

Figure 70: Iron-containing CORM reported by Motterlini and co-workers[35]

Romão and co-workers demonstrated the *in vitro* and *in vivo* CO release properties of a series of molybdenum carbonyl complexes, including the previously reported, *fac*-[$Mo(CO)_3$(histidinate)]Na (**53**, Figure 71).[139] This complex was shown to release CO when exposed to molecular oxygen. However, oxygen activation of the complex also

led to the formation of ROS, which can result in damage to cellular structures *via* oxidative stress. Despite this drawback, **53** has been successfully implicated to bring about therapeutical actions in a variety of animal models including lowering arterial blood pressure.[140]

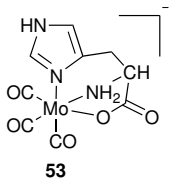

53

Figure 71: Molybdenum tricarbonyl complex reported by Meder and co-workers,[139] CORM properties investigated by Romão and co-workers[140]

Beyond toxicity monitoring, accessing a photoCORMs ability to induce a CO-related therapeutic action has received much less attention. Mascharak and co-workers monitored the vessel dilatation effect of a series of *fac*-$Mn(CO)_3$ based photoCORMs. In this study, light induced vasorelaxation of mouse aortic muscle rings was achieved in a concentration-dependent manner. No vasorelaxation was observed under dark conditions or was inhibited in the presence of sGC inhibitor, ODQ.[141,142] Bogdanova and co-worker accessed the cytoprotective influence of **36** (Mn-B_{12}CORM, Figure 31) on fibroblast cells under hypoxia conditions.[96] Following administration with **36**, the culture dishes were either irradiated with white light or kept in the dark. Photoactivation of the photoCORM was shown to significantly reduce the number of dead cells under hypoxia conditions compared to cultures kept in the dark. Poole and co-workers evaluated the anti-microbial activity of the manganese-based photoCORM, **27** (Figure 24) developed by Schatzschneider and co-workers.[87,143] Their findings demonstrated growth inhibition and a decreased in viability of an antibiotic-resistant uropathogenic strain of *E.coli* following administration and illumination of **27** at 365 nm. Administration of the CORM without light irradiation yielded no therapeutic effects. In this chapter, we evaluate the biological activities of complexes $\mathbf{Y1_{Fe}}$, $\mathbf{Y2_{Fe}}$, $\mathbf{D1_{Fe}}$, $\mathbf{D2_{Fe}}$ and $\mathbf{Y1_{Ru}}$ by analysing their anti-inflammatory properties *in vitro*. This is achieved by utilizing the Enzyme Linked Sorbent Assay (ELISA, Section 2.3.3) which quantifies the production of LPS-stimulated pro-inflammatory cytokine, TNF-α.

5.2 Accessing Anti-Inflammatory Behaviour

The cytokine Tumour Necrosis Factor (TNF-α) is a pro-inflammatory mediator and has been implemented in a number of inflammatory processes in several immune-mediated inflammatory diseases.[144] These includes regulatory behaviour in rheumatoid arthritis,[145] Crohn's disease,[146] multiple sclerosis[147] and uveitis.[148] Indeed, raised TNF-α levels in transgenic mice caused the development of arthritis pathophysiologically similar to human rheumatoid arthritis.[149] Pharmacological inhibition of this cytokine has been shown to have beneficial effects, including preventing cardiovascular issues including myocardial infarction.[150,151]

The biological activities of TNF-α are mediated by two receptors: primary receptor TNF-R1 ($p55$) mediates the pro-inflammatory effects of TNF-α, and TNF-R2 ($p75$), which belongs to the same family despite being functionally distinct to TNF-R1, is involved in signalling attributed to TNF-α mediated effects such as skin necrosis and apoptosis of activated T-cells.[152,153]

Strategies for reducing the activity of this pro-inflammatory cytokine usually involve employing biological products to bind to TNF-α, thereby blocking its activity. These biological products include monoclonal antibodies and fusion proteins.[144] Blockage, or neutralisation of TNF-α causes the suppression of inflammatory cytokines downstream the signalling pathway, including IL-1 and IL-6.[154] Moreover, inflammatory processes are inhibited *via* suppression of adhesion molecules that promote leukocyte activation and migration. O'Connell and co-workers have recently developed a series of flavonoid metabiolites which have been shown to reduce the secretion of TNF-α.[155]

However, TNF-α also appears to be involved in signalling pathways which regulate or limit the severity and duration of the inflammatory response.[156] This *in vivo* behaviour was shown to operate through the regulation of macrophage, interleukin IL-12. and suggested complete blockage of TNF-α may cause adverse complications. Indeed, studies have attributed reactivation of tuberculosis and development of ocular inflammatory with the inhibition of TNF-α.[157]

When screening for the therapeutic actions of CO, it is useful to review the beneficial

roles of HO-1, which acts as the body's main source of endogenously produced CO. In particular, HO-1 has been shown to protect the organism from a number of chronic pathologies of which inflammation is a common condition. Poss and Tonegawa demonstrated this using HO-1 deficient mice which were shown to exhibit significantly greater amounts of inflammatory stress compared to the control group.[18] Exogenous administration of CO has been shown to mimic the protective effects of HO-1 in inhibiting the production of pro-inflammatory cytokines.[5,28–30]

The potential anti-inflammatory capability of CORMs can be gauged by monitoring the drugs influence on the production of pro-inflammatory cytokines following administration of endotoxin, lipopolysaccharide (LPS). In a study performed by Motterlini and co-workers, macrophages were treated with LPS to cause the production of TNF-α. Administration of CORM-3 (**6**, Figure 8) was shown to significantly reduce the production TNF-α. Furthermore, administration of an inactive '*i*CORM' control was shown to have no effect on the production of LPS-induced TNF-α. This validates it is indeed CO which attenuates the anti-inflammatory response.[158] Surveying the literature, this type of anti-inflammatory assay has not be used to evaluate the therapeutic behaviour of photoCORMs. It has, however, been successfully utilized by Motterlini and co-workers as a means of establishing the anti-inflammatory properties of **6**.[158]

5.2.1 Protocol

To probe the anti-inflammatory properties of our complexes, we adopted a non-standard protocol to achieve light activated CO release *in vitro*. THP-1 cells (0.5×10^6 cells/well) were seeded in a 24-well plate. The cell line was cultured in RPMI 1640 medium, supplemented with 10 % foetal bovine serum, L-glutamine (2 mM), penicillin (100 U/mL) and streptomycin (100 µg mL^{-1}). Cells cultures were maintained *via* incubation at 37 °C in a humidified atmosphere with 5 % CO_2. Cell passages used were between 5 and 20.

Production of pro-inflammatory cytokine TNF-α was stimulated *via* addition of LPS (1.0 µg mL^{-1} final concentration). Bardoxolone methyl (50 µM final concentration) was used as a positive control for an anti-inflammatory response. As further controls, THP-1

cells were treated with vehicle (DMSO), and each condition was analysed in the presence or absence of LPS (referred to as 'unstimulated' and 'stimulated' samples, respectively). Furthermore, each condition was analysed in the presence or absence of light, in order to verify any adverse effects irradiation with visible light might have on the cells cultures. The 24-well plate was covered in tin-foil with black dye containing wells separating the light irradiated samples from the dark condition samples (Figure 72, left). Visible light irradiation of specific wells was achieved by carefully cutting sections into the tin-foil which would expose only the desired well (Figure 72, right). Irradiation of cells operated at 'high intensity' for a duration of 10 min per well, set at a distance of 5.0 cm above the cell culture.

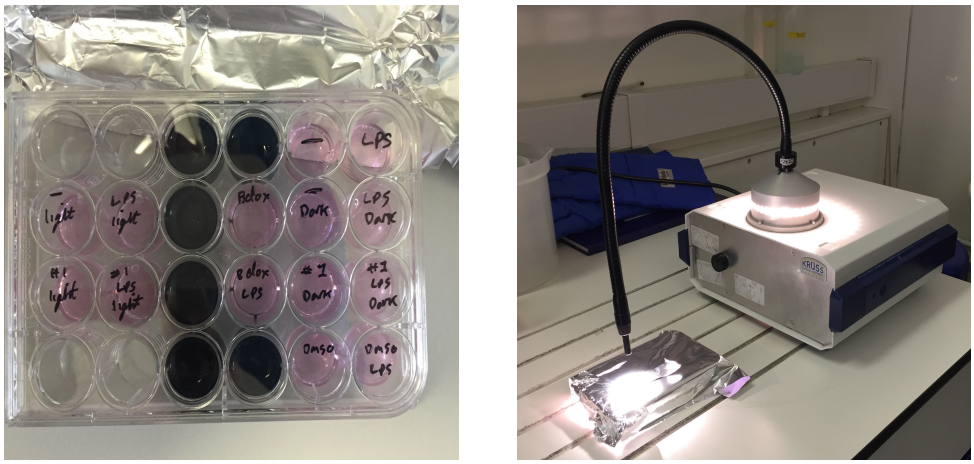

Figure 72: THP-1 cells seeded to a 24-well plate, protected from light using tin-foil (left), light source setup to achieve well-specific irradiation (right)

A prior experiment determined $\mathbf{Y1_{Fe}}$ required 30 min incubation period (37 °C) to allow sufficient cellular uptake. Cell samples were treated with the desired CORM to give a final concentration of 50 µM. After the 30 min incubation period, cells in the 'stimulated' conditions were administrated with LPS. Cells in the light condition were irradiated with visible light, followed by an incubation period of 3 h (37 °C). Cytokine concentrations in supernatants was quantified using the human ELISA kit. Briefly, TNF-α standards and supernatant samples (100 µL) were added to a 96-well plate precoated with an THP-1 anti-body and incubated for 2 h at room temperature. Plates were washed with PBS/0.05 % Tween-20 followed by addition of an enzyme-linked secondary anti-body

(100 µL) into each well. After a further incubation period of 1 h, the plate was washed and substrate solution (100 µL) was added to each well. The plate, whilst being shielded from light, was allowed to develop for 30 min. The reaction was stopped by addition of H_2SO_4 (50 µL, 1 M). Absorbance measured at 450 nm and calibrated to the absorption readings of the TNF-α standards.

5.3 Cell Viability Assays

Before accessing the therapeutic anti-inflammatory properties of our complexes, preliminary cell viability studies of $\mathbf{Y1_{Fe}}$ were carried out[159] on HL-60 and THP-1 cell lines using the MTS assay.[121] Cells were treated with $\mathbf{Y1_{Fe}}$ at varying concentrations (1 mM → 1 µM). After an incubation period of 72 h, analysis of cell morphologies showed cytotoxicity issues at the highest drug concentration only (1 mM), with no detectable cytotoxicity at concentrations of 100 µM, 10 µM and 1 µM. Cell viability data is summarized in Figure 73, which includes a vehicle control (DMSO).

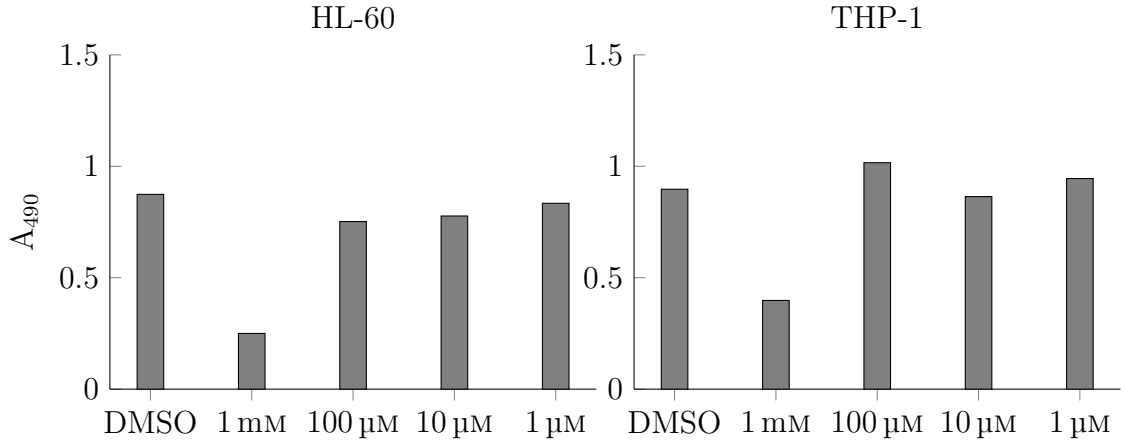

Figure 73: Viability of HL-60 and THP-1 cell lines after 72 h incubation with $\mathbf{Y1_{Fe}}$, as determined by the MTS assay. Absorbance at 490 nm is proportional to the number of viable cells[121]

5.4 Accessing Anti-Inflammatory Properties

The anti-inflammatory role of CO is well-established,[5,6,15,29,46] with a number of publications demonstrating CORM intervention into the inflammatory progress.[158,160] Due to the absence of such biological demonstrations with regards to photoCORMs, we decided to probe whether our systems hindered an LPS-induced inflammatory response *in vitro*. Figure 74 shows the amount of TNF-α produced for each experimental condition. The 'unstimulated' samples are represented in blue and the 'stimulated' samples in red. As our complexes were administrated in a DMSO solution, we included a DMSO vehicle control. A positive control for anti-inflammatory activity employed bardoxolone methyl (abbreviated 'bardox') which inhibits the transcription factor (NF-κB) involved in inflammation.[161]

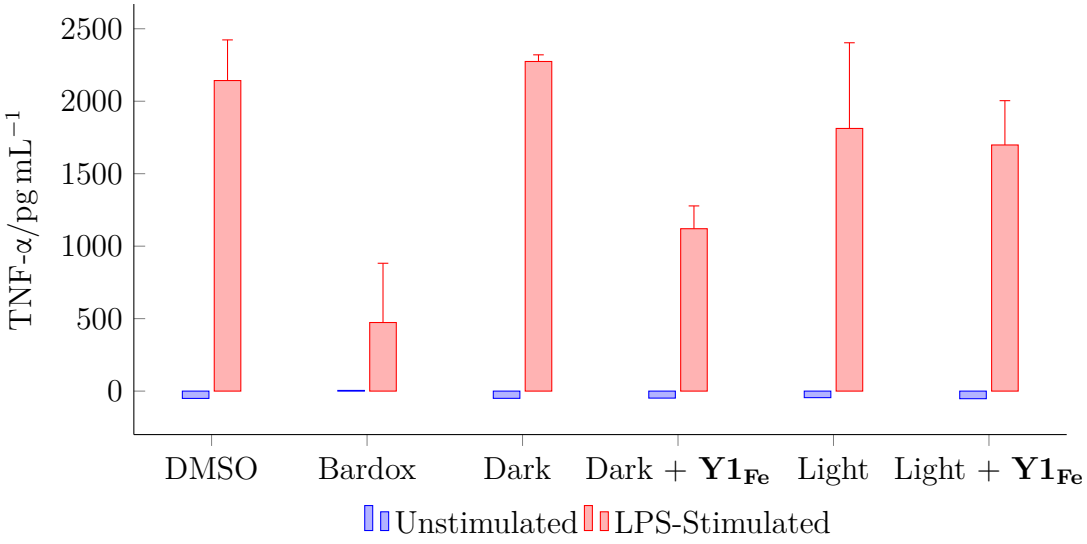

Figure 74: Effect of $\mathbf{Y1_{Fe}}$ on LPS-stimulated TNF-α production. Unstimulated and LPS-stimulated THP-1 cells were exposed to light and dark conditions in the presence or absence of $\mathbf{Y1_{Fe}}$

Interestingly, production of TNF-α was inhibited most predominately following administration of $\mathbf{Y1_{Fe}}$ to cells shielded from light (Dark + $\mathbf{Y1_{Fe}}$ sample). This *in vitro* behaviour contradicted data obtained from IR spectroscopy and Mb assay, which suggested visible light irradiation was necessary for CO release. Indeed, CORM admin-

istration followed by light irradiation of the cells with visible light did elicit a small anti-inflammatory response. However, the ability of $\mathbf{Y1_{Fe}}$ to attenuate the LPS-induced production of TNF-α was significantly greater in the non-irradiated samples.

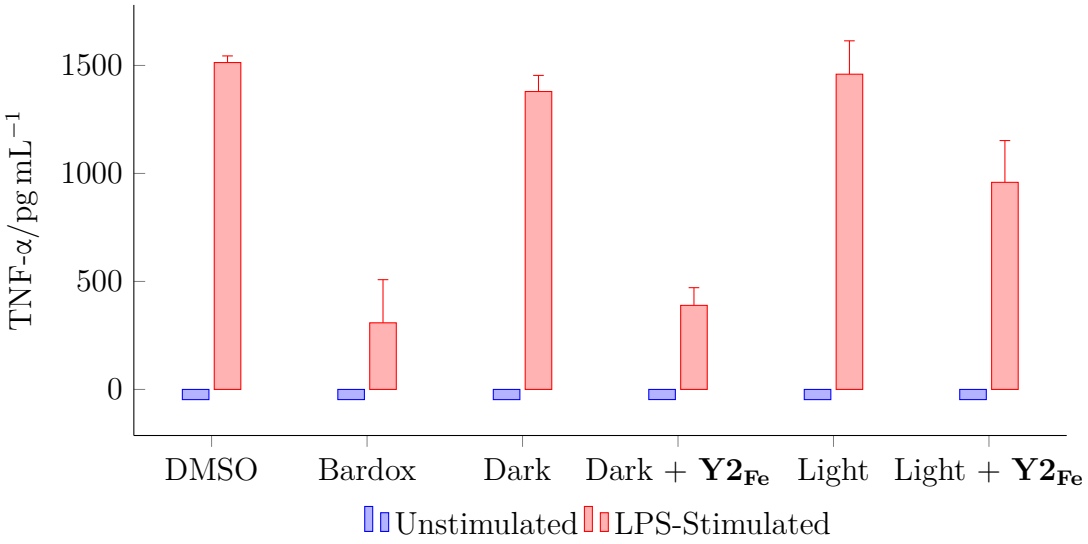

Figure 75: Effect of $\mathbf{Y2_{Fe}}$ on LPS-stimulated TNF-α production. Unstimulated and LPS-stimulated THP-1 cells were exposed to light and dark conditions in the presence or absence of $\mathbf{Y2_{Fe}}$

This unexpected *in vitro* behaviour was mimicked in $\mathbf{Y2_{Fe}}$. Administration of $\mathbf{Y2_{Fe}}$ followed by cell irradiation resulted in a notable decrease in the production of TNF-α. However, as shown in Figure 75, TNF-α production was significantly hindered following addition of $\mathbf{Y2_{Fe}}$ to cells kept in the dark (Dark + $\mathbf{Y2_{Fe}}$ sample). The amount of activity elicited by each CORM species can be calculated by dividing the amount of TNF-α produced following CORM administration from the amount produced in the corresponding control sample (identical conditions, except no CORM added). From this, the degree of anti-inflammatory activity can be represented as a percentage. Figure 76 displays a comparative view of the activities of $\mathbf{Y1_{Fe}}$ and $\mathbf{Y2_{Fe}}$ in both light and dark conditions.

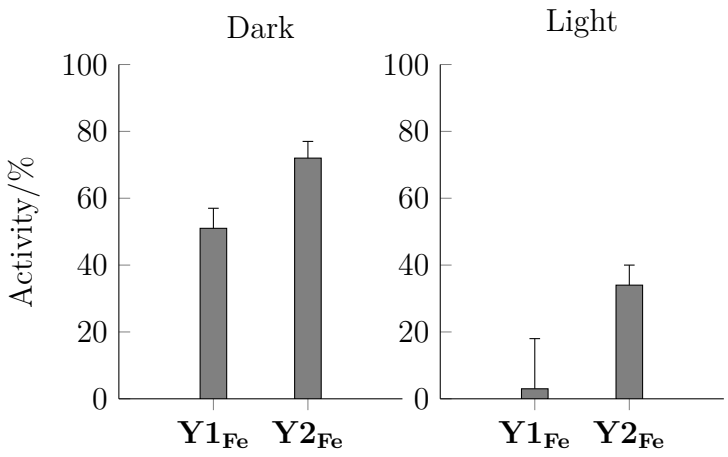

Figure 76: Comparison of the anti-inflammatory activities of $\mathbf{Y1_{Fe}}$ and $\mathbf{Y2_{Fe}}$ to reduce to the production of pro-inflammatory cytokine, TNF-α

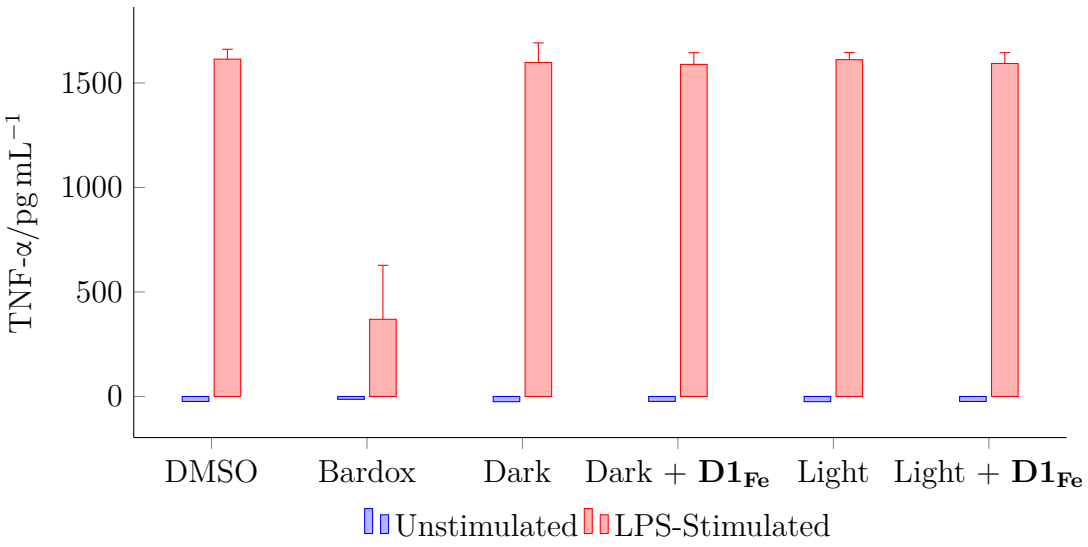

Figure 77: Effect of $\mathbf{D1_{Fe}}$ on LPS-stimulated TNF-α production. Unstimulated and LPS-stimulated THP-1 cells were exposed to light and dark conditions in the presence or absence of $\mathbf{D1_{Fe}}$

Having established anti-inflammatory responses produced from $\mathbf{Y1_{Fe}}$ and $\mathbf{Y2_{Fe}}$, we investigated the ability of $\mathbf{D1_{Fe}}$ and $\mathbf{D2_{Fe}}$ to attenuate LPS-induced TNF-α production under the same conditions. Disappointingly, despite their significantly enhanced water solubility, dimerisation of the iron complexes proved to be detrimental to their ability to neutralise inflammation. As shown in Figure 77, $\mathbf{D1_{Fe}}$ displayed no detectable capability to regulate the production of TNF-α. $\mathbf{D2_{Fe}}$ displayed greater anti-inflammatory

properties to that of $\mathbf{D1_{Fe}}$. However, modulation of inflammation remained poor, as displayed in Figure 78.

Interestingly, the *in vitro* properties of the dimeric species appeared to be identical under both light and dark conditions. This contrasts with the data collected for the monomeric species, which displayed significantly greater activity in the dark. A number of explanations can be suggested for the lack of activity demonstrated by $\mathbf{D1_{Fe}}$ and $\mathbf{D2_{Fe}}$, the most obvious cause being poor cellular uptake. Lipinski's 'rule of five', which is based on a number of experimental and computational investigations, describes desirable drug characteristics which favour uptake into the cell.[162] Firstly, to ensure sufficient permeation of the cellular membrane, the drug molecule should not have a molecular weight exceeding $500\,\mathrm{g\,mol^{-1}}$. Monomeric species $\mathbf{Y1_{Fe}}$ and $\mathbf{Y2_{Fe}}$ adhere to this rule, with molecular weights of 353.9 and $404.0\,\mathrm{g\,mol^{-1}}$, respectively. In contrast, dimerisation yielded molecular weights of 855.0 and $1046.9\,\mathrm{g\,mol^{-1}}$ for $\mathbf{D1_{Fe}}$ and $\mathbf{D2_{Fe}}$, respectively. Moreover, functionalisation with the thioglucose ligands resulted in each CORM harbouring a total of eight hydroxyl groups. Despite imparting water solubility, drugs containing more than five hydrogen donor groups exhibit poorer permeability of the membrane lipid bi-layer. Further to this, drugs which exhibit a lipohilicity reading of $\log P > 5$, and those fostering more than ten hydrogen bond acceptor groups were found to display impaired permeability of the membrane bi-layer.[162]

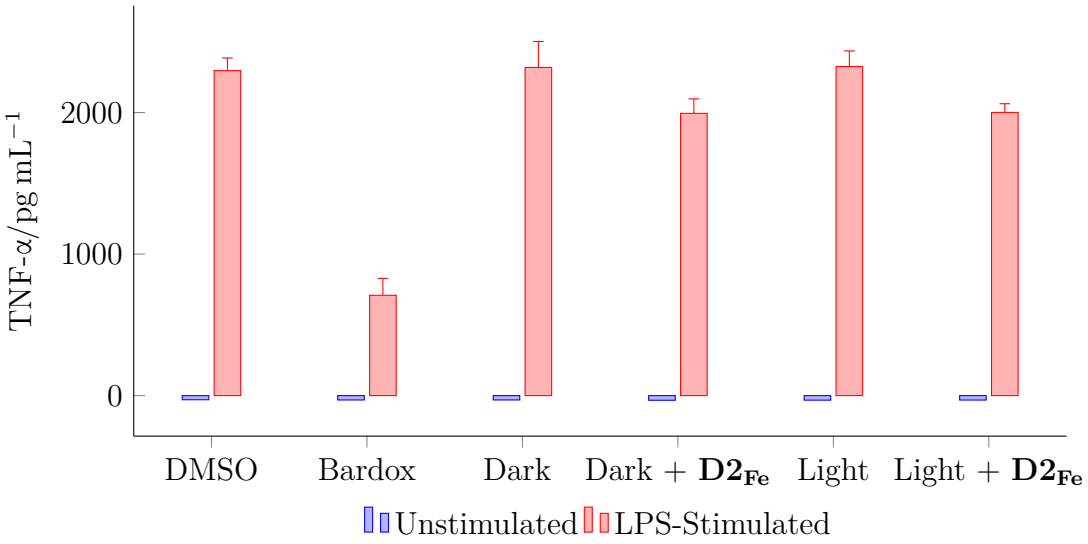

Figure 78: Effect of $\mathbf{D2_{Fe}}$ on LPS-stimulated TNF-α production. Unstimulated and LPS-stimulated THP-1 cells were exposed to light and dark conditions in the presence or absence of $\mathbf{D2_{Fe}}$

To further investigate the bioactivities displayed by $\mathbf{Y1_{Fe}}$ and $\mathbf{Y2_{Fe}}$ in the absence of light, we decided to probe the anti-inflammatory properties of the ruthenium analogue, $\mathbf{Y1_{Ru}}$. As discussed in Chapter 2, $\mathbf{Y1_{Ru}}$ does not release CO when irradiated with visible light and requires activation using UV light. As reported in Figure 79, treatment of $\mathbf{Y1_{Ru}}$ to THP-1 caused a marginal decrease to the production of LPS-induced TNF-α. As expected, visible light stimulation had no bearing on the degree of activity observed.

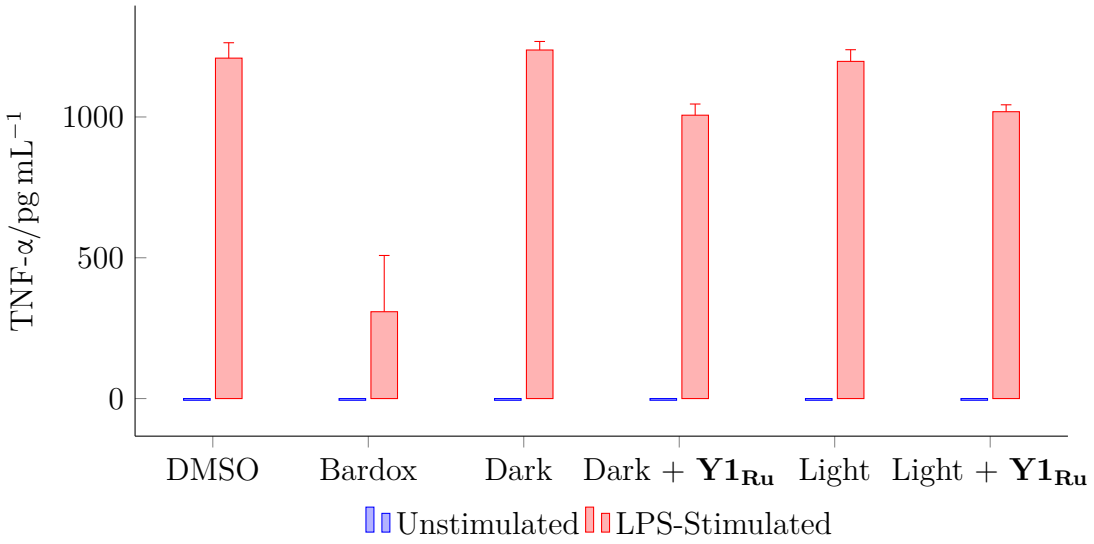

Figure 79: Effect of $\mathbf{Y1_{Ru}}$ on LPS-stimulated TNF-α production. Unstimulated and LPS-stimulated THP-1 cells were exposed to light and dark conditions in the presence or absence of $\mathbf{Y1_{Ru}}$

Figure 80 displays a comparative view of the activities of $\mathbf{Y1_{Fe}}$, $\mathbf{Y2_{Fe}}$, $\mathbf{D1_{Fe}}$, $\mathbf{D2_{Fe}}$ and $\mathbf{Y1_{Ru}}$ in both light and dark conditions. The overall bioactivies are clear: monomeric species $\mathbf{Y1_{Fe}}$ and $\mathbf{Y2_{Fe}}$ exhibit ample therapeutic benefit in the absence of light, with less activity detected following visible light irradiation. *In vitro* properties of $\mathbf{D1_{Fe}}$, $\mathbf{D2_{Fe}}$ and $\mathbf{Y1_{Ru}}$ display minimal inhibition of TNF-α. At this stage, it is clear more experimental data is required to fully appreciate the underlying factors behind these variations. However, one may consider several potential factors which could modulate drug efficiency.

Pre-incubation of CORM species with THP-1 cell cultures to facilitate cellular uptake was limited to 30 min. The extent of CORM population which successfully entered the cell may be vastly different between the smaller monomeric and larger dimeric species. Furthermore, the rate of light triggered CO release from $\mathbf{D1_{Fe}}$ and $\mathbf{D2_{Fe}}$ was shown to be appreciably accelerated compared to the monomeric species. Therefore the distinct lack of anti-inflammatory activities could in fact be a consequence of hindered cellular uptake coupled with prematurely triggered rapid CO release to the solution media.

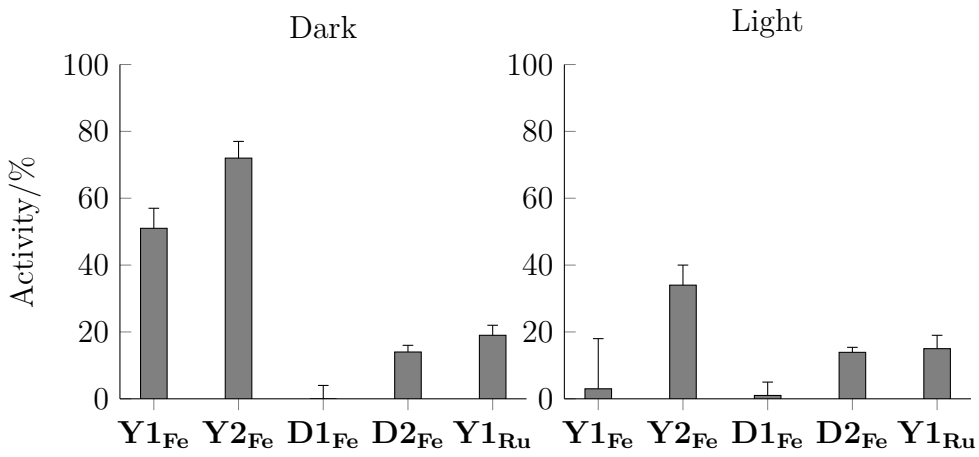

Figure 80: Comparison of the anti-inflammatory activities of $\mathbf{Y1_{Fe}}$, $\mathbf{Y2_{Fe}}$, $\mathbf{D1_{Fe}}$, $\mathbf{D2_{Fe}}$ and $\mathbf{Y1_{Ru}}$ to reduce to the production of pro-inflammatory cytokine, TNF-α

Of course, this does not explain why CORMs harbouring the isoquinoline architecture ($\mathbf{Y2_{Fe}}$ and $\mathbf{D2_{Fe}}$) exhibit a greater anti-inflammatory effect than their smaller, pyridyl containing counterparts ($\mathbf{Y1_{Fe}}$ and $\mathbf{D1_{Fe}}$). However, as stated previously, increased hydrophobicity of the drug sphere infers betters drug permeability of the cellular membrane. It is reasonable to speculate that the increased potency of the former complexes ($\mathbf{Y2_{Fe}}$ and $\mathbf{D2_{Fe}}$) may be caused by a higher local concentration inside the cellular environment.

Perhaps most notable is the contrasting bioactivities of $\mathbf{Y1_{Fe}}$ and $\mathbf{Y1_{Ru}}$. The two complexes display significantly different anti-inflammatory properties. Drug activation *via* molecular recognition of the ligand framework seems unlikely. As shown in Table 5, bond lengths are around 0.1 Å longer for ruthenium than for iron, but there is no obvious link between this elongation and bioactivity. On the other hand, cells utilize a variety of transition metals for the generation of metalloproteins. Intracellular trafficking of different metal ions allow the cells to direct usable metals to specific protein sites whilst managing concentration levels to prevent cytotoxicity issues.[163] For example, cellular uptake of iron is promoted *via* interaction of the extracellular transferrin protein, with regulation of iron concentration in the cytoplasm achieved *via* ferritin, which is an intracellular protein capable of scavenging and storing free iron. Therefore one might speculate the dark conditioned activation of our iron complexes may be facilitated *via* involvement with iron-specific cellular machinery. This could offer an explanation for

the superior activity of $\mathbf{Y1_{Fe}}$ compared to $\mathbf{Y1_{Ru}}$, for which activation is limited to interaction with proteins capable of docking ruthenium.

Table 5: Comparison of metrical data for $\mathbf{Y1_{Fe}}$ · MeCN and $\mathbf{Y1_{Ru}}$ · MeCN

	Bond distance/Å	
	$\mathbf{Y1_{Fe}}$ · MeCN	$\mathbf{Y1_{Ru}}$ · MeCN
M−Br	2.4632(5)	2.5613(3)
M−C(6)	1.931(2)	2.012(2)
M−C(7)	1.782(3)	1.884(3)
M−C(8)	1.811(3)	1.909(3)
M−N(1)	1.992(2)	2.112(2)
M−N(3)	2.022(2)	2.187(2)

5.5 Summary

The field of carbon monoxide releasing molecules is still in its infancy, with the first reported CORMs reported little over a decade ago.[7] Sophisticated detection methods enable accurate quantification of the rate and equivalents of CO released. However, for a carbonyl complex to be truly verified as a CORM, its pharmacological properties must be probed *in vitro* and *in vivo*. Surveying the literature revealed the most commonly employed *in vitro* CORM characteristic being investigated is cytotoxicity, with a comparatively smaller number of CORMs demonstrated to elicit a therapeutic response.

To this effect, we probed the ability of our complexes to inhibit the LPS-induced production of the pro-inflammatory cytokine, TNF-α. Surprisingly, the anti-inflammatory properties of the monomeric iron systems ($\mathbf{Y1_{Fe}}$ and $\mathbf{Y2_{Fe}}$) was shown to be most active in the dark. Inspection of the potency of dimeric species $\mathbf{D1_{Fe}}$ and $\mathbf{D2_{Fe}}$ revealed a significant reduction in bioactivity under the same experimental conditions, which could be a consequence of impeded cellular uptake and non-productive, light triggered CO release outside the cellular environment. We reasoned the *in vitro* therapeutic activities observed in the dark was achieved through interaction with an iron specific protein

within the cellular environment. This theory was strengthened when administration of $\mathbf{Y1_{Ru}}$ only elicited a minimal response compared to the iron analogues.

Chapter 6

Iron Carbonyls Bearing a Fluorescein Linked Ligand Framework

6.1 Introduction

A fundamental requirement for the clinical development of any given CORM is the ability to impart spatial and temporal control over drug delivery. This property is of considerable importance due to the fact CO has a high affinity for heamoglobin, resulting in the formation of carboxyhaemoglobin which ultimately impairs the oxygen transport ability of the red blood cell. Moreover, larger drug doses would be required to achieve an effective concentration at the desired tissues if the CORM in question liberated CO unselectively to healthy and diseased tissues alike.

Many of the current strategies to elicit such spatial and temporal control focus on the incorporation of specific biogenic ligands onto the CORM drug sphere. The idea being that incorporation of these targeting ligands would have a high affinity for receptor sites located predominantly on diseased tissues. Of course, such a CORM would only be active at these specific tissues, and the therapeutic delivery of CO to a different site would require the incorporation of a completely different targeting ligand. Alternatively, enzyme-triggered CORMs (ET-CORMs) release CO in response to a specific enzymatic interaction. ET-CORMs, such as the acyloxybutadiene iron tricarbonyl complexes (Section 1.6.3) undergo enzymatic cleavage of the ester functionality, which facilitates

the liberation of CO.[65]

Selective drug delivery can also be managed *via* conjugation of the metal carbonyl motif with peptides or macromolecular structures including micelles and nanoparticles.[134] The first example of a CORM modified to include a peptide was reported by Schatzschneider and co-workers.[76] The $Mn(CO)_3$-core functionalised with an attached peptide (**14**, Figure 15) exhibited preferential targeting of cancer cells. This was achieved *via* the specific amino acid sequence of the attached peptide, which in this case resembled part of the sequence found in the tumour suppressor protein p53. In a later study, Schatzschneider and co-workers reported a UV-activated ruthenium photoCORM modified with peptide nucleic acid (**23**, Figure 22).[85] The attached peptide acted as a delivery vector which enhanced cellular uptake and provided a means to facilitate site-specific CO delivery.

An alternative strategy involves the application of a non-invasive external stimulus to initiate CO release. The advantage of employing photoCORMs (which release CO only in response to irradiation with light) is that delivery of CO to specific tissues can be achieved without modifying the drug sphere with specific bio-targeting ligands. Instead, the photoCORM remains thermally stable until intentionally activated *via* the application of light to the targeted tissue.

However, photodissociation of CO generally requires energy in the near-UV (350–400 nm) region to break the M−CO bond. This is a major flaw with this strategy, as near-UV irradiation causes skin damage and can increase the likelihood of developing skin cancer. Furthermore, the depth of transmission through biological tissues at this wavelength range is poor, which potentially limits the activation of the drug. Most desirable would be a CORM which is activated by longer wavelengths of light. For mammalian tissues, irradiation in the near-IR region (800–1100 nm) is most favourable due to the extensive depth of tissue penetration (up to 10 cm)[70] whilst being of lower enough energy to eliminate the risk of photodamage to the skin.

The development of such photoCORMs have largely focused on shifting the absorption maxima in a bathochromic fashion *via* extending the π-system of the ligand architecture,

or incorporating additional nitrogen donor atoms. However, two new and relatively unexplored alternative approaches have recently emerged: the incorporation of an organic dye onto the metal centre to act as a photosensitizer for CO release, and use of a dye-derivatived chromophore capable of undergoing two-photon excitations to initiate CO loss.[61]

The development of suitable photosensitizers presents a number of challenges. Firstly, the chromophore must be easily synthesised and display appropriate pharmaceutical characteristics such as biocompatibility and low toxicity. Furthermore, the light absorbing component should be relatively small in size as to not hinder cellular uptake. Most importantly, the designed compound should improve the light harvesting ability of the CORM by absorbing longer wavelengths of light.

Of course, the strategies of drug sphere modification and use of an external trigger can be combined, as was the case of the manganese photoCORM-conjugate developed by Zheng and Ford.[135] The hydrophobic photoCORM (**54**, Figure 81) was encaged in a water-soluble nanocarrier capable of up-conversion from near-IR to visible. The manganese photoCORM was shown to release approximately two equivalents of CO upon irradiation with visible (470 nm) light. Examination of the absorption maxima of the complex revealed a strong band at 400 nm, which trailed into the visible region just beyond 500 nm. Therefore, an effective up-converter would absorb near-IR light and exhibit re-emission bands which overlapped with the absorbance bands of the metal carbonyl. Following incorporation of the manganese carbonyl into the nanoparticle, CO release was achieved *via* irradiation with 980 nm light.

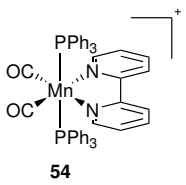

54

Figure 81: Hydrophobic manganese-based photoCORM developed by Zheng and Ford[135]

This 'combination strategy' was also explored in the development of selective cancer treatments. Traditionally, chemotherapy involves highly toxic drugs being distributed

to healthy and cancerous cells, with the selectivity for cancer cells being exclusively dependent on their increased rates of proliferation compared to healthy cells. To increase the selective toxicity of anti-cancer drugs, an attractive solution is to employ macromolecular carriers which selectively accumulate in tumour tissues due to the enhanced permeability and retention (EPR) effect. This strategy was utilized by Kunz and co-workers who coordinated *fac*-$Mn(CO)_3$ fragments to methacrylate or methacrylamide polymer backbones (**20**, Figure 19).[81] Labilisation of CO was triggered in response to irradiation at 365 nm.

The application of photosensitizers has been successful employed in the development of photosensitive nitric oxide (NO) releasing molecules. The Ford group have designed a pendant chromophore attached to an iron/sulfur/nitrosyl cluster (**55**, Figure 82)[164] which is able to sensitize NO release *via* a two-photon excitation process. This antenna is able to absorb wavelengths in the near-IR region and trigger NO loss through frequency up-conversion and the re-emission of irradiation in the visible region. More specifically, photochemical production of NO was achieved following excitation at 800 nm, which resulted frequency up-conversion and re-emission of irradiation between 480–700 nm.

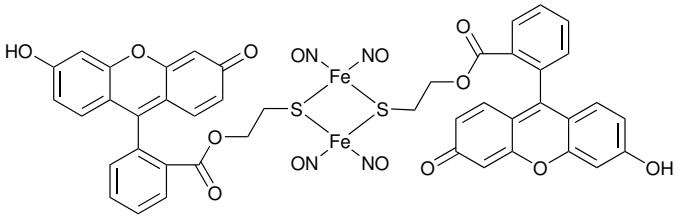

55

Figure 82: Iron/sulfur/nitrosyl cluster featuring two fluorescein moieties[164]

Taking inspiration from this work, we aimed to improve the light harvesting ability of our complexes at longer wavelengths through the incorporation of a dye-derivatized chromophore. This chapter explores two linking strategies, namely click chemistry and generation of an thiolated fluorescein chromophore.

6.2 Principle of Two-Photon Excitation

Absorption of electromagnetic radiation initiates the promotion of an electron from a lower energy state to one of higher energy. The molecule rapidly relaxes back to the lower energy state during which energy is released in the form of luminescence. The absorption and emission of light is illustrated using the Jablonski diagram (Figure 83). The lowest energy level is known as the ground state (S_0), with higher energy (or excited) states being referred to as S_1, S_2, ..., S_n. Each electronic energy level comprises a number of vibrational states (illustrated as 0, 1, 2, *etc.*), within which there are also much smaller rotational energy states (omitted for clarity).

Upon absorption of radiation and population of a higher energy vibrational state, the molecule rapidly relaxes to the lowest possible vibrational state *via* non-radiative transitions in a process known as internal conversion. This process occurs rapidly and is complete before emission starts. At this point, two types of luminescence can occur: fluorescence, the relaxation of an electron from a singlet excited state, and phosphorescence, a forbidden transition from a triplet state (T_1). The electron promoted into a singlet excited state has a spin opposite to the ground state electron. These two electrons form a pair. Florescence does not require a change in electron spin and is therefore a quantum mechanically 'allowed' transition. Contrast this to phosphorescence, where inter-system crossing from a singlet excited state to a triplet excited state involves a change in electron spin. The paired electrons in the ground and triplet states have the same orientation. Therefore phosphorescence transitions are formally 'not allowed' and consequently have much lower emission rates compared to fluorescence.

In a standard single photon absorption, the energy gap between the ground and excited state is equal to or less than the energy of the photon absorbed. Energy transfer to the excited state occurs, followed by fluorescence as the molecule relaxes back to the ground state. The energy of the fluorescence emission ($h\nu'$) will be slightly lower than the energy of the photon absorbed due to relaxation to the lowest vibrational energy level; this is known as the Stokes' shift. Two photon absorption (TPA) is the absorption

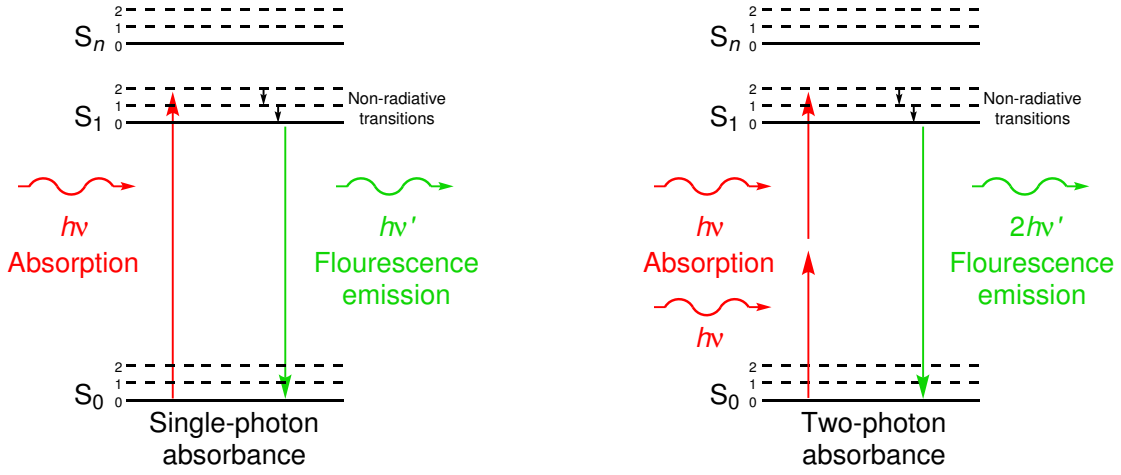

Figure 83: Jablonski diagrams depicting a single-photon absorption (left) and a two photon absorption (right)

of two photons which collectively promote an electron to an excited state. This leads to fluorescence emission with an energy of $2h\nu'$. This is a type of anti-Stokes emission, in which the fluorescence emission is significantly higher in energy compared to the energy of each photon absorbed. Inspection of the electronic absorption spectra for a two-photon excitation would display absorption bands at longer wavelengths and emission bands at shorter wavelengths. The probability of absorbing two photons simultaneous is given by the molecules cross-section (δ). This is unsurprisingly small, but can be systematically increased through increasing the π-conjugation system with donor and acceptor atoms at the centre and ends of the molecule. The most obvious advantage of TPA is the ability to access excited states using photons of only half the required energy. This is especially beneficial for drug delivery where longer wavelengths of light cause less photochemical damage.[165]

Unlike single photon absorption, which depends linearly on the intensity of the excitation radiation, the intensity of a TPA increases with the square of the intensity of the excitation light. Consequently, TPA usually employ intense and focused pulsed lasers in order to generate large irradiances. There are a number of applications which utilize TPA, including fluorescence imagining and photodynamic therapy.[166]

6.3 Linking Strategies

To maximise the efficacy with which the emitted visible light (generated *via* near-IR irradiation) activates the photoCORMs, the up-converter system should be covalently bonded to the carbonyl complex to ensure close proximity and optimal re-absorption by the active species. In critiquing the best pathway to secure the two-photon up-converter, we trialled two anchoring strategies. One of these approaches, namely click chemistry, involved attaching the fluorescein chromophore to the pyridyl ligand framework. However, prior to our attempts to develop such a chromophore system, we explored the synthesis of a simplified 'model ligand' in order to verify a synthetic route. The second route involved the synthesis of a thiolated fluorescein derivative which should mimic the coordination chemistry described in Chapter 4. Each strategy utilized 2-iodoethyl fluorescein ester (**56**, Figure 84) as the starting material. Like **56**, simplified ligand **57** was synthesised *via* a Steglich esterification using dicyclohexylcarbodiimide (DCC) and 4-*N,N*-dimethylaminopyridine (DMAP).

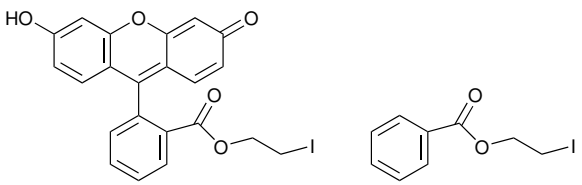

56 **57**

Figure 84: Starting materials fluorescein-2-iodoethyl ester (**56**) and benzyl-2-iodoethyl ester (**57**)

6.3.1 Click Chemistry

Click chemistry was originally defined by Sharpless in 2001, who initially developed the technique to be used in the field of drug discovery.[167] The Cu^{I}-catalysed Huisgen 1,3-dipolar cycloaddition offers a quick and simple means to connect azides and terminal alkynes.[168] This is achieve through the formation of a 1,2,3-triazole five membered ring. The procedure is highly regiospecific, exclusively forming only 1,4-substituted

products.[169,170] Moreover, high yields are typically obtained as a result of the large thermodynamic driving force attributed to the formation of C−N bonds. Reactivity between the azide and terminal alkyne usually requires a catalyst. There are exceptions in which a catalyst is not required: electron deficient alkynes are efficiently reactive enough for the reaction to proceed at ambient condition.[171] Otherwise, an Cu^{I} catalyst is used to initiate the reaction. Most commonly, the Cu^{I} catalyst is generated through the reduction of $CuSO_4 \cdot 5\,H_2O$ with sodium ascorbate. This *in situ* approach was adopted due to the reactions enhanced water and oxygen tolerance. Contrast this to addition of a copper halide catalyst in which the reaction would require the use of dried organic solvents and an inert atmospheric gas.

We initially explored the pathway of click chemistry in an attempt to isolated model ligand, **60** (Scheme 9). NMR spectroscopy revealed complete disappearance of the starting material alkyne peak at 3.06 ppm. However, because the chemical environment for each starting material remained largely unchanged throughout the reaction (excluding loss of alkyne and formation of the triazole ring which contains a single proton), little diagnostic information could be derived for the NMR spectra. Identification of this ligand was confirmed through the observed molecular ion peak at 310.1299 ($[M + H]^+$). Reaction of $Fe(CO)_4Br_2$ with **60** in dried dichloromethane overnight resulted in the formation of a dark yellow precipitate. Dissolution in acetonitrile yielded the expected ferracyclic complex bearing the click-anchored model ligand. ATR IR spectroscopy revealed new peaks at 2047, 1991, 1724 and 1621 cm^{-1}. The desired product as confirmed *via* observation of a molecular ion peak at 487.0640 ($[M - Br]^+$).

Following the successful generation of **60** and incorporation onto the iron metal centre, we attempted to replicate this chemistry in the production of **62** (Scheme 10). The 2-iodoethyl fluorescein ester starting material (**56**) was synthesised following a modified procedure reported by Ford and co-workers.[174] Reaction with sodium azide yielded the corresponding azide (**61**) *via* nucleophilic substitution.

The proton NMR profiles for **56** and **61** (shown in Figure 85) exhibit identical splitting patterns for the fluorophore fragment. The most notable change occurs in the signals for the pendant alkyl arm. The gap between these two triplet signals was significantly

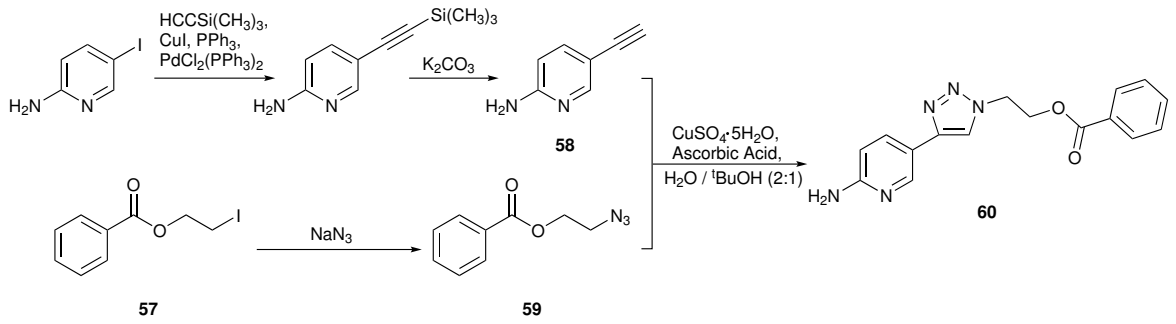

Scheme 9: Schematic for the synthesis of the desired model ligand (**60**) *via* click chemistry. Molecules **58** and **59** were generated using literature methods[172,173]

less in **61** (3.23 and 4.10 ppm) compared to **56** (2.99 and 4.24 ppm). Subjecting this azide (**61**) to click conditions in the presence of alkyne (**58**) did lead to the loss of the terminal alkyne signal. However, mass spectrometry failed to identify the molecular ion.

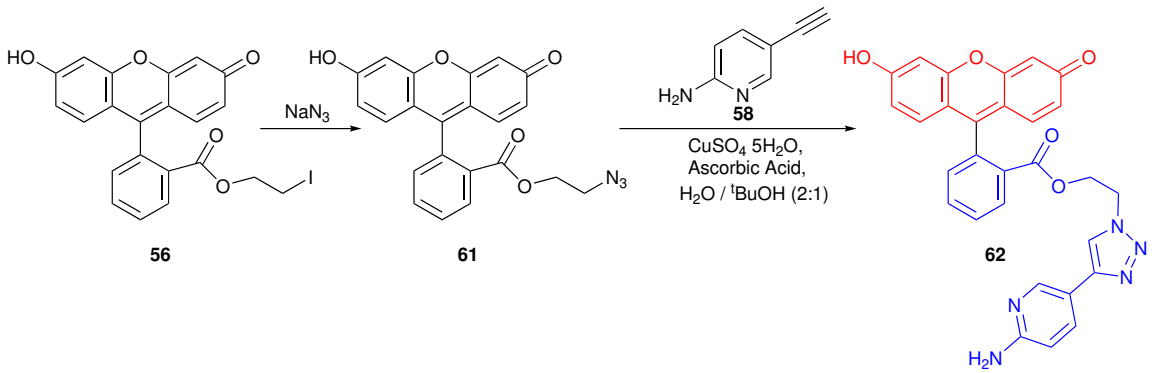

Scheme 10: Schematic for the synthesis of **62**

Proton NMR spectroscopy showed loss of signal intensities corresponding to the tricyclic fluorenyl ring (Scheme 10, shown in red) with good agreement with the rest of the molecule (shown in blue). This may suggest cleavage of the C−C bond in the fluorophore, or may be indicative of an attack on this unit, most probably at the ketyl functionality.

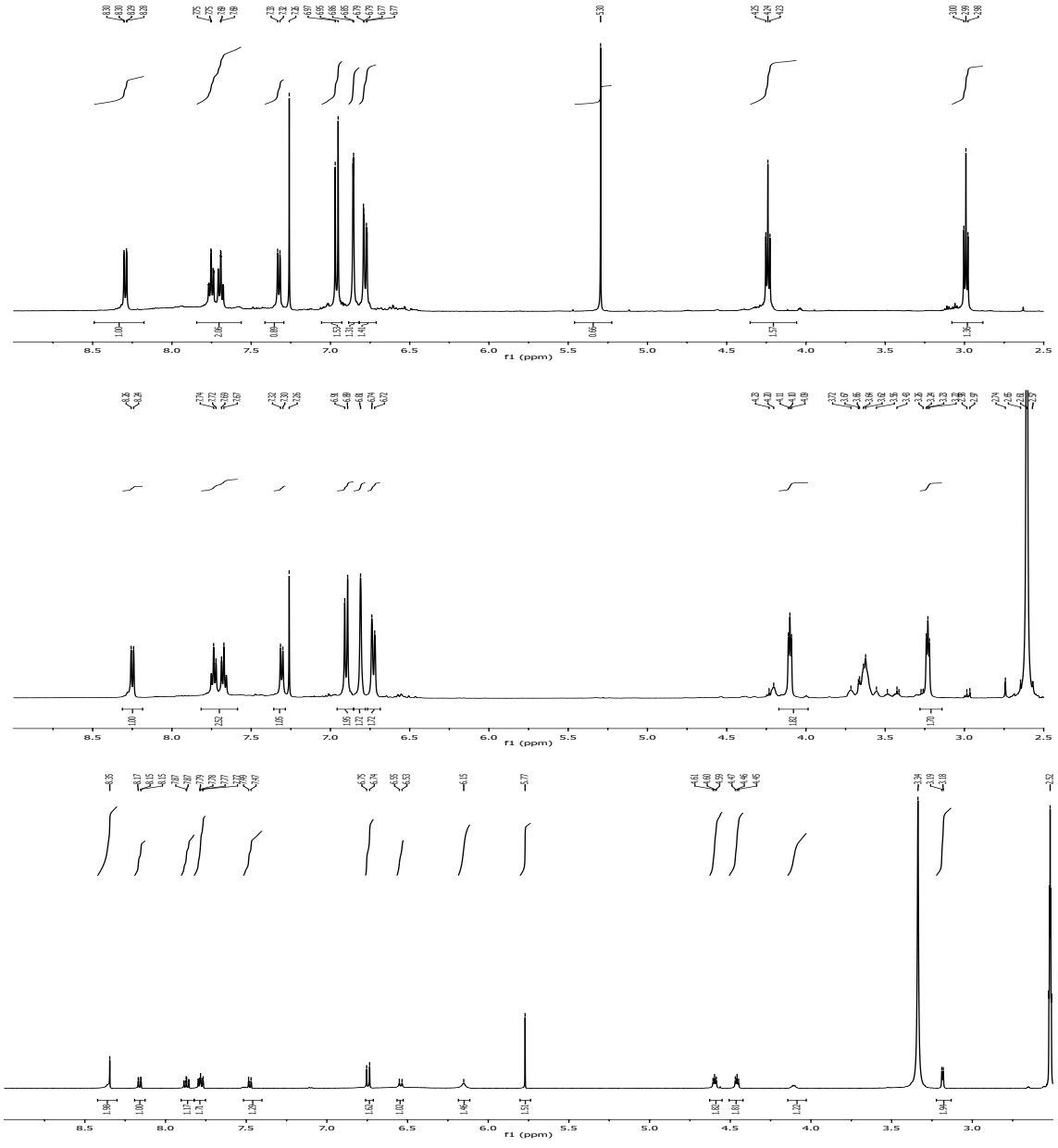

Figure 85: Above: proton NMR spectrum of **56** in $CDCl_3$. Middle: proton NMR spectrum of **61** in $CDCl_3$. Bottom: proton NMR spectrum of **62** in D_6−DMSO

6.3.2 Thiolated Fluorescein

The second strategy employed was the generation of a fluorescein thiolate which could coordinate directly to the metal centre through substitution of the halide. Although this approach would prevent the addition of the water-solubilising thioglucose ligand, the synthesis is more straightforward and easier to manufacture compare to the click chemistry. This strategy is therefore ideal to be used as a quick means to evaluate the effectiveness of attaching a two-photon up-converter to the photoCORM species.

The iodo-derivatized fluorescein precursor (**56**) was synthesised *via* a modified literature method.[174] The pendant alkyl halide arm was attached to the fluorescein molecule *via* formation of an ester linkage at the carboxylic acid functional group. The Steglich esterification reaction utilized DCC to which the carboxylic acid functionality of the fluorescein was able to attack, forming an *O*-acyl-urea intermediate. This was followed by attack of DMAP, which formed a reactive amide which could be attacked by the 2-iodoethanol alcohol group to form **56**.

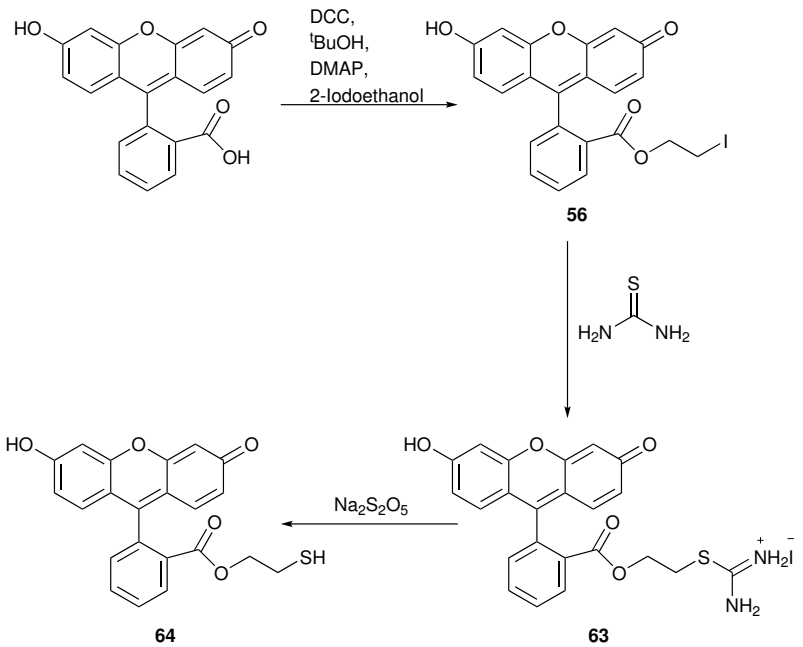

Scheme 11: Schematic for the synthesis of **64**

The alkyl halide of **56** undergoes a nucleophilic substitution reaction with thiourea to

form the alkylisothiouronium salt, **63**. Generation of the desired thiol (**64**) product can be achieved through hydrolysis of the intermediate alkylisothiouronium salt species. Typically, NaOH is employed, however, the fluorophore consists of an ester functionality, which would readily hydrolyse under such conditions. Instead, the reaction utilized the milder reducing agent, $Na_2S_2O_5$. Notably, hydrolysis required vigorous stirring and reflux conditions over 24 h. T.L.C analysis (CH_2Cl_2−CH_3OH (9 : 1)) showed complete consumption of the alkylisothiouronium salt ($R_f = 0.0$) with the formation of two closely positioned bands at $R_f = 0.60$ and 0.68. Mass spectra analysis revealed the band at $R_f = 0.68$ contained a molecular ion peak corresponding to the desired product (393.0797, $[M + H]^+$), whilst the remaining peak ($R_f = 0.60$) showed evidence of the formation of the disulphide species (783.1347, $[M + H]^+$). The UV/Vis spectrum of fluorescein changes depending on the pH and solvent. This is because fluorescein can exist in a number of protic forms, each with a different absorption spectrum.[164] Inspection of the UV/Vis spectrum of fluorescein in DMSO reveal three distinct peaks in the visible region at 435, 462 and 491 nm with significantly reduced molar extinction coefficients. As shown in Figure 86, the chromophore absorptivity remains essentially unchanged through reaction of **56** to **64**.

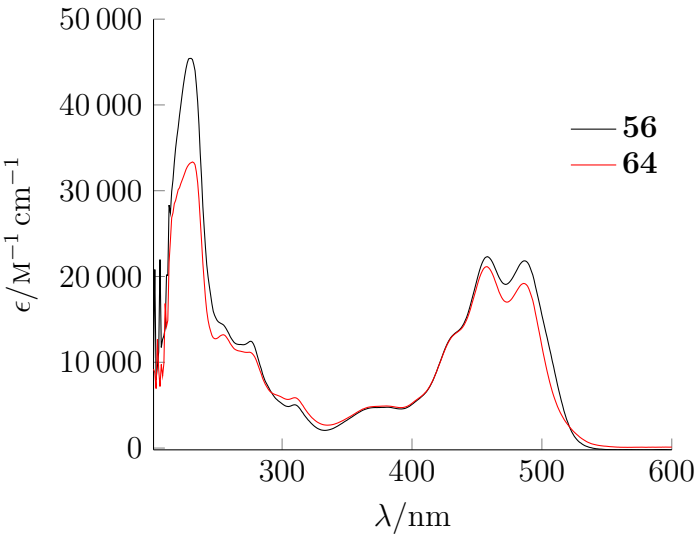

Figure 86: Electronic absorption spectra of **56** and **64** in DMSO

6.4 Summary

In summary, we explored avenues to enhance the near-IR light harvesting ability of our metallocyclic carbonyl complexes by coordinating a two-photon up-converter onto the drugs sphere. Two anchoring strategies were investigated. First, we explored click chemistry as a means of attaching a fluorescein-derivatized dye onto the pyridyl ligand architecture. Before embarking on the generation of the 'clicked' fluorescein ligand, we probed the synthetic procedure using a simplified model ligand. Generation of the model azide and linkage to the pyridyl ligand framework was successful under click conditions. Employing the same chemistry with the fluorescein-derivatized starting material successfully yielded the intermediate azide species, **61**. However, attachment to the 2-aminopyridine ligand framework *via* formation of a 1,2,3-triazole ring proved to be unsuccessful.

For our second approach, we devised to syntheses a thiolated fluorophore as an alternative method to attach the fluorescein molecule. This strategy mimics the coordination chemistry displayed in Chapter 4 and offers a readily accessible means to validate the principle behind combining a two-photon up-converter with our systems. Reaction of **56** with thiourea yielded **63**, which was subsequently hydrolysed to obtain the desired product, **64**.

Chapter 7

Conclusion and Future Directions

7.1 Conclusion

This research adds to the body of knowledge surrounding the development of novel carbonyl complexes capable of acting as therapeutic agents through the delivery of CO. Metallocyclic carbonyl complexes based on iron and ruthenium have been successfully identified and characterised. Research focused on the visible light induced CO release capabilities of the ferracyclic complexes, which were verified *via* infra-red spectroscopy and the myoglobin assay. UV/Vis spectroscopic analysis showed absorption profiles shifted towards the red with an increasing degree of conjugation in the ligand framework. Not only this, incorporation of a nitrogen donor group onto the architecture further enhanced the light sensitivity of the complex.

Reaction of these first generation carbonyls with thioglucose yielded dimeric species with significantly enhanced water solubility. Quantification of CO release revealed a dramatic change in CO release behaviour between the monomeric and dimeric species, including a change in mechanism. Indeed, $\mathbf{Y1_{Fe}}$ and $\mathbf{Y2_{Fe}}$ exhibited steady release of two equivalence of CO over 120 min. Complexes $\mathbf{D1_{Fe}}$ and $\mathbf{D2_{Fe}}$, however, displayed rapid loss of the first equivalent of CO, followed by much slower liberation of a second equivalent. Notably, $\mathbf{D1_{Fe}}$ and $\mathbf{D2_{Fe}}$ only liberate half of the available metal bound carbonyl ligands present. DFT calculations attribute this to insufficient HOMO–LUMO contribution consequence of the dimeric geometry. The heightened photosensitivity of

the dimeric species is perhaps most exemplified when comparing $\mathbf{D5_{Ru}}$ to monomeric analogue, $\mathbf{Y5_{Ru}}$, where the former displays visible light activated CO release and the latter does not.

The ability of these complexes to act as therapeutic agents was accessed. LPS-induced inflammation of THP-1 cells was alleviated following addition of $\mathbf{Y1_{Fe}}$ and $\mathbf{Y2_{Fe}}$, with the most observable inhibition of TNF-α exhibited in cells kept in the dark. This surprising finding contradicted the photoCORM activities verified using the myoglobin assay, and we speculate the anti-inflammation response is a consequence of CO loss initiated *in vitro*. Complexes $\mathbf{D1_{Fe}}$ and $\mathbf{D2_{Fe}}$ produced minimal anti-inflammatory influence, possibly due to poor cellular uptake. The distinct lack of bioactivity imparted by $\mathbf{Y1_{Ru}}$ suggest the intracellular CO loss is triggered *via* interaction with an iron specific enzyme or cellular machinery.

7.2 Future Avenues

Further to our demonstrations of *in vitro* anti-inflammatory behaviour, investigations into additional inflammatory markers should be carried out. This includes monitoring any changes in the immune responses elicited by pro-inflammatory cytokines IL-1 and IL-6 following CORM administration, as well as examining any up-regulatory activity of anti-inflammatory cytokines such as IL-10. Also, future *in vitro* investigations should allow extended incubation times to probe the cellular uptake capabilities of $\mathbf{D1_{Fe}}$ and $\mathbf{D2_{Fe}}$. Synthetic efforts should be made to isolate a monomeric species featuring a bulky thio-saccharide derivative. Such a species should display sufficient water solubility whilst being small enough to efficiently cross the cellular membrane.

Further to this, in order to verify that the achieved anti-inflammatory responses operate *via* a CO signalling pathway, the following investigatory efforts should be made. First, cell lines should be administrated with gaseous CO and a direct comparison in activity made. Indeed, there have been many studies which establish the therapeutic benefit of gaseous CO on inflammation. However, in the contexts of this research, this direct comparison would authenticate the bioactivities of our complexes as CORMs, rather

than eliciting activity independent of CO. This can be combined with investigations into the levels of CO produced *in vitro* following CORM administration. This can be achieved *via* the detection method reported by Tschugguel and co-workers, in which CO present in the cell supernatant was reacted with haemoglobin. The amount of carboxyhaemoglobin produced can be determined by spectrophotometric analysis, which in turn provides an accurate quantification of the concentration of CO.[175] This method adopts the same detection principles used in the myogobin assay, except it allows for an exact determination CO generated *in vitro*. Alternatively, administration of a suitable '*i*CORM' would allow the therapeutic response to be attributed to CO.

There have been numerous studies implicating the involvement of various CO target sites and signalling pathways. It would therefore be beneficial to inspect the extent of activity in the presence of specific pathway activators or inhibitors. As summarised in Figure 2, there is convincing evidence that CO mediates its therapeutic effects *via* the soluble gyanylyl cyclase (sGC) system and involvement with MAPK proteins (not to mention others). In order to investigate whether the anti-inflammatory effects observed operate through either of these pathways, *in vitro* investigations exclusively modulating each pathway should be carried out. For example, to ascertain any involvement of sGC, the scope of TNF-α inhibition may be markedly increased in the presence of sGC activator, YC-1 (**1**, Figure 1) or notably decreased in the presence of sGC inhibitor, ODQ.

Further research will be required to determine the exact *in vitro* activation mechanism which facilitated the anti-inflammatory response from the monomeric ferracyclic complexes kept in the dark. As the corresponding ruthenium carbonyl produced significantly lower activity, we speculate intracellular CO loss was initiated *via* interaction with an iron-specific protein. Motterlini and co-workers mention the unusual case of $[Fe(bpy)(SPh)_2(CO)_2]$ which has been shown to cause vasodilation despite failing to generate MbCO in the presence of myoglobin. This is suggestive of an intracellular CO release mechanism initiated *via* complex involvement with biological machinery.[26] However, one must be careful when assigning this therapeutic effect to the actions of CO. Indeed, bipyridine (including derivatives) has also been shown to restore vascular disorders.[176,177] Unfortunately, no further details on the study of $[Fe(bpy)(SPh)_2(CO)_2]$

as a therapeutic agent have been given.

Despite the impressive ability of $\mathbf{Y1_{Fe}}$ and $\mathbf{Y2_{Fe}}$ to alleviate inflammation, the selective activation of these complexes is lost *in vitro*. The development of CORMs which facilitate spatial and temporal control over CO delivery is vitally important. Modification of our ruthenium complexes with the light-sensitizing chromophores discussed in Chapter 6 could provide an avenue to develop light directed CO release.

Chapter 8

Experimental

8.1 General

All reactions were conducted under a dry nitrogen atmosphere using standard Schlenk techniques. Starting materials were purchased from Aldrich or Alfa Aesar and were used without further purification. All glassware and solvents were pre-dried and degassed prior to use. The appropriate drying agents were used for solvent drying: CH_2Cl_2 (CaH_2), tetrahydrofuran ($Na/(C_6H_5)_2CO$) and acetonitrile (CaH_2). FT-IR spectra were recorded using a Perkin-Elmer SpectrumBX instrument. NMR spectra were recorded on a Bruker AvanceIII 500 operating at 500 MHz, at ambient temperature (*ca* 21 °C). Chemical shifts are given in parts per million (δ) and quoted relative to the residual solvent peak. UV-visible spectra were recorded using an Agilent Technologies Cary 60 in disposable 1 cm plastic cuvettes. Elemental analysis was carried out at London Metropolitan University. Mass Spectrometry was carried out at the National Mass Spectrometry Facility at the Swansea University. The preparations of $Fe(CO)_4Br_2$,[108] $Ru(CO)_4Br_2$,[130,131] 1-thio-β-D-glucose,[138] **58**[172] and **59**[173] were carried out following literature procedures.

8.2 Synthesis

8.2.1 Complex $\mathbf{Y1_{Fe}}$

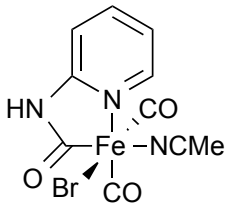

The synthesis was carried out using a modified procedure to that reported in the literature.[108] To a solution of $[Fe(CO)_4Br_2]$ (0.78 g, 2.36 mmol) in CH_2Cl_2 (60 mL) was added 2-aminopyridine (0.46 g, 4.9 mmol). The solution was left to react for 2 h. Gas was evolved and a yellow precipitate formed over time. Once precipitation was complete, the supernatant was removed *via* decantation. The yellow product was recrystallized from acetonitrile affording brown crystals (0.46 g, 51 %). M.p. 108 °C. Found C 36.37, H 2.67, N 14.16 %; $C_9H_8BrFeN_3O_3 \cdot C_2H_2N$ requires C 36.49, H 2.81, N 14.14 %. UV/Vis (DMSO) λ_{max} 277 (1.65×10^4) nm ($M^{-1}\,cm^{-1}$). ν_{max} (MeCN) 2051, 1997, 1987, 1668, 1621 cm^{-1}. m/z (Orbitrap) 375.9 $[M + Na]^+$.

8.2.2 Complex $\mathbf{Y2_{Fe}}$

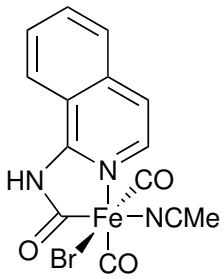

$[Fe(CO)_4Br_2]$ (0.29 g, 0.77 mmol) was dissolved in CH_2Cl_2 (30 mL) and cooled to −40 °C. 1-Aminoisoquinoline (0.19 g, 1.82 mmol) in CH_2Cl_2 (20 mL) was added drop-wise (protected from light), and the resulting solution allowed to warm to −10 °C. The solution was allowed to react at room temperature for a further hour. The solution was decanted to leave a yellow precipitate. Recrystallisation from acetonitrile (25 mL) yielded $[FeBr(C_{10}H_7N_2O)(CO)_2(MeCN)]$ (0.37 g, 48 %). X-ray quality crytals were obtained from the same solvent. Decomposes at 155 °C. Found C 41.40, H 2.34, N 10.16 %; $C_{14}H_{10}BrFeN_3O_3$ requires C 41.62, H 2.49, N 10.40 %. UV/Vis (DMSO) λ_{max} 283 (1.68×10^4), 349 (5.59×10^3) nm ($M^{-1}\,cm^{-1}$). ν_{max} (MeCN) 2053, 1999, 1989, 1662, 1613 cm^{-1}.

8.2.3 Complex $\mathbf{X3_{Fe}}$

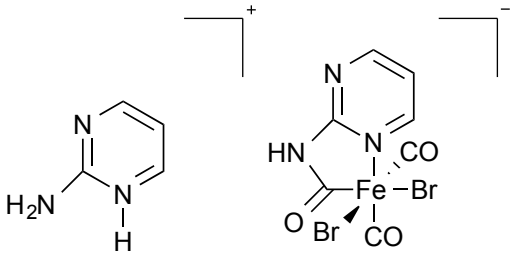

To a solution of $[Fe(CO)_4Br_2]$ (100 mg, 0.28 mmol) in CH_2Cl_2 (50 mL) was added 2-aminopyrimidine (26 mg, 0.27 mmol). After 3 h, an orange/yellow precipitate forms, which was collected *via* decantation of the supernatant. The yellow product was recrystallized from acetonitrile affording brown crystals (0.17 g, 41 %). Found C 27.19,

H 2.00, N 17.30 %; $C_{11}H_9Br_2FeN_6O_3$ requires C 27.02, H 1.86, N 17.19. UV/Vis (DMSO) λ_{max} 297 (1.35×10^4) nm ($M^{-1}\,cm^{-1}$). ν_{max} (CH_2Cl_2) 2058, 2009, 1989, 1661, 1635, 1625 cm^{-1}.

8.2.4 Complex $X4_{Fe}$

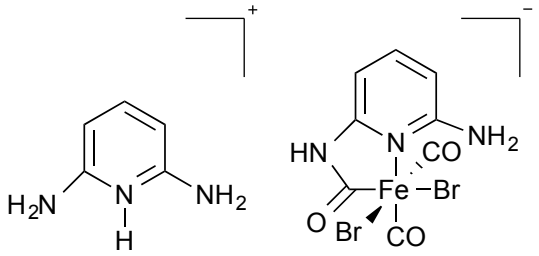

$[Fe(CO)_4Br_2]$ (0.12 g, 0.31 mmol) was dissolved in CH_2Cl_2 (30 mL) with the exclusion of light. Upon cooling to −40 °C, 2,6-diaminopyridine (74 mg, 0.67 mmol) dissolved in CH_2Cl_2 (20 mL) was added drop-wise. The reaction was allowed to warm naturally to room temperature. After 2 h a yellow precipitate formed, the supernatant was decanted and the solid dried under vacuum (0.17 g, 55 %). UV/Vis (DMSO) λ_{max} 341 (2.52×10^4), 259 (2.68×10^4) nm ($M^{-1}\,cm^{-1}$). ν_{max} (ATR) 2036, 1972, 1632, 1552 cm^{-1}.

8.2.5 Complex $Y1_{Ru}$

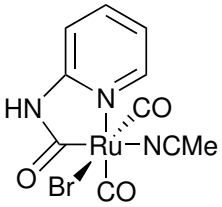

To a solution of $[Ru(CO)_4Br_2]$ (49.7 mg, 0.13 mmol) in CH_2Cl_2 (10 mL) was added 2-aminopyridine (27.4 mg, 0.29 mmol). Gas was evolved and a white precipitate formed almost immediately. Once precipitation was complete, the supernatant was removed *via* decantation. The white product was redissolved in acetonitrile. Addition of

one equivalent of $AgPF_6$ under stirring resulted in the formation of AgBr precipitation. Filtration and cooling of the solution yields colourless X-ray quality crystals of $[RuBr(C_6H_5N_2O)(CO)_2(MeCN)]$ (35.7 mg, 49 %). M.p. 167 °C. Found C 30.23, H 1.99, N 10.44 %; $C_{10}H_8BrN_3O_3Ru$ requires C 30.09, H 2.02, N 10.53 %. UV/Vis (DMSO) λ_{max} 298 (6.74×10^3), 262 (1.26×10^4) nm ($M^{-1}\,cm^{-1}$). ν_{max} (THF) 2055, 1987, 1672, 1621 cm^{-1}. m/z (Orbitrap) 319.9 [M^+].

8.2.6 Complex $Y2_{Ru}$

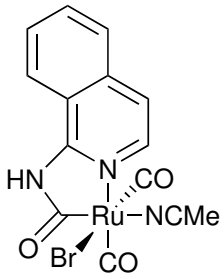

A solution of $[Ru(CO)_4Br_2]$ (53.8 mg, 0.14 mmol) and 1-aminoisoquinoline (48.0 mg, 0.33 mmol, 2 eq) in CH_2Cl_2 (10 mL) was stirred for 30 min, after which time a pale precipitate appeared. The supernatant was decanted and the precipitate dried under vacuum. Addition of MeCN (12 mL) and one equivalent of $AgPF_6$, followed by separation *via* filtration and recrystallisation yielded $[RuBr(C_{10}H_7N_2O)(CO)_2(MeCN)]$ as colourless needles (37.3 mg, 58 %). Decomposes 202 °C. Found C 37.25, H 2.12, N 9.27 %; $C_{14}H_{10}BrN_3O_3Ru$ requires C 37.45, H 2.24, N 9.35 %. UV/Vis (DMSO) λ_{max} 268 (1.87×10^4), 341 (9.85×10^3) nm ($M^{-1}\,cm^{-1}$). ν_{max} (THF) 2046, 1990, 1967, 1668, 1649, 1618 cm^{-1}. m/z (Orbitrap) 369.9 [M^+].

8.2.7 Complex $Y4_{Ru}$

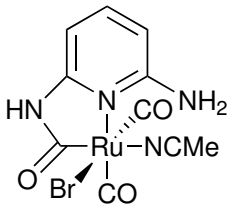

$[Ru(CO)_4Br_2]$ (77.7 mg, 0.21 mmol) was dissolved in CH_2Cl_2 (10 mmol) to which 2,6-diaminopyridine (51.0 mg, 0.47 mmol, 2 eq) was added. After 30 min a yellow precipitate formed. The solution was decanted and the precipitate dried under vacuum. The precipitate was redissolved in MeCN (10 mL) containing one equivalent of $AgPF_6$. Following filtration, recrystallisation yielded colourless needle-like crystals of $[RuBr(C_6H_7N_3O)(CO)_2(MeCN)]$ (44.0 mg, 52 %). Decomposes at 185 °C. Found C 28.91, H 2.28, N 13.57 %; $C_{10}H_9BrN_4O_3Ru$ requires C 29.00, H 2.19, N 13.53 %. UV/Vis (DMSO) λ_{max} 264 (1.33×10^4), 343 (1.54×10^4) nm ($M^{-1}\,cm^{-1}$). ν_{max} (MeCN) 2065, 2002, 1656, 1644, 1617 cm^{-1}. m/z (Orbitrap) 334.9 $[M^+]$.

8.2.8 1,3-Diaminoquinoline (49)

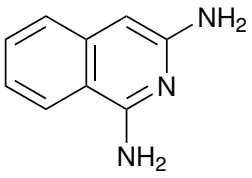

This synthesis was carried out using a literature protocol.[132] A solution of *o*-cyanobenzyl chloride (8.23 g, 57.9 mmol) in deoxygenated formamide (80 mL) was heated to 55 °C. Upon cooling to 15 °C, an ice-cold solution of sodamide (6.2 g, 159 mol) in deoxygenated formamide (100 mL) was added in portions of 10 mL with stirring under nitrogen. After 2 h a yellow precipitate was separated. Distilled water (300 mL) was added to the reaction filtrate and allowed to stir 1.5 h. An orange solid was separated from the filtrate, which was made turbid by another portion of water (300 mL) following 2 h

of stirring. A dark orange solid was separated and dried. This orange solid (1.84 g, 9.83 mmol, 17 %) was dissolved in ethanol (90 mL) and heated under reflux with sodium hydroxide (2 M, 360 mL) for 1 h. Evaporation resulted in the precipitation of a yellow powder which was washed with ice-cold water. 1,3-Diaminoquinoline (1.03 g, 11 %) was isolated as a yellow solid. M.p. 173–175 °C. Found C 67.73, H 5.77, N 26.32 %; $C_9H_9N_3$ requires C 67.90, H 5.70, N 26.40 %. UV/Vis (DMSO) λ_{max} 260 (7.81×10^3), 308 (1.01×10^4), 390 (4.33×10^3) nm ($M^{-1}\,cm^{-1}$). ^{1}H NMR (500 MHz, DMSO) δ: 5.26 (2H, s), 5.84 (1H, s), 6.44 (2H, s), 6.91 (1H, ddd, $J = 1.4, 6.6, 8.2$ Hz), 7.24 (1H, m), 7.28 (1H, m), 7.89 (1H, d, $J = 8.5$ Hz). ^{13}C NMR (126 MHz, DMSO) δ: 87.00, 111.38, 119.32, 123.87, 124.46, 129.46, 140.50, 155.01, 156.97. m/z (Orbitrap) 160.0867 [M^+]

8.2.9 Complex $Y5_{Ru}$

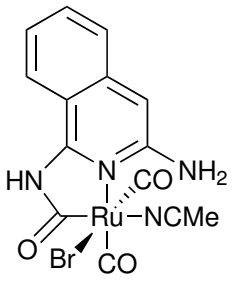

A solution of $[Ru(CO)_4Br_2]$ (0.09 g, 0.24 mmol) was dissolved in CH_2Cl_2 (20 mL) and 1,3-diaminoquinoline (86 mg, 0.54 mmol) was added. After stirring for 1.5 h a white precipitate appear. The supernatant was removed and the precipitate dried under vacuum. The precipitate was redissolved in MeCN (10 mL) containing one equivalent of $AgPF_6$. The resultant AgBr was filtered off and the remaining solvent removed under vacuum to product a yellow crystalline solid (39 mg, 35 %). M.p. 194 °C. Found C 36.04, H 2.23, N 11.94 %; $C_{14}H_{11}BrN_4O_3Ru$ requires C 36.22, H 2.39, N 12.07 %. UV/Vis (DMSO) λ_{max} 258 (1.60×10^4), 308 (1.48×10^4), 401 (4.58×10^3) nm ($M^{-1}\,cm^{-1}$). ν_{max} (MeCN) 2066, 2001, 1666, 1642 and 1628 cm^{-1}. m/z (Orbitrap) 486.8938 $[M + Na]^+$

8.2.10 Complex $\mathbf{D1_{Fe}}$

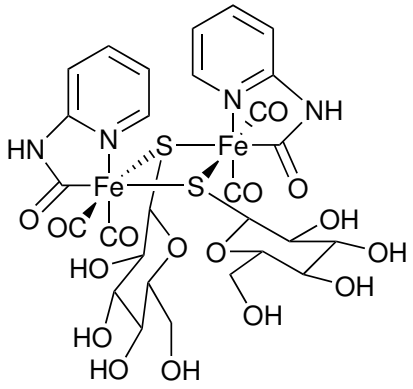

To a solution of $\mathbf{Y1_{Fe}}$ (37.2 mg, 0.11 mmol) in MeOH (10 mL) was added one equivalent of 1-thio-β-D-glucose from a stock solution of known concentration. The reaction was allowed to stir for 1 h. The solvent was removed under vacuum yielding a yellow solid (48.0 mg, 51 %). M.p. 95 °C. Found C 38.87, H 3.68, N 6.37 %; $C_{28}H_{32}Fe_2N_4O_{16}S_2$ requires C 39.27, H 3.77, N 6.54 %. UV/Vis (DMSO) λ_{max} 301 (4.12×10^4) nm ($M^{-1}\,cm^{-1}$). ν_{max} (MeOH) 2046, 2025, 1977, 1674 and 1622 cm^{-1}. m/z (Orbitrap) 857.0 [M^+].

8.2.11 Complex $\mathbf{D2_{Fe}}$

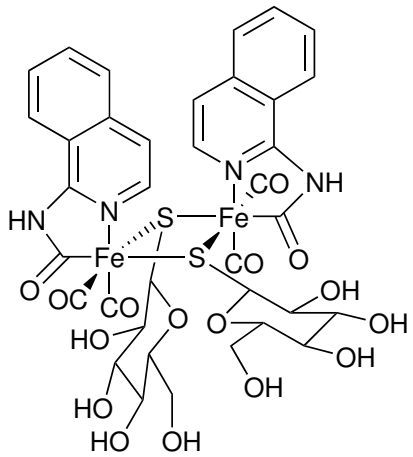

A solution of $\mathbf{Y2_{Fe}}$ (5.0 mg, 0.0124 mmol) was dissolved in MeOH (10 mL) and one equivalent of 1-thio-β-D-glucose was added from a stock solution of known concentration.

The reaction was allowed to stir for 1 h. The product was recrystallized from methanol affording yellow prisms (3.7 mg, 31 %). M.p. 136 °C. UV/Vis (DMSO) λ_{max} 280 (3.23×10^4), 289 (3.24×10^4), 335 (1.94×10^4) nm ($M^{-1}\,cm^{-1}$). ν_{max} (MeOH) 2048, 2025, 1980, 1675, 1622 cm^{-1}. m/z (Orbitrap) 979.0 [M^+]

8.2.12 Complex $\mathbf{D1_{Ru}}$

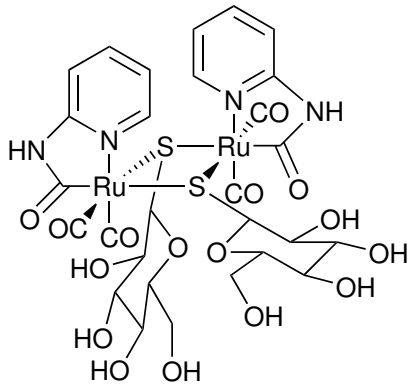

Complex $\mathbf{Y1_{Ru}}$ (11.7 mg, 0.03 mmol) was dissolved in methanol (10 mL) and one equivalent of 1-thio-β-D-glucose was added from a stock solution. The reaction was allowed to stir at room temperature for 1.5 h, afterwhich time the solvent was removed under vacuum. The desired product was obtained as a white powder (10.9 mg, 40 %). M.p. 194 °C. UV/Vis (DMSO) λ_{max} 261 (1.38×10^4) nm ($M^{-1}\,cm^{-1}$). ν_{max} (MeOH) 2061, 1987, 1675, 1622 cm^{-1}. m/z (Orbitrap) 948.9 [M^+]

8.2.13 Complex $\mathbf{D2_{Ru}}$

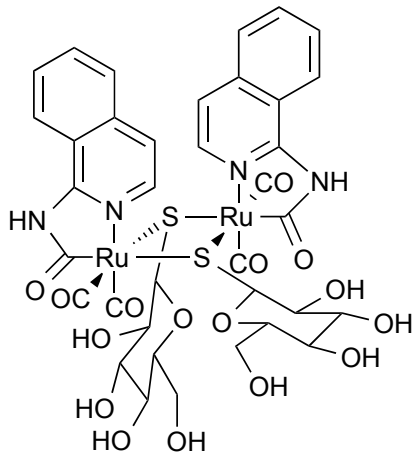

A solution of $\mathbf{Y2_{Ru}}$ (3.81 mg, 0.027 mmol) in methanol (5 mL) containing one equivalent of 1-thio-β-D-glucose was stirred at room temperature for 1.5 h. Slow evaporation of the solvent produced colourless X-ray quality crystals (2.20 mg, 26 %). Found C 40.92, H 3.33, N 5.29 %; $C_{36}H_{36}N_4O_{16}Ru_2S_2$ requires C 41.3, H 3.47, N 5.35 %. UV/Vis (DMSO) λ_{max} 259 (3.15×10^4), 338 (1.10×10^4) nm ($M^{-1}\,cm^{-1}$). ν_{max} (MeOH) 2059, 2042, 1981, 1658, 1630, 1595 cm^{-1}. m/z (Orbitrap) 1048.9 [M^+]

8.2.14 Complex $\mathbf{D4_{Ru}}$

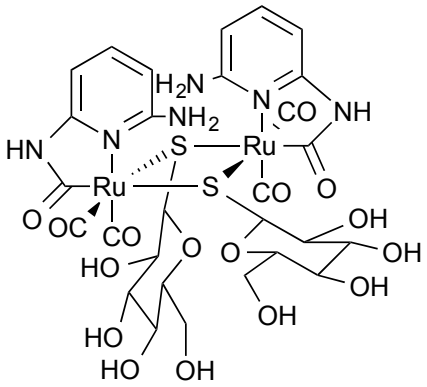

To a solution of $[Ru(CO)_4Br_2]$ (0.11 g, 0.29 mmol) dissolved in CH_2Cl_2 (10 mL) was added 2,6-diaminopyridine (60.0 mg, 0.6 mmol) drop-wise at −40 °C. The solution was left to react until it reached room temperature. Once a white precipitation was complete,

the supernatant was removed *via* decantation. The white precipitation was dissolved in methanol (10 mL) and one equivalent of 1-thio-β-D-glucose was added from a stock solution of known concentration. The solution was allowed to react for 1.5 h, afterwhich the solvent was removed to give a white solid (50 mg, 18 %). Found C 34.18, H 3.31, N 8.43 %; $C_{29}H_{34}N_5O_{16}Ru_2S_2$ requires C 34.43, H 3.51, N 8.60 %. UV/Vis (DMSO) λ_{max} 258 (1.63×10^4), 342 (1.82×10^4) nm ($M^{-1}\,cm^{-1}$). ν_{max} (MeOH) 2060, 1993, 1672, 1635, 1622 cm^{-1}. m/z (Orbitrap) 977.9 $[M^+]$

8.2.15 Complex $D5_{Ru}$

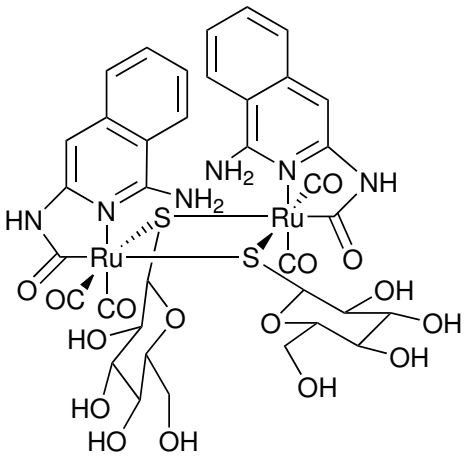

Complex $\mathbf{Y5_{Ru}}$ (12.05 mg, 0.026 mmol) in methanol (10 mL) containing one equivalent of 1-thio-β-D-glucose was stirred for 1.5 h, after which the solvent was removed under vacuum to produce an yellow solid (17 mg, 61 %). Found C 39.14, H 3.46, N 7.56 %; $C_{36}H_{38}N_6O_{16}Ru_2S_2$ requires C 40.15, H 3.56, N 7.8 %. UV/Vis (DMSO) λ_{max} 258 (3.16×10^4), 314 (2.62×10^4), 388 (6.97×10^3) nm ($M^{-1}\,cm^{-1}$). ν_{max} (MeOH) 2060, 1991, 1635 and 1622 cm^{-1}. m/z (Orbitrap) 1077.9 $[M + H]^+$

8.2.16 2-Iodoethylbenzoate (57)

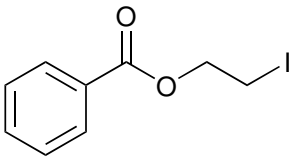

Benzoic acid (1.01 g, 8.27 mmol) was dissolved in dry THF (100 mL) under an inert atmosphere. 1-Hydroxybenztriazole (1.11 g, 8.19 mmol) and 4-(dimethylamino)pyridine (0.11 g, 0.88 mmol) were added. The solution was cooled in an ice bath to 0 °C, followed by slow addition of 1,3-dicyclocarbodiimide (1.68 g, 8.14 mmol). After stirring for 10 min 2-iodoethanol (0.6 mL, 7.7 mmol) was added drop-wise. The reaction was stirred in an ice bath under an inert atmosphere for 3 h, after which the ice bath was removed and the solution allowed to stir for 16 h. The solvent was removed at reduced pressure. The resulting residue was purified (1.74 g, 76 %) *via* column chromatography silica gel using EtOAc−Hex (1 : 9) as the elutent mixture. The desired product gave a band at R_f = 0.78. ^{1}H NMR (500 MHz, $CDCl_3$) δ: 3.43 (2H, t, J = 6.8 Hz, CH_2I), 4.57 (2H, t, J = 6.8 Hz, OCH_2), 7.45 (2H, m, *m*-H), 7.58 (1H, tt, J = 7.4, 1.3 Hz, *p*-H), 8.08 (2H, dd, 1H, tt, J = 8.5, 1.26 Hz, *o*-H).

8.2.17 2-[4-(6-Aminopyridin-3-yl)-1*H*-1,2,3-triazol-1-yl]ethyl benzoate (60)

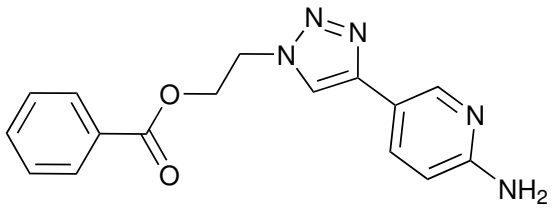

A mixture of 2-amino-5-ethynylpyridine (0.26 g, 2.20 mmol) and 2-azidoethyl benzoate (0.43 g, 2.25 mmol) was dissolved in *tert*-butanol (5 mL) and H_2O (2.5 mL). $CuSO_4 \cdot 5\,H_2O$ (5.5 mg, 0.02 mmol, 1 mol %) and L-ascorbic acid (2.0 mg, 0.11 mmol, 5 mol %)

were added. The reaction was stirred overnight under N_2. T.L.C. (hexane−EtOAc (4 : 1)) confirmed product formation ($R_f = 0.15$). The mixture was extracted with CH_2Cl_2 (3 × 10 mL), the combined organic phases washed with H_2O (3 × 10 mL) and dried over $MgSO_4$. The desired product was isolated as a residue after evaporation of the solvent *in vacuo* (0.13 g, 20 %). ν_{max} (CH_2Cl_2) 1016, 1026, 1072, 1098, 1113, 1266, 1721, 2105, 2338, 2361, 2856, 2928, 2963 and 3403 cm^{-1}. ^1H NMR (500 MHz, $CDCl_3$) δ: 3.54 (2H, t, $J = 5.0$ Hz, CH_2), 4.43 (2H, t, $J = 5.0$ Hz, CH_2), 6.52 (1H, br s, NH_2), 7.32–7.37 (2H, m), 7.45–7.49 (2H, m), 7.70 (1H, s), 7.81 (1H, d, $J = 8.44$ Hz), 7.88 (1H, d, $J = 7.74$ Hz), 7.96 (2H, d, $J = 7.78$ Hz) m/z (Orbitrap) 310.1 $[M + H]^+$.

8.2.18 2-Iodoethyl fluorescein (56)

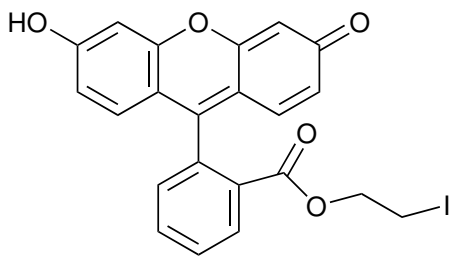

The synthesis was carried out using a modified procedure to that reported in the literature.[174] Fluorescein (0.676 g, 2.0 mmol) was dissolved in dry THF (50 mL) under an inert atmosphere. 1-Hydroxybenztriazole (0.289 g, 2.0 mmol) and 4-(dimethylamino)pyridine (31 mg, 0.22 mmol) were added. The solution was cooled in an ice bath to 0 °C, followed by slow addition of 1,3-dicyclocarbodiimide (0.383 g, 2.0 mmol). After stirring for 10 min 2-iodoethanol (0.2 mL, 2 mmol) was added drop-wise. The reaction was stirred in an ice bath under an inert atmosphere for 3 h, after which the ice bath was removed and the solution allowed to stir overnight. The solvent was removed at reduced pressure and the resulting solid taken up in ice-cold chloroform and filtered. After removal of the solvent *in vacuo*, the product was purified *via* column chromatography silica gel using CH_2Cl_2−CH_3OH (9 : 1) as the elutent mixture. The desired product gave an orange band ($R_f = 0.4$). The desired product was collected as a red crystalline solid (0.279 g, 28 %). M.p. 167 °C. Found C 54.41, H 3.12 %; $C_{22}H_{15}IO_5$ requires C 54.34, H

3.11 %. UV/Vis (DMSO) λ_{max} 231 (4.53×10^4), 460 (2.21×10^4), 489 (2.16×10^4) nm ($\text{M}^{-1}\,\text{cm}^{-1}$). ^{1}H NMR (500 MHz, CD_3OD) δ: 3.13 (2H, t, $J = 6.1$ Hz, CH_2), 4.28 (2H, t, $J = 6.1$ Hz, CH_2), 6.72 (2H, dd, $J = 9.3$, 2.2 Hz), 6.78–6.75 (2H, m), 7.05 (2H, d, $J = 9.3$ Hz), 7.45 (1H, dd, $J = 7.6$, 1.3 Hz), 7.81 (1H, td, $J = 7.7$, 1.3 Hz), 7.88 (1H, td, $J = 7.5$, 1.4 Hz), 8.36 (1H, dd, $J = 7.9$, 1.4 Hz). ^{13}C NMR (126 MHz, MeOD) δ: −1.44, 65.70, 102.96, 115.16, 129.87, 130.49, 130.64, 131.04, 132.85, 134.05, 155.14, 157.81, 164.76. m/z (Orbitrap) 487.003 [M^+].

8.2.19 2-Azidoethyl fluorescein (61)

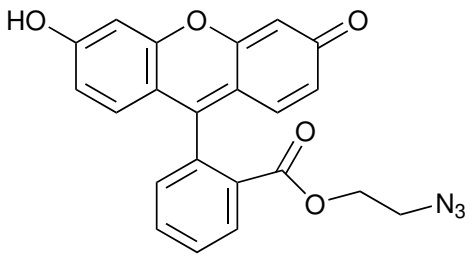

To a solution of **56** (0.27 g, 0.56 mmol) dissolved in DMSO (3.5 mL) was added one equivalent of NaN_3 (43 mg, 0.66 mmol) dissolved in DMSO (0.5 M, 1.5 mL). The mixture was allowed to stir for 16 h. The reaction was quenched by addition of distilled water (5 mL). The aqueous phase was separated and washed with CH_2Cl_2 (2 ×5 mL). The combined organic phases were washed with brine and dried over $MgSO_4$. The desired product was isolated following filtration and solvent removal *in vacuo* to give an orange residue (0.23 g, 100 %). ^{1}H NMR (500 MHz, CD_3OD) δ: 3.24 (2H, t, $J = 5.0$ Hz, CH_2), 4.11 (2H, t, $J = 5.0$ Hz, CH_2), 6.74 (2H, dd, $J = 9.2$, 2.1 Hz), 6.82 (2H, s), 6.91 (2H, d, $J = 9.1$ Hz), 7.35–7.30 (1H, m), 7.68 (1H, td, $J = 7.7$, 1.3 Hz), 7.75 (1H, td, $J = 7.5$, 1.4 Hz), 8.26 (1H, dd, $J = 7.9$, 1.3 Hz). ^{13}C NMR (126 MHz, $CDCl_3$) δ: 0.95, 40.87, 49.31, 63.52, 103.79, 114.98, 121.98, 129.65, 129.77, 130.11, 130.46, 131.24, 132.86, 134.56, 153.61, 157.41, 164.81.

8.2.20 2-Thiouroniumethyl fluorescein iodide (63)

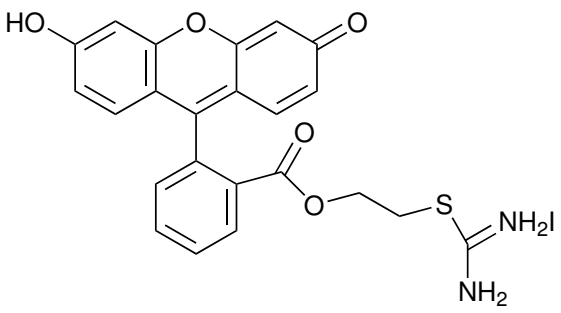

Compound **56** (0.129 g, 0.27 mmol) and thiourea (29.65 mg, 0.39 mmol, 1.5 Eq) were dissolved in methanol (5 mL) and heated under reflux. After 24 h, T.L.C. (CH_2Cl_2−MeOH (9 : 1)) showed a majority product at $R_f = 0.0$, with some starting material remaining ($R_f = 0.4$). The solvent was removed at reduced pressure. The product was isolated by washing with Et_2O, which dissolved the starting material but not the product, which was isolated as a red solid (0.103 g, 70 %). M.p. 198–200 °C. Found C 48.72, H 3.41, N 5.07 %; $C_{22}H_{15}IO_5$ requires C 49.12, H 3.41, N 4.98 %. UV/Vis (DMSO) λ_{max} 235 (1.23×10^4), 506 (1.70×10^4) nm ($M^{-1}\,cm^{-1}$). ^{1}H NMR (500 MHz, CD_3OD) δ: 3.11 (2H, dd, $J = 6.2, 5.1$ Hz, CH_2), 4.24 (2H, dd, $J = 6.2$, 5.1 Hz, CH_2), 6.53 (1H, d, $J = 2.2$ Hz), 6.55 (3H, d, $J = 0.9$ Hz), 6.87 (2H, dt, $J = 9.7$, 1.2 Hz), 7.44–7.38 (1H, m), 7.75 (1H, td, $J = 7.7$, 1.3 Hz), 7.83 (1H, td, $J = 7.5$, 1.4 Hz), 8.28–8.22 (1H, m). ^{13}C NMR (126 MHz, CD_3OD) δ: 30.83, 63.48, 104.68, 113.60, 124.17, 130.94, 131.49, 131.91, 132.14, 134.16, 159.86, 181.44. m/z (Orbitrap) 435.1007 [M^+].

8.2.21 2-Thioethyl Fluorescein (64)

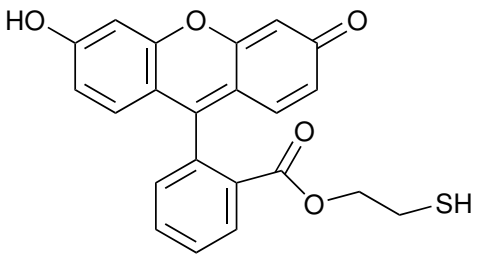

Compound **63** (24 mg, 0.04 mmol) was dissolved in CH_2Cl_2 (2 mL). Sodium metabisulfite (9 mg, 0.05 mmol) was dissolved in distilled water (1 mL). The solutions were combined and refluxed (110 °C) under nitrogen with vigorous stirring for 16 h. Reaction completion was indicated by T.L.C. (CH_2Cl_2–MeOH 9:1), with complete disappearance of the starting material ($R_f = 0.0$) and formation of new peaks at $R_f = 0.6$ and 0.68. After removing from heat, the solution phases were separated. The aqueous layer was washed with CH_2Cl_2 (2 ×5 mL) and dried over $MgSO_4$. The solvent was removed via rotary evaporation, and the product purified *via* column chromatography silica gel using CH_2Cl_2–MeOH (9 : 1) as the elutent mixture. The desired product gave an orange band ($R_f = 0.68$). The solvent was removed via rotary evaporation, the resulting product was collected as a red powder (32 mg, 76 %). M.p. 178–179 °C. Found C 64.18, H 3.59 %; $C_{22}H_{16}O_5S \cdot H_2O$ requires C 64.38 , H 4.42 %. UV/Vis (DMSO) λ_{max} 232 (3.33×10^4), 459 (2.10×10^4), 488 (1.90×10^4) nm ($M^{-1}\,cm^{-1}$). ^{1}H NMR (500 MHz, MeOD) δ 2.43 (2H, t, $J = 6.4$ Hz, CH_2), 4.09 (2H, t, $J = 6.4$ Hz, CH_2), 6.71 (2H, dd, $J = 9.2,\ 2.2$ Hz), 6.77–6.75 (2H, m), 7.04 (2H, d, $J = 9.3$ Hz), 7.45 (1H, dd, $J = 7.5,\ 1.3$ Hz), 7.80 (1H, td, $J = 7.7,\ 1.4$ Hz), 7.87 (1H, td, $J = 7.5,\ 1.4$ Hz), 8.33 (1H, dd, $J = 7.9,\ 1.3$ Hz). [CARBON]. m/z (Orbitrap) 392.07 [M^+].

8.3 X-Ray Crystallography

For each sample, crystals were suspended in oil and one was mounted on a glass fibre and fixed in the cold nitrogen stream of the diffractometer. Data were collected using Mo-K_α ($\lambda = 0.710\,73$ Å) radiation using either and Oxford Diffraction

Xcalibur-3 CCD diffractometer equipped with a graphite monochromator ($\mathbf{Y1_{Ru}}$ · MeCN, $\mathbf{Y5_{Ru}}$ · MeCN, $\mathbf{D2_{Fe}}$ · 2 MeOH · 1.5 H_2O) or a Rigaku FR-E++ equipped with molybdenum rotating anode equipped with confocal mirrors ($\mathbf{Y2_{Ru}}$ · MeCN, $\mathbf{Y4_{Ru}}$, $\mathbf{Y2_{Fe}}$ · MeCN, $\mathbf{D2_{Ru}}$ · 3 MeOH · 1.5 H_2O). Data were processed using CrysAlisPro[178] ($\mathbf{Y1_{Ru}}$ · MeCN, $\mathbf{Y5_{Ru}}$ · MeCN, $\mathbf{D2_{Fe}}$ · 2 MeOH · 1.5 H_2O)[178] or CrystalClear-SM Expert ($\mathbf{Y2_{Ru}}$ · MeCN, $\mathbf{Y4_{Ru}}$, $\mathbf{Y2_{Fe}}$ · MeCN, $\mathbf{D2_{Ru}}$ · 3 MeOH · 1.5 H_2O).[179] Structures were determined dual space methods in SHELXT-2014[180] and refined by full-matrix least-squares methods on F^2 in SHELXL-2014.[181] Non-hydrogen atoms were refined with anisotropic thermal parameters. Hydrogen atoms bound to carbon were included in idealized positions and their U_{iso} values were set to ride on the U_{eq} values of the parent atom. In $\mathbf{Y1_{Ru}}$ · MeCN, $\mathbf{Y4_{Ru}}$, $\mathbf{Y5_{Ru}}$ · MeCN and $\mathbf{Y2_{Fe}}$ · MeCN hydrogen atoms bound to nitrogen were located in the Fourier difference map and were refined with the caramoyl N−H distance restrained to 0.84(2) Å and, where present, the amine N−H distances restrained to 0.88(2) Å. In $\mathbf{Y2_{Fe}}$ · MeCN one C−O distance was restrained to 1.150(2) Å. In $\mathbf{Y2_{Ru}}$ · MeCN, $\mathbf{D2_{Fe}}$ · 2 MeOH · 1.5 H_2O and $\mathbf{D2_{Ru}}$ · 3 MeOH · 1.5 H_2O the hydrogen atoms bound to nitrogen and oxygen could not be located reliably in this way and were therefore included using a riding model. Complex $\mathbf{Y4_{Ru}}$ was refined as a two component twin with final occupancy of the major part of 0.952(7).

Data for $\mathbf{D2_{Fe}}$ · 2 MeOH · 1.5 H_2O were refined as a two-component inversion twin. For the two water atoms no hydrogen atoms were included in the model. A disordered solvent region in $\mathbf{D2_{Fe}}$ · 2 MeOH · 1.5 H_2O containing approximately one molecule of MeOH could not be modelled successfully and was handled using SQUEEZE.[182]

One methanol molecule in $\mathbf{D2_{Ru}}$ · 3 MeOH · 1.5 H_2O was disordered over two positions with the carbon atom in a common position. The thermal parameters of the two oxygen atoms were constrained to the same value, whilst the carbon atom was constrained to the same position and thermal parameters in both molecules. At the end of the refinement the occupancy of the major position was 0.522(17).

Data collection parameters are summarised in Tables 6 and 7.

Table 6: Summary of crystallographic data for $\mathbf{Y1_{Ru}}$ · MeCN, $\mathbf{Y2_{Ru}}$ · MeCN, $\mathbf{Y4_{Ru}}$ and $\mathbf{Y5_{Ru}}$ · MeCN

	$\mathbf{Y1_{Ru}}$ · MeCN	$\mathbf{Y2_{Ru}}$ · MeCN	$\mathbf{Y4_{Ru}}$	$\mathbf{Y5_{Ru}}$ · MeCN
Formula	$C_{10}H_8BrN_3O_3Ru$, C_2H_3N	$C_{14}H_{10}BrN_3O_3Ru$, C_2H_3N	$C_{10}H_9BrN_4O_3Ru$	$C_{14}H_{11}BrN_4O_3Ru$, C_2H_3N
Formula weight	440.23	490.28	414.19	505.30
Crystal system	Triclinic	Triclinic	Monoclinic	Triclinic
Space group	$P\bar{1}$	$P\bar{1}$	Cc	$P\bar{1}$
a/Å	7.0770(3)	8.1629(6)	8.7710(5)	7.8077(11)
b/Å	9.9476(3)	8.9306(6)	12.6008(9)	9.6098(10)
c/Å	12.2898(4)	12.2320(9)	12.7779(9)	12.7601(10)
α/°	108.791(3)	84.749(14)	90	91.963(8)
β/°	100.660(3)	89.791(15)	105.423(2)	98.272(9)
γ/°	101.096(3)	87.448(14)	90	97.406(10)
V/Å^3	774.84(5)	887.08(11)	1361.38(16)	938.17(18)
Z	2	2	4	2
T/K	140(2)	100(2)	100(2)	140(2)
Crystal size/mm	0.15 × 0.08 × 0.06	0.07 × 0.02 × 0.01	0.10 × 0.09 × 0.02	0.10 × 0.08 × 0.01
2θ/°	27.5	27.5	27.5	25.0
Reflections measured	12 751	12 774	8012	12 723
Unique reflections, R_{int}	3552, 0.037	4060, 0.143	2779, 0.031	3310, 0.107
Reflections with $I > 2\sigma(I)$	3248	2413	2763	2308
No. parameters	204	232	186	237
R_1 $[I > 2\sigma(I)]$	0.028	0.087	0.0219	0.060
wR_2 (all data)	0.054	0.234	0.049	0.147

Table 7: Summary of crystallographic data for $\mathbf{Y2_{Fe}}$ · MeCN, $\mathbf{D2_{Fe}}$ · 2 MeOH · 1.5 H_2O and $\mathbf{D2_{Ru}}$ · 3 MeOH · 1.5 H_2O

	$\mathbf{Y2_{Fe}}$ · MeCN	$\mathbf{D2_{Fe}}$ · 2 MeOH · 1.5 H_2O	$\mathbf{D2_{Ru}}$ · 3 MeOH · 1.5 H_2O
Formula	$C_{14}H_{10}BrFeN_3O_3$, C_2H_3N	$C_{36}H_{36}Fe_2N_4O_{16}S_2$, 2 CH_4O, 1.5 H_2O	$C_{36}H_{36}N_4O_{16}Ru_2S_2$, 3 CH_4O, 1.5 H_2O
Formula weight	445.0	1047.61	1170.1
Crystal system	Triclinic	Monoclinic	Monoclinic
Space group	$P\bar{1}$	$C2$	$C2$
a/Å	8.0450(6)	23.8608(7)	24.1018(17)
b/Å	8.9535(5)	13.3771(5)	13.3121(9)
c/Å	12.1950(9)	15.4092(5)	15.5776(11)
α/°	96.322(6)	90	90
β/°	91.386(6)	101.705(3)	103.281(2)
γ/°	92.148(6)	90	90
V/Å^3	872.11(10)	4816.2(3)	4864.3(6)
Z	2	4	4
T/K	100(2)	140(2)	100(2)
Crystal size/mm	0.09 × 0.06 × 0.01	0.38 × 0.35 × 0.28	0.20 × 0.06 × 0.04
2θ/°	27.5	28.7	37.5
Reflections measured	15 488	35 931	34 718
Unique reflections, R_{int}	3981, 0.049	10 843, 0.063	10 840, 0.046
Reflections with $I > 2\sigma(I)$	3596	8067	10 547
No. parameters	232	604	623
R_1 $[I > 2\sigma(I)]$	0.051	0.051	0.038
wR_2 (all data)	0.143	0.112	0.109

8.4 Myoglobin Assay

Stock solutions of horse heart myoglobin (approx. 130 mg in 4 mL) and sodium thionite (roughly 200 fold excess) were prepared in phosphate buffered saline (PBS, 0.01 M, pH = 7.4). For the reference spectrum of deoxy-myoglobin, a disposable cuvette was filled with myoglobin solution (500 µL), sodium thionite (100 µL) and PBS (400 µL). For the reference spectrum of carboxy-myoglobin, gaseous CO was passed through to saturate the solution before a UV/Vis spectrum was obtained. For the putative CORMS, the metal complex was dissolved in DMSO to a known concentration before transfer a cuvette (10 µL). To this cuvette were added stock solutions of myoglobin (500 µL), and sodium thionite (100 µL), along with PBS (390 µL). A UV/Vis spectrum was run, followed by irradiation of visible light. The cuvette was removed from the light source before running the UV/Vis spectrum. This procedure was repeated as appropriate.

8.5 Quantum Yield Measurements

All quantum yields were carried out using a liquid phase potassium ferrioxalate actinometer. The actinometer was prepared in complete darkness by mixing $FeCl_3$ (24.4 g, 150 mmol) in water (100 mL) with $K_2C_2O_4$ (76.0 g, 457 mmol) in water (300 mL) together and allowing to stir for 1.5 h, after which a green precipitate forms. The supernatant was removed and the precipitate recrystallised from hot water three times. The actinometer stock solution was prepared by dissolving the $K_3[Fe(C_2O_4)_3]$ precipitate (8.94 g, 18.2 mmol) in distilled water (800 mL) followed by addition of sulfuric acid (1.0 M, 100 mL) and making up to 1 L with distilled water. The irradiation was done in a darkroom using a red photographic safelight. The light intensity in a photochemical reaction is determined by irradiating the ferrioxalate solution and monitoring the subsequent changed in absorbance at 510 nm. For each actinometeric measurement a cuvette was charged with 1 mL (V_1) of ferrioxalate solution. The cuvette was placed at a specified distance away from the light source and irradiated for a set period of time.

After the allocated irradiation time (t), the solution was well mixed and an aliquot volume (0.5 mL, V_2) was added to a volumetric flask (10 mL, V_3) A buffer solution (half of V_2, 0.25 mL) and phenanthroline solution (0.3 % by weight, 2 mL) was added. The solution was made up to the mark with distilled water (7.25 mL). The solution was mixed and allowed to develop for 1 h. The absorbance was measured at 510 nm using distilled water as a reference.

8.6 Anti-Inflammatory Assays

8.6.1 TNF Assay

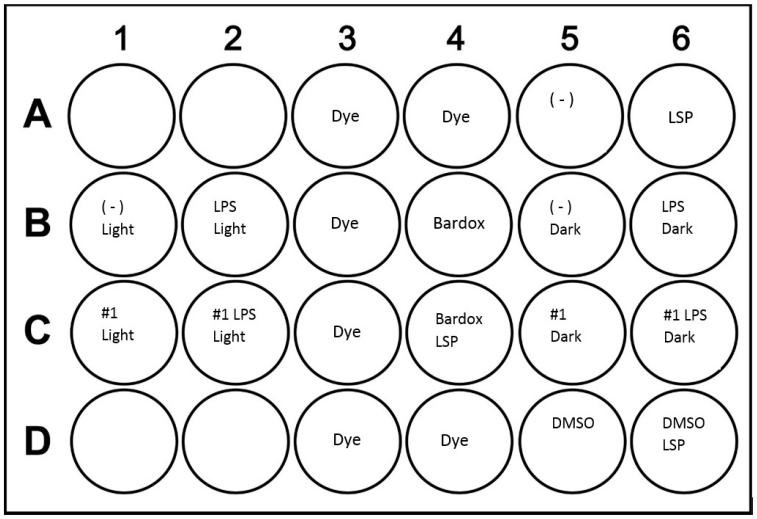

The human monocytic cell line, THP-1, was obtained from the European Collection of Cell Cultures (Health Protected Agency, Salisbury, UK). The THP-1 cells were cultured in RPMI 1640 medium, supplemented with 10 % foetal bovine serum, L-glutamine (2 mM), penicillin (100 U/mL) and streptomycin (100 µg mL^{-1}). Cells cultures were maintained *via* incubation at 37 °C in a humidified atmosphere with 5 % CO_2. Cells used were between passages 5 and 20.

THP-1 cells (0.5×10^6 cells/well, 0.5 mL) were seeded in a 24-well plate as shown above. Water containing organic food dye (1 mL) was added to wells (A3, A4, B3, C3, D3, D4) to capture any scattered light from penetrating the dark conditioned

wells. DMSO (1.0 µL) was added to vehicle control wells D5 and D6. Bardoxolone methyl (50 µM final concentration) was added to positive anti-inflammatory control wells B4 and C4. CORM was dissolved in DMSO to give a 50 mM stock solution. Administration of CORM (1.0 µL) resulted in a final CORM concentration of 50 µM in the cellular solution. After CORM administration to wells C1 and C5, the 24-well plate was incubated at 37 °C for 10 min. CORM addition to wells C2 and C6 was followed by further incubation (37 °C) for 20 min. A total of 30 min was allowed for CORM cellular uptake before stimulation with LPS (1.0 µg mL^{-1} final concentration). 30 min after CORM addition to well C1, LPS was added to well C4 followed by 'high power' visible light irradiation of well C1 for 10 min (distance between well and light source = 5 cm). Administration of LPS to wells C2, A6, B6, C6 and D6 was followed by successive irradiations (10 min) of wells C2 (30 min after CORM addition) and B1. LPS was added to well B2 prior to irradiation (10 min). The 24-well plate was incubated for 3 h. The samples were centrifuged (2000 rpm, 5 min) and sample supernatants were collected. Cytokine concentration quantified *via* ELISA kit. Each TNF assay was completed three times.

8.6.2 TNF ELISA

'Coating buffer' consisting of $NaHCO_3$ (0.72 g, 8.6 mmol) and Na_2CO_3 (0.16 g, 1.5 mmol) dissolved in millipore water (100 mL) was made to pH 9.5 with small additions of NaOH (5 M). A 1/250 dilution of capture antibody was made up with the coating buffer, of which 100 µL was added to each well of a 96-well Nunc-Immuno polystyrene Maxisorp ELISA flat bottom plate. The plate was sealed and incubated overnight at 4 °C. Phosphate-buffered saline (PBS) wash was made up by dissolving NaCl (8.0 g, 146 mmol), Na_2HPO_4 (0.11 g, 0.80 mmol), KCl (0.20 g, 2.68 mmol) and KH_2PO_4 (0.2 g, 1.47 mmol) in millipore water (1 L) and made up to pH 7.0 using NaOH (5 M). The coating buffer was removed from the wells using a multi-channel pipette and the plate was washed three times using the PBS wash with Tween-20 (450 µL) added. After each wash, the plate was inverted and blotted onto absorbent paper to remove residual buffer. Into each well was added assay dilutant (200 µL), which consisted of a PBS

and foetal bovine serum (FBS) (9 : 1). The plate was sealed and left at RT for 1 h. The TNF assay samples were prepared, with the samples containing LPS diluted 1/3. Standards are also prepared *via* serial dilutions: concentrations of human TNF at 500, 250, 125, 62.5, 31.2, 15.6 and 7.8 $\mathrm{pg\,mL^{-1}}$. Assay diluent served as the zero standard. The assay diluent was removed from each well, and the plate was washed three times using the PBS-Tween-20 wash. After each wash, the plate was inverted and blotted onto absorbent paper to remove residual buffer. A standard or TNF assay sample (100 µL) was pipetted into selected wells. The plate was sealed and left at RT for 2 h. The standard/TNF assay samples were removed *via* pipette, and the plate was washed five times using the PBS-Tween-20 wash. After each wash, the plate was inverted and blotted onto absorbent paper to remove residual buffer. Working detector (100 µL) solution (1/250 dilution of detection antibody + 1/250 dilution of SAv-HRP reagent) was added to each well. The plate was sealed and incubated at RT for 1 h. The plate was aspirated and washed using the PBS-Tween-20 mixture seven times, with each wash allowing the wells to soak for 45 s. After each wash, the plate was inverted and blotted onto absorbent paper to remove residual buffer. The substrate solution was made up by mixing reagent A and reagent B (1:1) into a light-protected vial. Protected from light, the substrate solution (100 µL) was added to each well. The plate was sealed, covered in tin foil and left at RT for 30 min. Addition of a stop solution (H_2SO_4, 1 M, 50 µL) to each well caused a colour change from blue to yellow (colouration dependent on concentration of human TNF). Absorbance measurement at 450 nm were recorded, with subtraction of the absorbance at 570 nm which acted as a wavelength correction.

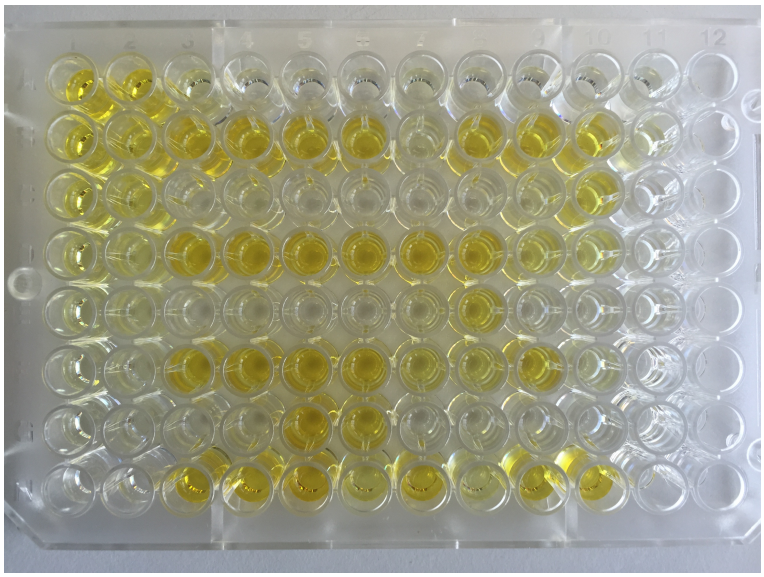

8.7 Density Functional Theory Calculations

All calculations were performed using the Gaussian 09[183] computational package. Geometry optimisation and frequency calculations have been carried out using the Tao–Perdew–Staroverov–Scuseria[184] functional. Bromine, iron and sulfur atoms were described by the Hay and Wadt LANL2DZ[185,186] basis set with effective core potential. All other atoms employ the all-electron 6-31++G** basis set. Structures were geometry optimised in the gas phase with the default convergence criteria and confirmed as minima through frequency calculations.

References

(1) C. C. Romão, W. A. Blättler, J. D.Seixas and G. J. Bernardes, *Chem. Soc. Rev.*, 2012, **41**, 3571–3583.

(2) T. Sjöstrand, *Nature*, 1949, **164**, 729–730.

(3) R. Tenhunen, H. S. Marver and R. Schmid, *Proc. Natl. Acad. Sci. USA*, 1968, **61**, 748–755.

(4) B. E. Mann, *Organometallics*, 2012, **31**, 5728–5735.

(5) L. E. Otterbein, F. H. Bach, J. Alam, M. P. Soares, H. T. Lu, M. Wysk, R. J. Davis, R. A. Flavell and A. M. Choi, *Nat. Med.*, 2000, **6**, 422–428.

(6) R. Motterlini, B. Hass and R. Foresti, *Med. Gas. Res.*, 2012, **2**, 28.

(7) R. Motterlini, J. E. Clark, R. Foresti, P. Sarathchandra, B. E. Mann and C. J. Green, *Circ. Res.*, 2002, **90**, e17–e24.

(8) R. Foresti, J. Hammad, J. E. Clark, T. R. Johnson, B. E. Mann, A. Friebe, C. J. Green and R. Motterlini, *Br. J. Pharmacol*, 2004, **142**, 453–460.

(9) R. Song, Z. Zhou, P. K. M. Kim, R. A. Shapiro, F. Liu, C. Ferran, A. M. Choi and L. E. Otterbein, *J. Biol. Chem.*, 2004, **279**, 44327–44334.

(10) L. Wu and R. Wang, *Pharmacol. Rev.*, 2005, **57**, 585–630.

(11) R. Tenhunen, H. S. Marver and R. Schmid, *J. Biol. Chem.*, 1969, **244**, 6388–6394.

(12) W. Durante, *Curr Drug Targets*, 2010, **11**, 1504–1516.

(13) S. Kumar and U. Bandyopadhyay, *Toxicol. Lett.*, 2005, **157**, 175–188.

(14) T. Jansen and A. Daiber, *Front. Pharmacol.*, 2012, **3**, 30.

(15) H.-O. Pae and H.-T. Chung, *Immune Netw*, 2009, **9**, 12–19.

(16) A. Nakao, A. M. Choi and N. Murase, *J. Cell. Mol. Med.*, 2006, **10**, 650–671.

(17) R. Motterlini, B. E. Mann, T. R. Johnson, J. E. Clark, R. Foresti and C. J. Green, *Curr. Pharm. Des.*, 2003, **9**, 2525–2539.

(18) K. D. Poss and S. Tonegawa, *Proc. Natl. Acad. Sci. USA*, 1997, **94**, 10925–10930.

(19) S. W. Chung, S. Hall and M. A. Perrella, *Cell Microbiol.*, 2009, **11**, 199–207.

(20) S. W. Ryter, J. Alam and A. M. Choi, *Physiol. Rev.*, 2006, **86**, 583–650.

(21) S. Brouard, L. E. Otterbein, J. Anrather, E. Tobiasch, F. H. Bach, A. M. Choi and M. P. Soares, *J. Exp. Med.,* 2000, **192**, 1015–1026.

(22) P. Wiesel, A. P. Patel, N. DiFonzo, P. B. Marria, C. U. Sim, A. Pellacani, K. Maemura, B. W. LeBlanc, K. Marino, C. M. Doerschuk, S.-F. Yet, M.-E. Lee and M. A. Perrella, *Circulation*, 2000, **102**, 3015–3022.

(23) C. Chauveau, D. Bouchet, J.-C. Roussel, P. Mathieu, C. Braudeau, K. Renaudin, L. Tesson, J.-P. Soulillou, S. Lyer, R. Buelow and I. Anegon, *Am. J. Transplant.*, 2002, **2**, 581–592.

(24) B. E. Mann and R. Motterlini, *Chem. Commun.*, 2007, 4197–4208.

(25) P. K. Chatterjee, *Br. J. Pharmacol*, 2004, **142**, 391–393.

(26) T. R. Johnson, B. E. Mann, J. E. Clark, R. Foresti, C. J. Green and R. Motterlini, *Angew. Chem. Int. Ed*, 2003, **43**, 3722–3729.

(27) T.-Y. Tsui, A. Obed, Y.-T. Siu, S.-F. Yet, L. Prantl, H. J. Schlitt and S.-T. Fan, *Shock*, 2007, **27**, 165–171.

(28) L. E. Otterbein, S. L. Otterbein, E. Ifedigbo, F. Liu, D. E. Morse, C. Fearns, R. J. Ulevitch, R. Knickelbein, R. A. Flavell and A. M. Choi, *Am. J. Pathol.*, 2003, **163**, 2555–2563.

(29) H. P. Kim, S. W. Ryter and A. M. Choi, *Annu. Rev. Pharmacol. Toxicol.*, 2006, **46**, 411–449.

(30) D. Morse, S. E. Pischke, Z. Zhou, R. J. Davis, R. A. Flavell, T. Loop, S. L. Otterbein, L. E. Otterbein and A. M. Choi, *J. Biol. Chem.*, 2003, **278**, 36993–36998.

(31) J. Boczkowski, J. J. Poderoso and R. Motterlini, *Trends Biochem. Sci.*, 2006, **31**, 614–621.

(32) S. Mishra, T. Fujita, V. N. Lama, D. Nam, H. Liao, M. Okada, K. Minamoto, Y. Yoshikawa, H. Harada and D. J. Pinsky, *Proc. Natl. Acad. Sci. USA*, 2006, **103**, 5191–5196.

(33) S. Ghatta, D. Nimmagadda, X. Xu and S. T. O'Rourke, *Pharmacol. Ther.*, 2006, **110**, 103–116.

(34) Q. Xi, S. Cheranov and J. H. Jaggar, *Circ. Res.*, 2005, **97**, 354–362.

(35) P. Sawle, J. Hammad, I. J. Fairlamb, B. Mouton, C. O'Brien, J. Lynam, A. Duhme-Klair, R. Foresti and R. Motterlini, *J. Pharmacol. Exp. Ther.*, 2006, **318**, 403–410.

(36) L. J. Sampson, F. Plane and C. J. Garland, *Naunyn Schmiedebergs Arch. Pharmacol.*, 2001, **364**, 220–225.

(37) K. Mikawa, H. Kume and K. Takagi, *Clin. Exp. Pharmacol. Physiol.*, 1997, **24**, 175–181.

(38) R. Wang and L. Wu, *J. Biol. Chem.*, 1997, **272**, 8222–8226.

(39) J. H. Jaggar, H. P. Anlong Li, J. Liu, E. S. Umstot, A. M. Dopico and C. W. Leffler, *Circ. Res.*, 2005, **97**, 805–812.

(40) S. E. Williams, P. Wootton, H. S. Mason, J. Bould, D. E. Iles, D. Riccardi, C. Peers and P. J. Kemp, *Science*, 2004, **306**, 2093–2097.

(41) B. Brüne and V. Ullrich, *Mol. Pharmacol.*, 1988, **32**, 497–504.

(42) M. Desmard, R. Foresti, D. Morin, M. Dagouassat, A. Berdeaux, E. Denamur, S. H. Crook, B. E. Mann, D. Scapens, P. Montravers, J. Boczkowski and R. Motterlini, *Antioxid. Redox Signal.*, 2012, **16**, 153–163.

(43) K. Sato, J. Balla, L. Otterbein, R. N. Smith, S. Brouard, Y. Lin, E. Csizmadia, J. Sevigny, S. C. Robson, G. Vercellotti, A. M. Choi, F. H. Bach and M. P. Soares, *J. Immunol.*, 2001, **166**, 4185–4194.

(44) R. A. F. Hegazi, K. N. Rao, A. Mayle, A. R. Sepulveda, L. E. Otterbein and S. E. Plevy, *J. Exp. Med.*, 2005, **202**, 1703–1713.

(45) S. W. Chung, X. Liu, A. A. Macias, R. M. Baron and M. A. Perrella, *J. Clin. Invest.*, 2008, **118**, 239–247.

(46) F. Gullotta, A. di Masi and P. Ascenzi, *IUBMB Life*, 2012, **64**, 378–386.

(47) R. Foresti, M. G. Bani-Hani and R. Motterlini, *Intensive Care Med.*, 2008, **34**, 649–658.

(48) A. C. Pena, N. Penacho, L. Mancio-Silva, R. Neres, J. D. Seixas, A. C. Fernandes, C. C. Romão, M. M. Mota, G. J. Bernardes and A. Pamplona, *Antimicrob. Agents Chemother.*, 2011, **56**, 1281–1290.

(49) B. S. Zuckerbraun, L. E. Otterbein, P. Boyle, R. Jaffe, J. Upperman, R. Zamora and H. R. Ford, *Am. J. Physiol. Gastrointest. Liver Physiol.*, 2005, **289**, G607–G613.

(50) H. Christou, T. Morita, C.-M. Hsieh, H. Koike, B. Arkonac, M. A. Perrella and S. Kourembanas, *Circ. Res.*, 2000, **86**, 1224–1229.

(51) S.-F. Yet, M. A. Perrella, M. D. Layne, C.-M. Hsieh, K. Maemura, L. Kobzik, P. Wiesel, H. Christou, S. Kourembanas and M.-E. Lee, *J. Clin. Invest.*, 1999, **103**, R23–R29.

(52) M. Hangaishi, N. Ishizaka, T. Aizawa, Y. Kurihara, J.-I. Taguchi, R. Nagai, S. Kimura and M. Ohno, *Biochem. Biophys. Res. Commun.*, 2000, **279**, 582–588.

(53) S.-F. Yet, R. Tian, M. D. Layne, Z. Y. Wang, K. Maemura, M. Solovyeva, B. Ith, L. G. Melo, L. Zhang, J. S. Ingwall, V. J. Dzau, M.-E. Lee and M. A. Perrella, *Circ. Res.*, 2001, **89**, 168–173.

(54) L. E. Otterbein, B. S. Zuckerbraun, M. Haga, F. Liu, R. Song, A. Usheva, C. Stachulak, N. Bodyak, R. N. Smith, E. Csizmadia, S. Tyagi, Y. Akamatsu, R. J. Flavell, T. R. Billiar, E. Tzeng, F. H. Bach, A. M. K. Choi and M. P. Soares, *Nat. Med.*, 2003, **9**, 183–190.

(55) H. Fujimoto, M. Ohno, S. Ayabe, H. Kobayashi, N. Ishizaka, H. Kimura, K. Yoshida and R. Nagai, *Arterioscler. Thromb. Vasc. Biol.*, 2004, **24**, 1848–1853.

(56) E. Dubuis, M. Potier, R. Wang and C. Vandier, *Cardiovasc. Res.*, 2005, **65**, 751–761.

(57) T. Kaizu, A. Ikeda, A. Nakao, A. Tsung, H. Toyokawa, S. Ueki, D. A. Geller and N. Murase, *Am. J. Physiol. Gastrointest. Liver Physiol.*, 2008, **294**, G236–G244.

(58) J. Clark, P. Naughton, S. Shurey, C. Green, T. Johnson, B. Mann, R. Foresti and R. Motterlini, *Circ. Res.*, 2003, **93**, e2–e8.

(59) D. E. Bikiel, E. González Solveyra, F. Di Salvo, H. M. S. Milagre, M. N. Eberlin, R. S. Corrêa, J. Ellena, D. A. Estrin and F. Doctorovich, *Inorg. Chem.*, 2011, **50**, 2334–2345.

(60) U. Hasegawa, A. J. van der Viles, E. Simeoni, C. Wandrey and J. A. Hubbell, *J. Am. Chem. Soc.*, 2010, **132**, 18273–18280.

(61) S. Garcia-Gallego and G. J. L. Bernardes, *Angew. Chem. Int. Ed.*, 2014, **53**, 9712–9721.

(62) T. Santos-Silva, A. Mukhopadhyay, J. D. Seixas, G. J. L. Bernardes, C. C. Romão and M. J. Romão, *J. Am. Chem. Soc.*, 2011, **133**, 1192–1195.

(63) D. Achatz, M. A. Lang, A. Völkl, W. P. Fehlhammer and W. Beck, *Z. Anorg. Allg. Chem.*, 2005, **631**, 2339–2346.

(64) A. R. Marques, L. Kromer, D. J. Gallo, N. Penacho, S. S. Rodrigues, J. D. Seixas, G. J. L. Bernardes, P. M. Reis, S. L. Otterbein, R. A. Ruggieri, A. S. G. Gonçalve, A. M. L. Gonçalves, M. N. D. Matos, I. Bento, L. E. Otterbein, W. A. Blättler and C. C. Romão, *Organometallics*, 2012, **31**, 5810–5822.

(65) S. Romanski, B. Kraus, U. Schatzschneider, J.-M. Neudorfl, S. Amslinger and H.-G. Schmalz, *Angew. Chem. Int. Ed.*, 2011, **50**, 2392–2396.

(66) S. Botov, E. Stamellou, S. Romanski, M. Guttentag, R. Alberto, J.-M. Neudorfl, B. Yard and H.-G. Schmalz, *Organometallics*, 2013, **32**, 3587–3594.

(67) S. Romanski, E. Stamellou, J. Jaraba, D. Storz, B. Krämer, M. Hafner, S. Amslinger, H. Schmalz and B. Yard, *Free Radic. Biol. Med.*, 2013, **65**, 78–88.

(68) E. Stamellou, D. Storz, S. Botov, E. Ntasis, J. Wedel, S. Sollazzo, B. Krämer, W. van Son, M. Seelen, H. Schmalz and B. Yard, *Redox Biol.*, 2014, **2**, 739–748.

(69) L. Long, X. Jiang, X. Wang, Z. Xiao and X. Liu, *Dalton Trans.*, 2013, **42**, 15663–15669.

(70) R. Weissleder, *Nat. Biotechnol.*, 2001, **19**, 316–317.

(71) C.-L. Tsai, J.-C. Chen and W.-J. Wang, *J Med Biol Eng*, 2001, **21**, 7–14.

(72) M. A. Wright and J. A. Wright, *Dalton Trans.*, 2016, **45**, 6801–6811.

(73) J. Niesel, A. Pinto, H. W. Peindy N'Dongo, K. Merz, I. Ott, R. Gust and U. Schatzschneider, *Chem. Commun.*, 2008, 1798–1800.

(74) P. Rudolf, F. Kanal, J. Knorr, C. Nagel, J. Niesel, T. Brixner, U. Schatzschneider and P. Nuernberger, *J. Phys. Chem. Lett.*, 2013, **4**, 596–602.

(75) H.-M. Berends and P. Kurz, *Inorg. Chim. Acta*, 2012, **380**, 141–147.

(76) H. Pfeiffer, A. Rojas, J. Niesel and U. Schatzschneider, *Dalton Trans.*, 2009, 4292–4298.

(77) G. Dördelmann, H. Pfeiffer, A. Birkner and U. Schatzschneider, *Inorg. Chem.*, 2011, **50**, 4362–4367.

(78) R. D. Rimmer, H. Richter and P. C. Ford, *Inorg. Chem.*, 2010, **49**, 1180–1185.

(79) W.-Q. Zhang, A. J. Atkin, I. J. Fairlamb, A. C. Whitwood and J. M. Lynam, *Organometallics*, 2011, **30**, 4643–4654.

(80) P. C. Kunz, W. Huber, A. Rojas, U. Schatzschneider and B. Spingler, *Eur. J. Inorg. Chem.*, 2009, 5358–5366.

(81) N. E. Brückmann, M. Wahl, G. J. Reiß, M. Kohns, W. Wätjen and P. C. Kunz, *Eur. J. Inorg. Chem.*, 2011, 4571–4577.

(82) A. J. Atkin, J. M. Lynam, B. E. Moulton, P. Sawle, R. Motterlini, N. M. Boyle, M. T. Pryce and I. J. Fairlamb, *Dalton Trans.*, 2011, **40**, 5755–5761.

(83) C. S. Jackson, S. Schmitt, Q. P. Dou and J. J. Kodanko, *Inorg. Chem.*, 2011, **50**, 5336–5338.

(84) J. M. L. Jonathan S. Ward, J. W. B. Moir, D. E. Sanin, A. P. Mountford and I. J. S. Fairlamb, *Dalton Trans.*, 2012, **41**, 10514–10517.

(85) C. Bischof, T. Joshi, A. Dimri, L. Spiccia and U. Schatzschneider, *Inorg. Chem.*, 2013, **52**, 9297–9308.

(86) S. Yang, M. Chen, L. Zhou, G. Zhang, Z. Gao and W. Zhang, *Dalton Trans.*, 2016, **45**, 3727–3733.

(87) C. Nagel, S. McLean, R. K. Poole, H. Braunschweig, T. Kramer and U. Schatzschneider, *Dalton Trans.*, 2014, **43**, 9986–9997.

(88) J. S. Ward, J. T. W. Bray, B. J. Aucott, C. Wagner, N. E. Pridmore, A. C. Whitwood, J. W. B. Moir, J. M. Lynam and I. J. S. Fairlamb, *Eur. J. Inorg. Chem.*, 2016, 5044–5051.

(89) I. Chakraborty, S. J. Carrington and P. K. Mascharak, *Acc. Chem. Res.*, 2014, **47**, 2603–2611.

(90) I. Chakraborty, S. J. Carrington and P. K. Mascharak, *ChemMedChem*, 2014, **9**, 1266–1274.

(91) R. Kretschmer, G. Gessner, H. Görls, S. H. Heinemann and M. Westerhausen, *J. Inorg. Biochem.*, 2011, **105**, 6–9.

(92) A. E. Pierri, A. Pallaoro, G. Wu and P. C. Ford, *J. Am. Chem. Soc.*, 2012, **134**, 18197–18200.

(93) H. T. Poh, B. T. Sim, T. S. Chwee, W. K. Leong and W. Y. Fan, *Organometallics*, 2014, **33**, 959–963.

(94) P. Govender, S. Pai, U. Schatzschneider and G. S. Smith, *Inorg. Chem.*, 2013, **52**, 5470–5478.

(95) F. Zobi, O. Blacque, R. A. Jacobs, M. C. Schaub and A. Y. Bogdanova, *Dalton Trans.*, 2012, **41**, 370–378.

(96) F. Zobi, L. Quaroni, G. Santoro, T. Zlateva, O. Blacque, B. Sarafimov, M. C. Schaub and A. Y. Bogdanova, *J. Med. Chem.*, 2013, **56**, 6719–6731.

(97) V. Yempally, S. J. Kyran, R. K. Raju, W. Y. Fan, E. N. Brothers, D. J. Darensbourg and A. A. Bengali, *Inorg. Chem.*, 2014, **53**, 4081–4088.

(98) M. A. Gonzalez, S. J. Carrington, N. L. Fry, J. L. Martinez and P. K. Mascharak, *Inorg. Chem.*, 2012, **51**, 11930–11940.

(99) M. A. Gonzalez, S. J. Carrington, I. Chakraborty, M. M. Olmstead and P. K. Mascharak, *Inorg. Chem.*, 2013, **52**, 11320–11331.

(100) S. J. Carrington, I. Chakraborty and P. K. Mascharak, *Chem. Commun.*, 2013, **49**, 11254–11256.

(101) S. J. Carrington, I. Chakraborty, J. M. L. Bernard and P. K. Mascharak, *ACS Med. Chem. Lett.*, 2014, **5**, 1324–1328.

(102) E. Kottelat, A. Ruggi and F. Zobi, *Dalton Trans.*, 2016, **45**, 6920–6927.

(103) R. Motterlini, P. Sawle, J. Hammad, S. Bains, R. Alberto, R. Foresti and C. J. Green, *FASEB J.*, 2005, **19**, 284–286.

(104) P. Peng, C. Wang, Z. Shi, V. K. Johns, L. Ma, J. Oyer, A. Copik, R. Igarashi and Y. Liao, *Org. Biomol. Chem.*, 2013, **11**, 6661–6864.

(105) E. Palao, T. Slanina, L. Muchova, T. Solomek, L. Vitek and P. Klan, *J. Am. Chem. Soc.*, 2016, **138**, 126–133.

(106) T. Šolomek, J. Wirz and P. Klán, *Acc. Chem. Res.*, 2015, **48**, 3064–3072.

(107) R. A. Yokel, *Neuromolecular Med.*, 2009, **11**, 297–310.

(108) P. J. Turrell, J. A. Wright, J. N. T. Peck, V. S. Oganesyan and C. J. Pickett, *Angew. Chem. Int. Ed.*, 2010, **49**, 7508–7511.

(109) P. J. Turrell, A. D. Hill, S. K. Ibrahim, J. A. Wright and C. J. Pickett, *Dalton Trans.*, 2013, **42**, 8140–8146.

(110) S. McLean, B. E. Mann and R. K. Poole, *Anal. Biochem.*, 2012, **427**, 36–40.

(111) Y. Yang, S. K. Seidlits, M. M. Adams, V. M. Lynch, C. E. Schmidt, E. V. Anslyn and J. B. Shear, *J. Am. Chem. Soc.*, 2010, **132**, 13114–13116.

(112) A. R. Lippert, E. J. New and C. J. Chang, *J. Am. Chem. Soc.*, 2011, **133**, 10078–10080.

(113) B. W. Michel, A. R. Lippert and C. J. Chang, *J. Am. Chem. Soc.*, 2012, **134**, 15668–15671.

(114) J. Marhenke, K. Trevino and C. Works, *Coord. Chem. Rev.*, 2016, **306**, 533–543.

(115) S. Pai, M. Hafftlang, G. Atongo, C. Nagel, J. Niesel, S. Botov, H.-G. Schmalz, B. Yard and U. Schatzschneider, *Dalton Trans.*, 2014, **43**, 8664–8678.

(116) Y. Lee and J. Kim, *Anal. Chem.*, 2007, **79**, 7669–7675.

(117) A. Goel, *Wave Mechanics*, New Delhi, India :Discovery Publishing House, 2006.

(118) K. K. Rohatgi-Mukherjee, *Fundamentals of Photochemistry*, New Delhi, India : Wiley Eastern, 1978.

(119) M. Chaves-Ferreira, I. S. Albuquerque, D. Matak-Vinkovic, A. C. Coelho, S. M. Carvalho, L. M. Saraiva, C. C. Romão and G. J. L. Bernardes, *Angew. Chem. Int. Ed.*, 2014, **54**, 1172–1175.

(120) J. O'Brien, I. Wilson, T. Orton and F. Pognan, *Eur. J. Biochem.*, 2000, **267**, 5421–5426.

(121) T. Mosmann, *J. Immunol. Methods*, 1983, **65**, 55–63.

(122) X. Han, R. Gelein, N. Corson, P. Wade-Mercer, J. Jiang, P. Biswas, J. N. Finkelstein, A. Elder and G. Oberdörster, *Toxicology*, 2011, **287**, 99–104.

(123) R. Motterlini and L. E. Otterbein, *Nat. Rev. Drug Discov.*, 2010, **9**, 728–743.

(124) B. Wegiel, D. Gallo, E. Csizmadia, C. Harris, J. Belcher, G. M. Vercellotti, N. Penacho, P. Seth, V. Sukhatme, A. Ahmed, P. Pandolfi, L. Helczynski, A. Bjartell, J. L. Persson and L. E. Otterbein, *Cancer Res.*, 2013, **73**, 7009–7021.

(125) C. Parsons, D. Muilenburg, T. Bowles, S. Virudachalam and R. Bold, *Anticancer Res.*, 2010, **30**, 3279–3289.

(126) L. Vítek, H. Gbelcová, L. Muchová, K. Váňová, J. Zelenka, R. Koníčková, J. Šuk, M. Zadinova, Z. Knejzlík, S. Ahmad, T. Fujisawa, A. Ahmed and T. Ruml, *Dig. Liver Dis.*, 2014, **46**, 369–375.

(127) C.-N. Chen, F.-J. Hsieh, Y.-M. Cheng, K.-J. Chang and P.-H. Lee, *J. Surg. Oncol.*, 2006, **94**, 226–233.

(128) J. A. Lemire, J. J. Harrison and R. J. Turner, *Nature*, 2013, **11**, 371–384.

(129) J. A. Wright, P. J. Turrell and C. J. Pickett, *Organometallics*, 2010, **29**, 6146–6156.

(130) W. R. Hastings, M. R. Roussel and M. C. Baird, *J. Chem. Soc., Dalton Trans.*, 1990, **1**, 203–205.

(131) F. Calderazzo and F. L'Eplattenier, *Inorg. Chem.*, 1967, **6**, 1220–1224.

(132) I. F. Barnard and J. A. Elvidge, *J. Chem. Soc. Perkin Trans. I*, 1983, 1137–1140.

(133) R. Alberto, *Eur. J. Inorg. Chem.*, 2009, 21–31.

(134) A. C. Kautz, P. Kunz and C. Janiak, *Dalton Trans.*, 2016, **45**, 18045–18063.

(135) A. E. Pierri, P.-J. Huang, J. V. Garcia, J. G. Stanfill, M. Chui, G. Wu, N. Zheng and P. C. Ford, *Chem. Commun.*, 2015, **51**, 2072–2075.

(136) R. Motterlini, *Biochem. Soc. Trans.*, 2007, **35**, 1142–1146.

(137) Y. Zhang, J. W. Chan, A. Moretti and K. E. Uhrich, *J. Controlled Release*, 2015, **219**, 355–368.

(138) N. Floyd, B. Vijayakrishnan, J. R. Koeppe and B. G. Davis, *Angew. Chem. Int. Ed. Engl.*, 2009, **48**, 7798–7802.

(139) W. Beck, W. Petri and J. Meder, *J. Organomet. Chem.*, 1980, **191**, 73–77.

(140) J. D. Seixas, A. Mukhopadhyay, T. Santos-Silva, L. E. Otterbein, D. J. Gallo, S. S. Rodrigues, B. H. Guerreiro, A. M. L. Gonçalves, N. Penacho, A. R. Marques, A. R. Coelho, P. M. Reis, M. J. Romão and C. C. Romão, *Dalton Trans.*, 2013, **42**, 5985–5998.

(141) M. A. Gonzalez, M. A. Yim, S. Cheng, A. Moyes, A. J. Hobbs and P. K. Mascharak, *Inorg. Chem.*, 2012, **51**, 601–608.

(142) M. A. Gonzales, H. Han, A. Moyes, A. Radinos, A. J. Hobbs, N. Coombs, S. R. J. Oliver and P. K. Mascharak, *J. Mater. Chem. B*, 2014, **2**, 2107–2113.

(143) M. Tinajero-Trejo, N. Rana, C. Nagel, H. E. Jesse, T. W. Smith, L. K. Wareham, M. Hippler, U. Schatzschneider and R. K. Poole, *Antioxid. Redox Signal.*, 2016, **24**, 765–780.

(144) S. Jinesh, *Inflammopharmacol*, 2015, **23**, 71–77.

(145) F. M. Brennan, R. N. Maini and M. Feldmann, *Br. J. Rheumatol.*, 1992, **31**, 293–298.

(146) S. E. Plevy, C. J. Landers, J. Prehn, N. M. Carramanzana, R. L. Deem, D. Shealy and S. R. Targan, *J. Immunol.*, 1997, **159**, 6276–6282.

(147) V. Navikas and H. Link, *J. Neurosci. Res.*, 1996, **45**, 322–333.

(148) S. Hale and S. Lightman, *Cytokine*, 2006, **33**, 231–237.

(149) J. Keffer, L. Probert, H. Cazlaris, S. Georgopoulos, E. Kaslaris, D. Kioussis and G. Kollias, *EMBO J.*, 1991, **10**, 4025–4031.

(150) A. Abbate, B. W. V. Tassell and G. G. L. Biondi-Zoccai, *BioDrugs*, 2012, **26**, 217–233.

(151) J. J. Wu, K.-Y. T. Poon, J. C. Channual and A. Y.-J. Shen, *Arch. Dermatol.*, 2012, **148**, 1244–1250.

(152) K. C. F. Sheerhan, J. K. Pinckard, C. D. Arthur, L. P. Dehner, D. V. Goeddel and R. D. Schreiber, *J. Exp. Med.*, 1995, **181**, 607–617.

(153) L. Zheng, G. Fisher, R. E. Miller, J. peschon, D. H. Lynch and M. J. Lenardo, *Nature*, 1995, **377**, 348–351.

(154) I. Kirman, R. L. Whelan and O. H. Nielsen, *Eur. J. Gastroenterol. Hepatol.*, 2004, **16**, 639–641.

(155) J. L. di Gesso, J. S. Kerr, Q. Zhang, S. Raheem, S. K. Yalamanchili, D. O'Hagan, C. D. Kay and M. A. O'Connell, *Mol. Nutr. Food Res.*, 2015, **59**, 1143–1154.

(156) J. Hodge-Dufour, M. W. Marino, M. R. Horton, A. Jungbluth, M. D. Burdick, R. M. Strieter, P. W. Noble, C. A. Hunter and E. Pure, *Proc. Natl. Acad. Sci. USA*, 1998, **95**, 13806–13811.

(157) S. Masli and B. Turpie, *Immunology*, 2008, **127**, 62–72.

(158) P. Sawle, R. Foresti, B. E. Mann, T. R. Johnson, C. J. Green and R. Motterlini, *Br. J. Pharmacol.*, 2005, **145**, 800–810.

(159) Preliminary cell viability data determined *via* the MTS assay on $\mathbf{Y1_{Fe}}$ was carried out by Miss Sarah Morris.

(160) S. Qin, R. Du, S. Yin, X. Liu, G. Xu and W. Cao, *Inflamm. Res.*, 2015, **64**, 537–548.

(161) R. Ahmad, D. Raina, C. Meyer, S. Kharbanda and D. Kufe, *J. Biol. Chem.*, 2006, **281**, 35764–35769.

(162) C. A. Lipinski, F. Lombardo, B. W. Dominy and P. J. Fenney, *Adv. Drug Delivery Rev.*, 2001, **46**, 3–26.

(163) L. A. Finney and T. V. O'Halloran, *Science*, 2003, **300**, 931–936.

(164) S. R. Wecksler, A. Mikhailovsky, D. Korystov and P. C. Ford, *J. Am. Chem. Soc.*, 2006, **128**, 3831–3837.

(165) O. V. Przhonska, S. Webster, L. A. Padilha, H. Hu, A. D. Kachkovski, D. J. Hagan and E. W. Van Stryland, *Adv Fluorescence Reporters Chem Biol I*, 2010, 105–147.

(166) M. Pawlicki, H. A. Collins, R. G. Denning and H. L. Anderson, *Angew. Chem. Int. Ed.*, 2009, **48**, 3244–3266.

(167) J. Lahann, *Click Chemistry for Biotechnology and Materials Science*, Hoboken, N.J. : Wiley ; Chichester : John Wiley, 2009.

(168) S. Sun and P. Wu, *J. Phys. Chem. A*, 2010, **114**, 8331–8336.

(169) V. V. Rostovtsev, L. G. Green, V. V. Fokin and K. B. Sharpless, *Angew. Chem. Int. Ed*, 2002, **41**, 2596–2599.

(170) C. W. Tornøe, C. Christensen and M. Meldal, *J. Org. Chem.*, 2002, **67**, 3057–3064.

(171) V. D. Bock, H. Hiemstra and J. H. van Maarseveen, *Eur. J. Org. Chem.*, 2006, **2006**, 51–68.

(172) C. B. Aakeroy, N. Schultheiss and J. Desper, *Dalton Trans.*, 2006, 1627–1635.

(173) S. V. Kolyachkina, V. I. Tararov, C. S. Alexeev, D. M. Krivosheev, G. A. Romanov, E. V. Stepanova, E. S. Solomko, A. N. Inshakov and S. N. Mikhailov, *Collect. Czech. Chem. Commun.*, 2011, **76**, 1361–1378.

(174) S. R. Wecksler, J. Hutchinson and P. C. Ford, *Inorg. Chem.*, 2006, **45**, 1192–1200.

(175) F. Stonek, W. Dietrich, C. Schneeberger, W. Vycudilik and W. Tschugguel, *J. Biochem. Biophys. Methods*, 2004, **58**, 49–58.

(176) L. L. Horky, R. M. Pluta, R. J. Boock and E. H. Oldfield, *J. Neurosurg.*, 1998, **88**, 298–303.

(177) J. Y. Coe, P. M. Olley, G. Vella and F. Coceani, *Pediatr. Res.*, 1987, **22**, 422–428.

(178) *CrysAlisPro*, Agilent Technologies Ltd., Yarnton, United Kingdom, 2012.

(179) *CrystalClear-SM Expert*, Rigaku Corporation, Tokyo, Japan, 2012.

(180) G. M. Sheldrick, *Acta Cryst. C*, 2015, **71**, 3–8.

(181) G. M. Sheldrick, *Acta Cryst. A*, 2015, **71**, 3–8.

(182) P. van der Sluis and A. Spek, *Acta Cryst. A*, 1990, **46**, 194–201.

(183) M. J. Frisch, G. W. Trucks, H. B. Schlegel, G. E. Scuseria, M. A. Robb, J. R. Cheeseman, G. Scalmani, V. Barone, B. Mennucci, G. A. Petersson, H. Nakatsuji, M. Caricato, X. Li, H. P. Hratchian, A. F. Izmaylov, J. Bloino, G. Zheng, J. L. Sonnenberg, M. Hada, M. Ehara, K. Toyota, R. Fukuda, J. Hasegawa, M. Ishida, T. Nakajima, Y. Honda, O. Kitao, H. Nakai, T. Vreven, J. A. Montgomery, Jr., J. E. Peralta, F. Ogliaro, M. Bearpark, J. J. Heyd, E. Brothers, K. N. Kudin, V. N. Staroverov, R. Kobayashi, J. Normand, K. Raghavachari, A. Rendell, J. C. Burant, S. S. Iyengar, J. Tomasi, M. Cossi, N. Rega, J. M. Millam, M. Klene, J. E. Knox, J. B. Cross, V. Bakken, C. Adamo, J. Jaramillo, R. Gomperts, R. E. Stratmann, O. Yazyev, A. J. Austin, R. Cammi, C. Pomelli, J. W. Ochterski, R. L. Martin, K. Morokuma, V. G. Zakrzewski, G. A. Voth, P. Salvador, J. J. Dannenberg, S. Dapprich, A. D. Daniels, Ö. Farkas, J. B. Foresman, J. V. Ortiz, J. Cioslowski and D. J. Fox, *Gaussian 09 Revision C.01*, Gaussian, Inc., Wallingford, CT, 2009.

(184) J. Tao, J. P. Perdew, V. N. Staroverov and G. E. Scuseria, *Phys. Rev. Lett.*, 2003, **91**, 146401–146405.

(185) P. J. Hay and W. R. Wadt, *J. Chem. Phys.*, 1985, **82**, 270–283.

(186) P. J. Hay and W. R. Wadt, *J. Chem. Phys.*, 1985, **82**, 284–298.